1-1-2016

Synthesis and Characterization of Kesterite Cu2ZnSnS4 (CZTS) Thin Films for Solar Cell Application

Mohamed M.A. Abusnina
University of Denver

Recommended Citation

Abusnina, Mohamed M.A., "Synthesis and Characterization of Kesterite Cu2ZnSnS4 (CZTS) Thin Films for Solar Cell Application" (2016). *Electronic Theses and Dissertations*. 1153.
https://digitalcommons.du.edu/etd/1153

Synthesis and characterization of kesterite Cu_2ZnSnS_4 (CZTS) thin films for solar cell application

---

A Dissertation

Presented to

The Faculty of the Daniel Felix Ritchie School of Engineering and Computer Science

University of Denver

In Partial Fulfillment

of the Requirements for the Degree

Doctor of Philosophy

---

by

Mohamed M. A. Abusnina

June 2016

Advisor: Mohammad Matin

Author: Mohamed M. A. Abusnina
Title: Synthesis and characterization of kesterite Cu_2ZnSnS_4 (CZTS) thin films for solar cell application
Advisor: Mohammad Matin
Degree Date: June 2016

Abstract

The quaternary compound Cu_2ZnSnS_4 (CZTS) gained considerable attention in the last decade due to its potential as an active-layer semiconductor for low-cost thin-film solar cells. The material is composed of nontoxic and Earth-abundant constituents, has optical properties suitable for photovoltaic application, and can be synthesized using a wide variety of methods.

Polycrystalline CZTS was grown in this work using vacuum-based deposition to first deposit metal films (precursors) of Cu, Zn, and Sn. In a subsequent step, the precursors underwent an annealing treatment in sulfur vapor environment (sulfurization) to form CZTS. Using sputtering, a physical vapor deposition (PVD) technique, two different kinds of metal precursors were deposited: a) stacked precursors, in which a stack of metal layers are sequentially deposited on a glass substrate, and b) co-sputtered precursors, in which the three metals are deposited simultaneously.

The effect of sulfurization time and temperature was investigated to optimize the process and to study the impact of both factors on the morphological and structural properties of the synthesized compound. CZTS films based on a stacked precursor were prepared and characterized by X-ray fluorescence, energy-dispersive X-ray spectroscopy, electron probe microanalysis, X-ray diffraction, scanning electron microscopy , ultraviolet-visible-near-infrared spectrophotometry, and Auger electron spectroscopy. Films with dense morphology, good crystallinity, and optical energy bandgap close to

1.5 eV were obtained using annealing temperatures of 500 °C and 550 °C. Furthermore, the study addressed the issue with $Cu_{2-x}S$ phases segregated on the film surface and suggested a route to avoid their evolution.

The secondary-phase dependence on the chemical composition was studied, focusing on suppressing $Cu_{2-x}S$ phases. In addition, we addressed the importance of Sn/Cu ratio as a controlling factor to avoid developing these detrimental phases. An electron backscatter diffraction study confirmed the role of increased Cu content in achieving larger grains.

Studying the influence of the stack sequence in the precursor revealed that depositing Zn as the first or second layer leads to better adhesion, and depositing Cu as top layer minimizes the loss of Sn and allows better control of film composition. Solar cells based on CZTS films prepared with the sulfurization of precursors with different stacking orders were produced, and the best device showed power conversion efficiency (PCE) of 4.43%.

CZTS films based on co-sputtered precursors showed very promising results in terms of large grains, dense morphology, and smooth surface; however, they suffered from poor adhesion to the Mo layer due to compressive intrinsic stresses. Further investigation is needed to identify the stress origin and improve the contact to the back electrode. The best device based on CZTS films from co-sputtered precursors yielded a PCE of 1.72%.

Acknowledgements

Almost daily for the first year of this project, I asked myself, “Have I made the right decision?,” wondering what really motivated me to work in this research area. The first answer always coming to mind was, “You’re so fortunate to conduct your research at the National Renewable Energy Laboratory (NREL), one of the world’s leading institutions for renewable energy research.” I had come from electrical engineering to a field where people talk about film morphology, crystal structure, and many other terms new to me. So I was feeling overwhelmed, lacking relevant background and experience that I could rely on. At moments, I questioned my ability to complete this dissertation. But this journey has ultimately come to the end with the help and support of certain people to whom I am very thankful.

First and foremost, I direct my thanks to my academic advisor, Prof. Mohammad Matin, for accepting me as a Ph.D. student. I also express my gratitude to Dr. Mowafak Al-Jassim for enabling me to conduct my research at NREL. My special thanks go to Dr. Helio Moutinho, who had the greatest impact on my work through valuable explanations and wide-ranging discussions. I am also appreciative to: Jeff Alleman for his ongoing help; Don Gwinner for editing my writing; Bobby To, Maikel van Hest, Jeff Blackburn, and Phil Parilla for training me on different systems; and Clay DeHart and Jeff Carapella for processing my samples into complete devices.

Last but not least, I thank my family for believing in me and encouraging me to finish this task. I am thankful to my parents for supporting me in all the steps of my life. My deepest thanks go to my wife, who has always been at my side in good times and bad, and to my children for their understanding and sacrifice when it came to my work.

Table of Contents

List of Figures

List of Tables

Chapter One: Introduction

1.1 Overview

For the last several decades, world energy consumption has substantially increased, and it is expected to continue increasing in the near future [1], [2]. Major factors contributing to this increase are global population growth, rising standard of living, and economic progress. Unfortunately, a large portion of energy production relies on fossil fuel sources (i.e., oil, coal, and natural gas), which have limited availability [3] and may face shortages at some point in the future. In addition, burning of fossil fuels causes carbon dioxide (CO_2) to be emitted into the atmosphere, with CO_2 being the main contributor to global warming [4]. Hence, alternative clean and infinite energy sources are needed to cover the growing energy demand and minimize environmental pollution. In this context, renewable energy sources—including, but not limited to, solar, wind, geothermal, hydropower, and biogas—provide an optimal solution for the shortage of energy resources and for addressing the issue of climate change.

Of all the renewable energy sources, solar is the most abundant and promising source because it has the potential to handle the world's energy consumption. We are encouraged to develop systems that enable effective harvesting, transfer, and storage of solar energy when we consider that the solar energy reaching the Earth's surface in one hour is nearly equivalent to the world's total energy consumption in one year [5]. Photovoltaic (PV) technology, which directly converts sunlight into electricity using solar cells, is one of the major solar energy fields that has experienced a significant increase in capacity globally. At the end of 2014, the worldwide total installed PV capacity was more than 177 gigawatts (GW) [6].

At present, PV technology is still not competitive with fossil fuel generation of electricity in terms of electricity production cost. Closing the gap and achieving this goal requires that PV systems use high-efficiency, cost-effective solar panels, which could be accomplished by increasing the power conversion efficiency (PCE) and lowering the production costs of the solar cell. The first generation of solar cells, based on single-crystalline silicon (sc-Si) and multi-crystalline silicon (mc-Si), is the most developed PV cell technology and it dominants the market. The best PCEs achieved in the laboratory for sc-Si and mc-Si single-junction solar cells are 25.6% and 20.8%, respectively, whereas the records for silicon modules are 22.9% (sc-Si) and 18.5% (mc-Si) [7]. On the other hand, thin-film (second generation) solar cell technology provides a cost-effective alternative to the conventional Si cells through material savings (e.g., the cell active layer is only about 1–3 micrometers [µm] thick compared to Si's thickness of 100–200 µm); in addition, it uses simpler and less expensive manufacturing procedures. The main representatives of thin-film solar cells that have already reached a commercial stage are cadmium telluride (CdTe) and copper indium gallium diselenide ($Cu(InGa)Se_2$, or CIGS) cells. Devices based on CdTe and CIGS have achieved record efficiencies of 22.1% [8] and 21.7% [9], respectively. The boost in efficiencies is mainly due to improved material quality. Both materials have reached module efficiencies around 17% and can compete with mc-Si devices; however, other issues raise concerns, such as material availability and toxicity. Scarcity of indium and tellurium as well as the toxicity of tellurium have led to the search for new semiconductor materials that are Earth-abundant and environmentally benign for PV application.

In this regard, the quaternary compound Cu_2ZnSnS_4 (CZTS)—and its related alloys $Cu_2ZnSnSe_4$ (CZTSe) and $Cu_2ZnSn(SSe)_4$ (CZTSSe)—is emerging as a promising active-layer semiconductor for low-cost thin-film solar cell application due to its suitable optical properties, elemental availability, and nontoxicity of its constituents [10]–[12]. In the literature, CZTS refers widely to the selenide, sulfide, or sulfide-selenide form of the compound. CZTS is a *p*-type semiconductor with a direct bandgap of about 1.0 electron-volt (eV) for selenide (CZTSe) [13] and about 1.5 eV for sulfide (CZTS) [12]. It possesses an absorption coefficient of more than 10^4 cm^{-1}, and the bandgap can be further tuned between 1.0 and 1.5 eV by varying the ratio of selenium to sulfur in the CZTSSe compound.

Although CZTS is relatively a new material, there have been numerous published works reporting different approaches for fabricating CZTS, including vacuum and non-vacuum methods. The record efficiency for a CZTSSe device, whose absorbing active layer was fabricated by a solution-based method, is 12.6% [14], whereas the highest-achieved PCE of a pure sulfide CZTS device based on a CZTS absorbing layer fabricated using thermal evaporation is 8.4% [15]. Despite the noticeable progresses made toward achieving higher PCEs of CZTS-based solar cells, the performance of the best-reported device is still far from the theoretically estimated efficiency of about 30% [16].

One of the main challenges is controlling the film composition during the film growth process. Controlling the phase stability of this compound is also difficult and the problem of phase segregation is widely reported in the literature. Phases such as $Cu_{2-x}S$

and $Cu_{2-x}Sn_xS_3$ are especially detrimental for the device because of their metal behavior, which could lead to shunting of the cell. Therefore, studying the impact of the various growth parameters may provide more insight into how to avoid their existence.

Understanding the material reaction pathway is also a central key to achieving high-quality materials with large grain size, good crystallinity, and uniform composition. Several published works reported proposals for the formation pathway. However, due to the different growth approaches used, none of them is universally valid in explaining the compound reaction pathway.

1.2 Aim of the Study

The objectives of this research are to:

1. Develop a route for the deposition of metal layers (precursors) using sputtering.
2. Determine the sputtering conditions to control the precursor composition and thickness.
3. Optimize the parameters for the sulfurization process used to convert the metal precursors into CZTS films.
4. Study the material properties and investigate the impact of the growth parameter.
5. Understand the reaction pathway and the growth mechanism of CZTS.
6. Apply the developed CZTS films in PV devices and study their electrical characteristics.

1.3 Structure of the Work

The report is divided into five chapters, starting with an introduction that illustrates the larger perspective of the research area and then narrowing down to highlight the open questions still needing to be investigated.

Chapter 2 provides a theoretical background on CZTS thin-film solar cell technology, first describing the working principles of solar cells followed by an overview of thin-film solar cells and the properties of CZTS.

Chapter 3 explains the fabrication steps used in our approach to produce CZTS films, and the principles of the characterization techniques used to analyze the films are briefly described.

Chapter 4 presents the results of this work and discusses aspects of them in greater detail.

Finally, Chapter 5 summarizes the highlights of the results.

Chapter Two: Theoretical Background

2.1 Physics of Photovoltaics

2.1.1 Light absorption in semiconductors

When light penetrates a semiconductor, it will be absorbed or transmitted depending on the energy bandgap of the semiconductor. A portion of the incident light may be reflected at the material surface. If the penetrating light has a photon energy ($E_{ph} = hc/\lambda$, where h is the Planck's constant, c speed of light, and λ wavelength of light) that is equal to or greater than the semiconductor bandgap (E_g) (for Si: $E_g = 1.124$ eV), photons will be absorbed, causing the generation of positive and negative charge carriers within the semiconductor. In this process, an electron is excited to a higher energy level (moves from the valence band to the conduction band), leaving a free space (hole) in the valence band. Light absorption in semiconductors depends strongly on the wavelength, and it is described by the absorption coefficient $\alpha(\lambda)$ or the absorption length (penetration depth) $L(\lambda) = 1/\alpha(\lambda)$. Figure 2.1 shows the behavior of the absorption coefficient and the penetration depth of silicon as a function of the wavelength. The required thickness of the material to absorb the light is largely determined by the depth of light penetration into the material.

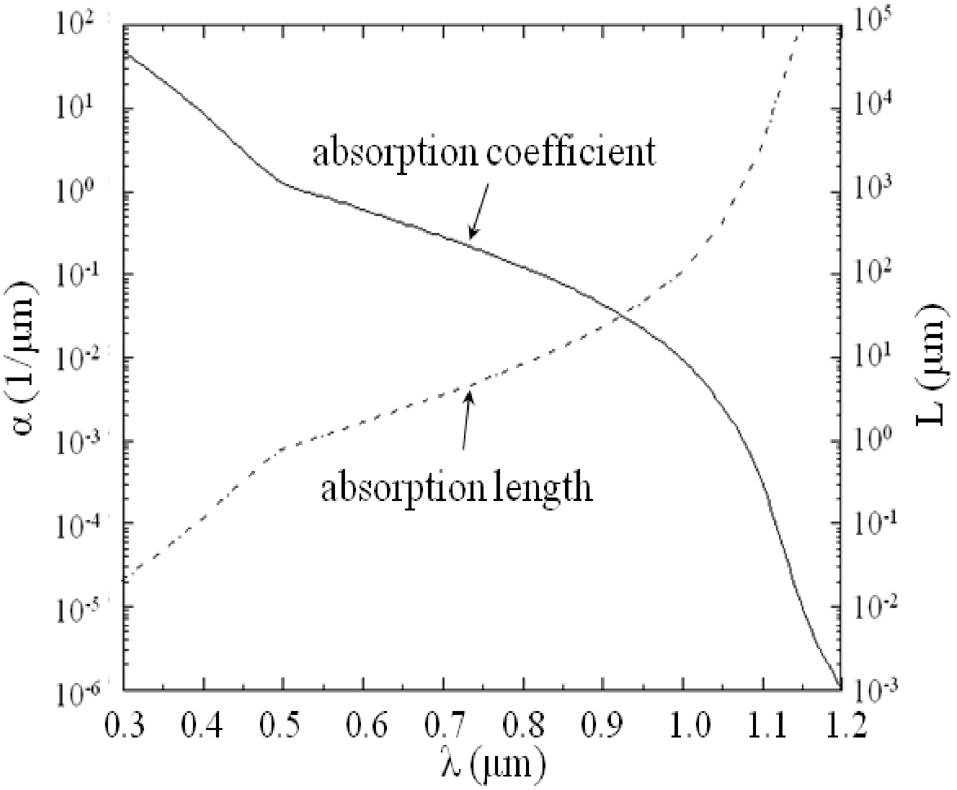

Figure 2.1: Absorption coefficient and penetration depth of silicon as a function of the light wavelength [17].

2.1.2 The p-n junction

A p-n junction is established when p-type and n-type semiconductors are joined together. We differentiate between a homojunction, where the same semiconductor material is differently doped (n- and p-type), and a heterojunction, where two different materials with different doping types are joined together.

If p- and n-type semiconductors are brought into contact, diffusion currents are formed as electrons from the n-region (near the contact interface) diffuse, due to the concentration differences of the charge carriers in both regions, to the p-region; similarly, holes diffuse in the reverse direction. Electrons in the n-region are called majority carriers and in the p-region are called minority carriers. Similarly, holes in the p-region are called majority carriers and in the n-region are called minority carriers. In the vicinity of the contact interface, positively charged donor ions (with the concentration denoted as N_D) in the n-region and negatively charged acceptors (with the concentration denoted as N_A) in the p-region remain localized, forming the so-called space-charge region (SCR) or depletion region (DR). The fixed positive and negative charges in the SCR form an electric field (E_0) from the positive donor ions in the n-region to the negative acceptor ions in the p-region. As a result of the electrical field, drift currents arise that counteract the diffusion flow of the respective charge-carrier types. At the thermodynamic equilibrium, the two currents (diffusion and drift currents) compensate each other. At equilibrium, the Fermi level must be aligned (be the same at both sides). Thus, the energy bands experience a shift equal to the built-in potential (V_0) that is established near the boundaries of the p-n junction. Figure 2.2 illustrates the band structure of intrinsic, p-type, and n-type semiconductors (a); the formation of the p-n junction (b); and the p-n junction energy band diagram (c).

From the equations for the hole and electron current densities J_p and J_n, respectively, and because in the equilibrium state the drift current is equal to the diffusion current, the built-in potential can be derived. The current density of the holes can be written as:

$$J_p = q(\mu_p pE + D_p \frac{dp}{dx}) \qquad (2.1)$$

and the current density of the electron as:

$$J_n = q(\mu_n nE + D_n \frac{dn}{dx}) \qquad (2.2)$$

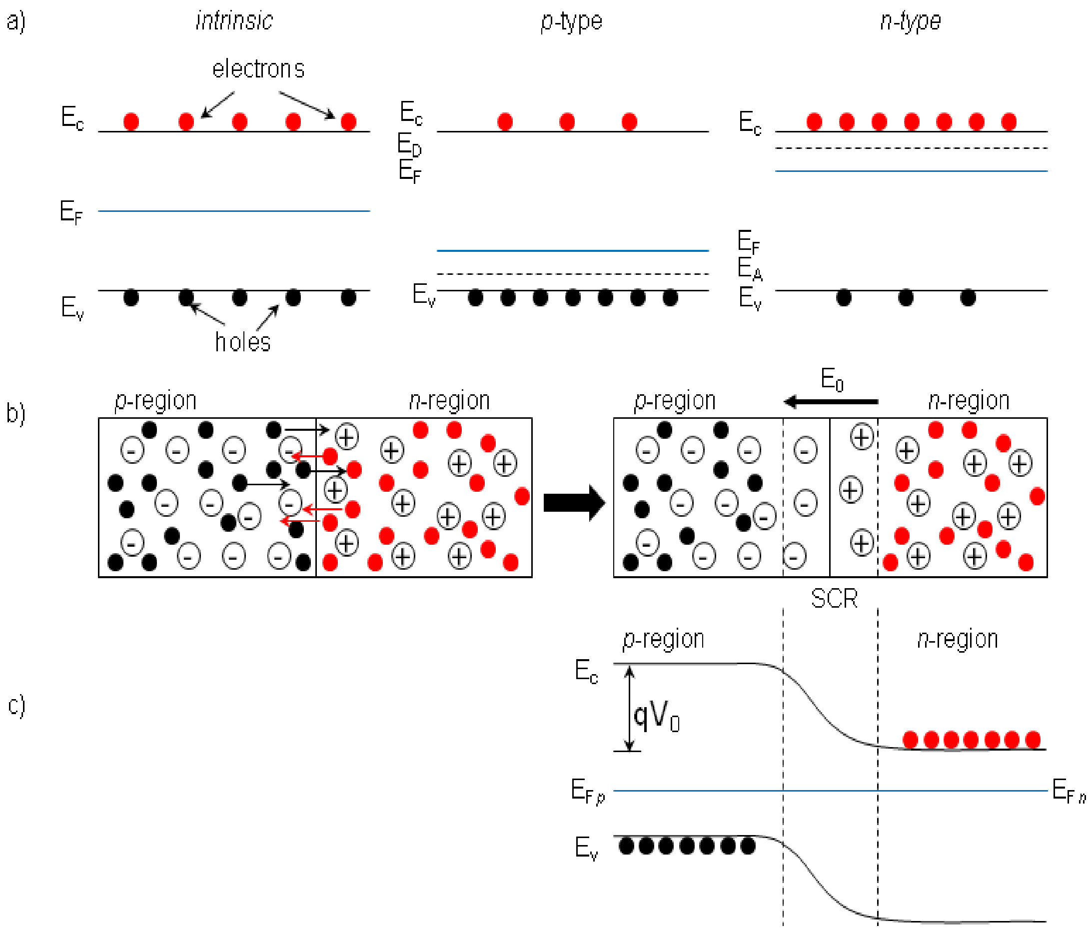

Figure 2.2: Band structure of intrinsic, p-type, and n-type semiconductors, showing the positions of Fermi, donor, and acceptor levels (a); formation of the p-n junction (b); and the energy band diagram of the p-n junction (c).

From both equations, and without going in the derivation details, the built-in potential can be written as:

$$V_0 = V_T \, ln(N_D N_A / n_i^2) \qquad (2.3)$$

Here, μ indicates the mobility of the charge carriers, q is the elementary charge, D is the diffusion coefficient, E is the electric field intensity, and p and n represent the concentration of holes or electrons, respectively. Furthermore, N_A and N_D denote the acceptor and donor concentration, n_i is the intrinsic carrier density, and V_T is the thermal voltage, which is equal to $k_B T/q$ with k_B, T, and q representing Boltzmann constant, temperature, and charge of the carrier, respectively.

By applying an external voltage ($V = V_{pn}$) to the p-n junction, the thermodynamic equilibrium is disturbed so that the drift and diffusion currents no longer compensate each other. We differentiate between forward ($V_{pn} > 0$) and reverse ($V_{pn} < 0$) biasing of the p-n junction.

In case of forward bias, the potential difference within the space-charge zone is reduced by the amount of the applied voltage ($V_0 – V$). Here, holes are injected from the p- to n-type region and electrons are injected from the n- to p-type region. The injected minority carriers recombine at the edges of the space-charge region with the respective majority carriers. The total current is the sum of the minority-carrier diffusion currents of holes in the n-region and electrons in the p-region.

If the applied voltage is negative ($V_{pn} < 0$), then the potential difference applied to the now wider space-charge region increases by V_{pn} to ($V_0 + V$). As a consequence of the increased voltage, the generated electron-hole pairs will be separated at the edges of the space-charge region and the minority carriers are extracted via the space-charge region. The drift current remains unchanged and a constant small reverse current flows in reverse direction. Figure 2.3 illustrates the energy band diagram of the p-n junction under forward and reverse bias.

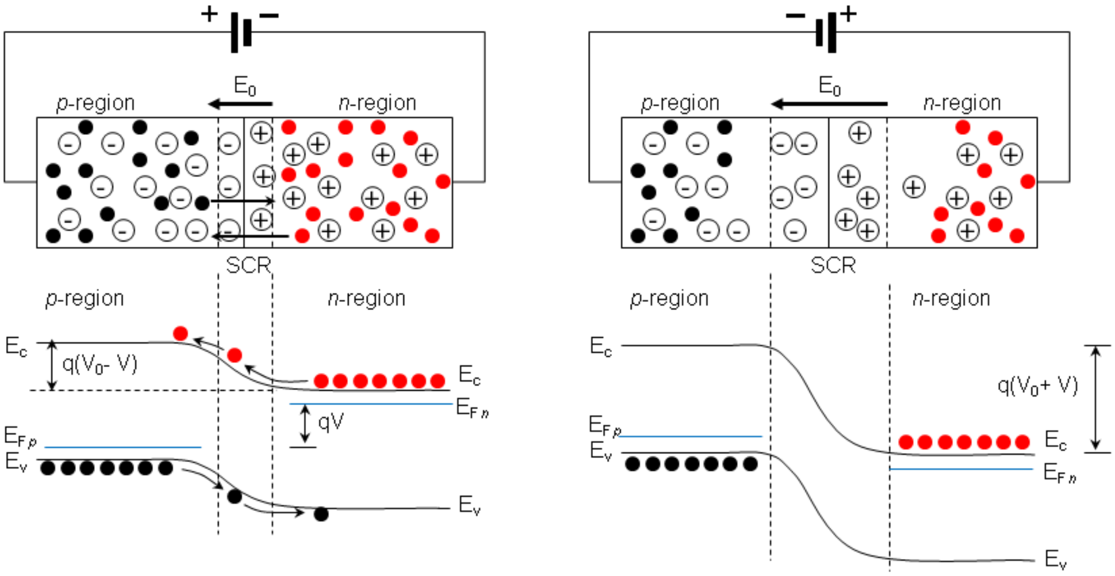

Figure 2.3: Energy band diagram of the p-n junction under forward bias (left) and reverse bias (right).

The current-voltage behavior of the p-n junction is described by the diode equation, which can be analytically calculated under the following conditions:

a) The voltage drop across the n- and p-type regions is negligible compared with the voltage drop across the space-charge zone.

b) Weak injection exists.

c) Generation and recombination in the space-charge region are neglected.

The complete mathematical derivation of the current-voltage characteristic can be found, e.g., in [18]. Without providing the derivation, the ideal diode equation is defined as:

$$I = I_0[exp(V/V_T - 1)] \qquad (2.4)$$

with

$$I_0 = A\left[\frac{qD_n n_i^2}{L_n N_A} + \frac{qD_p n_i^2}{L_p N_D}\right] \qquad (2.5)$$

Here, A is the area of the diode, and L_p and L_n are the diffusion lengths of the holes and electrons, respectively.

2.1.3 The solar cell

Figure 2.4 shows a cross section of a typical silicon solar cell consisting of a p-doped silicon wafer as a base. For the formation of the p-n junction, a narrow n-doped layer (emitter) is produced on the front of the device by diffusion of elements from group V of the Periodic table such as phosphorus (P) or arsenic (As).To reduce the optical losses, an antireflection layer is deposited on top of the emitter. For contacting the cell, the entire back area is covered with aluminum, whereas on the front, silver contact fingers are applied but are narrow to minimize the shading of the underlying material.

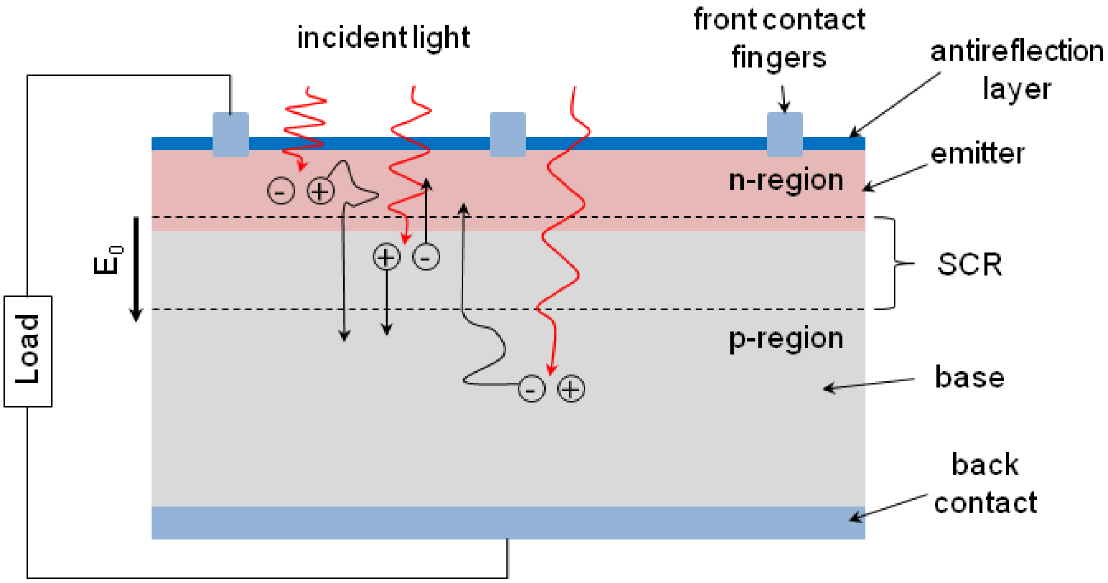

Figure 2.4: Schematic cross-sectional illustration of a silicon solar cell. SCR = space-charge region.

When the solar cell is illuminated, light with photon energy ($E_{ph} = hc/\lambda$) equal to or greater than the bandgap of the semiconductor material will be absorbed, and electron-hole pairs (EHPs) are generated. Because the n-type layer is very thin, most of the incident photons will be absorbed in the SCR and in the wider p-type layer (bulk).

If the EHPs arrive at the space-charge region without recombining, they will be separated by the electrical field so that the electrons drift into the emitter and holes into the base. The ideal current-voltage (I-V) equation of a solar cell is given by:

$$I = I_0[exp(V/V_T - 1)] - I_{ph} \qquad (2.6)$$

Here, I_{ph} is the photocurrent generated by the illumination of the cell.

2.1.3.1 Characteristic parameters of a solar cell

As shown in Figure 2.5, the photocurrent causes a shift of the dark curve downward by the amount of I_{ph}. The maximum current is obtained when the solar cell is short-circuited, i.e., when V = 0. This current is called the short-circuit current, I_{sc}. From Equation 2.6, I_{SC} can be written as:

$$I_{sc} = -I_{ph} \qquad (2.7)$$

The open terminal voltage is obtained when (I = 0) in Equation 2.6. It is called the open-circuit voltage, V_{oc}, and can be written as:

$$V_{oc} = V_T ln(I_{ph}/I_0 + 1) \qquad (2.8)$$

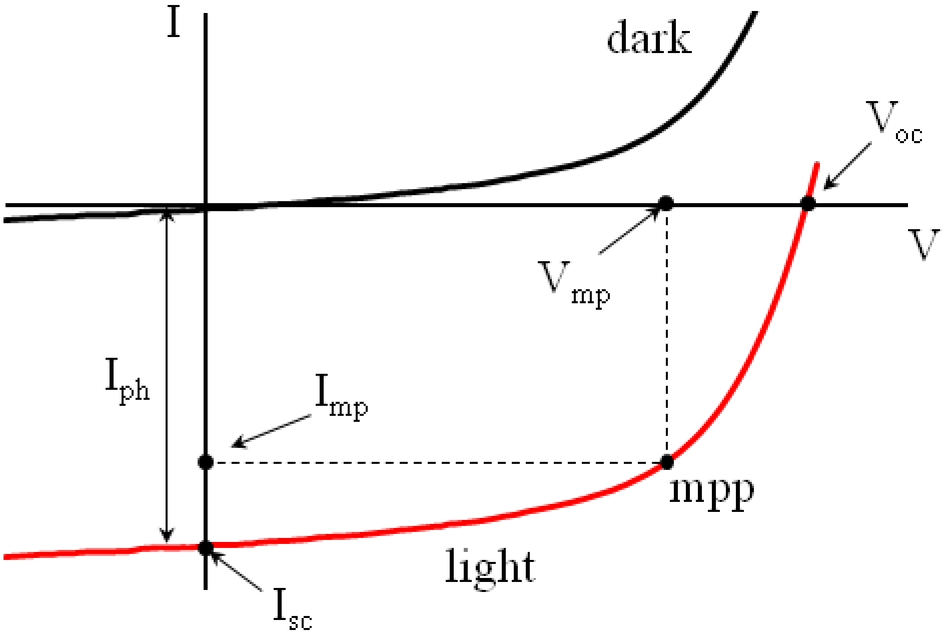

Figure 2.5: Dark and light curve of the solar cell.

The maximum power output of the solar cell is obtained at the maximum power point (mpp), and the ratio of the maximum power ($P_{mp} = V_{mp} \cdot I_{mp}$) to the product ($V_{oc} \cdot I_{sc}$) is called the fill factor (FF) and is defined as:

$$FF = \frac{V_{mp} I_{mp}}{V_{oc} I_{sc}} \qquad (2.9)$$

The efficiency of a solar cell is defined as the ratio between the electrical power output at the maximum operating point and the incident light power. It measures the fraction of incident light that is converted into electrical power:

$$\eta = \frac{V_{mp} I_{mp}}{P_L} = \frac{FF I_{sc} V_{oc}}{P_L} \qquad (2.10)$$

2.1.3.2 Real solar cell (equivalent circuit)

According to Equation 2.6, the solar cell can be realized by a current source (representing the photocurrent) connected in parallel with a p-n junction diode (Figure 2.6 a). However, Equation 2.6 represents an ideal p-n junction that does not consider several parasitic effects that cause a deviation from the ideal behavior. If the parasitic resistances (series and parallel resistances) are taken into account, the equivalent circuit of the solar cell looks like the one illustrated in Figure 2.6 b, and the I-V equation for the solar cell can be extended to:

$$I(V) = I_0\left[exp\left(\frac{V-IR_S}{V_T}-1\right)\right]+\frac{V-IR_S}{R_p}-I_{ph} \qquad (2.11)$$

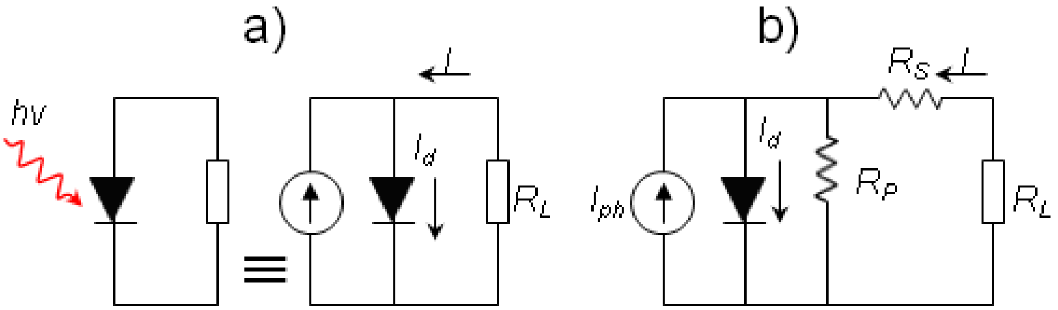

Figure 2.6: Equivalent circuit of ideal a) and real b) solar cell, RL represent the external load to the cell.

The series resistance R_s comprises a number of individual resistances in the solar cell, including the following components:

- Contact resistance between the semiconductor material and the metal contacts

- Ohmic resistance in the metal contacts

- Ohmic resistance in the semiconductor material (sheet resistance of the n-layer and volume resistivity of the base)

The parallel resistance R_p (also called shunt resistance R_{sh}) represents carrier leakage at the edges of the solar cell and disorders of the p-n junction. A contact between the finger electrodes and the p-layer can be formed by these leakage currents or by the interruption of the p-n junction; this situation can result in short circuits.

The influences of the serial and parallel resistances to the parameters of the solar cell are shown in Figure 2.7. It can be clearly seen that even with a small change of both parameters, the fill factor of the cell is greatly affected. The open-circuit voltage decreases with the decrease of the parallel resistance whereas the short-circuit current is not affected. In contrast, large values of series resistance affect the short-circuit current, but not the open-circuit voltage. The losses caused by the two types of resistances are called ohmic losses and belong to the electrical losses that occur within the solar cell. In addition, there are other loss mechanisms, including optical losses and losses caused by different kinds of recombination of the charge carriers.

2.1.3.3 Optical losses in the solar cell

When the solar cell is irradiated, a part of the incident light is reflected by the metal contacts that shade a portion of the front surface, thus not contributing to the generation of electron-hole pairs. Another part of the incident light is reflected at the front surface itself. An antireflection coating can be deposited on the emitter based on the principle of “optical quarter-wavelength” [17] to reduce the reflectance at the surface:

$$n.d = \lambda/4 \qquad (2.12)$$

Here, n is the refractive index and d is thickness of the antireflection layer, and λ is the wavelength at which the reflection should be minimal.

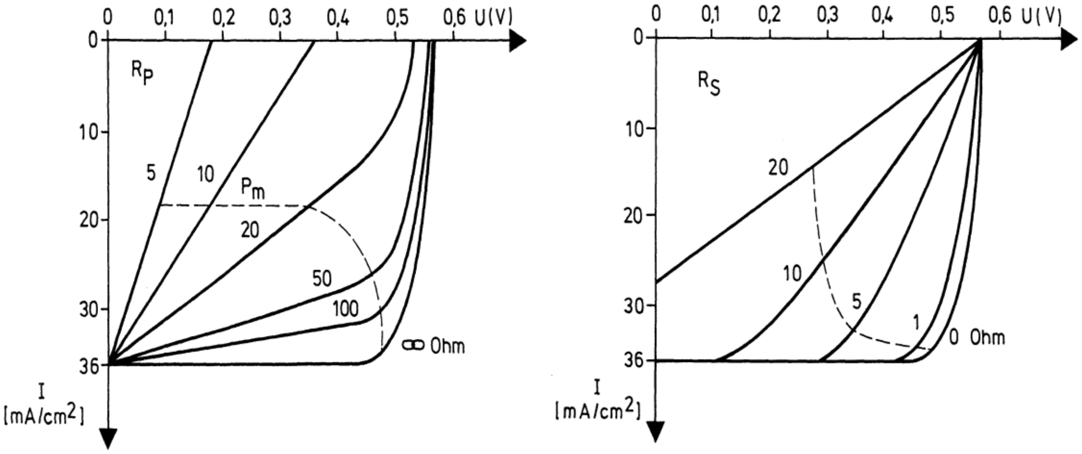

Figure 2.7: Influence of the parallel (left) and series (right) resistances on the solar cell parameters [17].

2.1.3.4 Recombination

The reverse process of the generation of electron-hole pairs is called recombination, in which, for example, the previously photogenerated electron-hole pairs destroy each other before they can be collected at the external cell electrodes. When an electron falls from the conduction band to the valence band, it recombines with a hole and the released energy is emitted as a photon, phonon, or is given to another charge carrier.

Recombination processes in semiconductors are divided into intrinsic and extrinsic recombination. Intrinsic transitions, including band-band and band-band Auger recombination, are unavoidable and occur even in defect-free semiconductors. In contrast, extrinsic transitions are caused by lattice defects or impurities in the semiconductor material (recombination via impurity).

Lattice defects or impurity atoms with energy transition levels within the bandgap of the semiconductor build recombination centers that act as traps for the charge carriers. Thus, the recombination process reduces the total amount of free-charge carriers and will directly affect the short-circuit current of the device and also impact the open-circuit voltage. As a consequence, the FF will also be reduced. Therefore, producing semiconductor materials with minimal impurities is very important for obtaining solar cells with high efficiencies. If the recombination phenomena are considered, the ideal solar cell equation can be written as:

$$I = I_0[exp(V/nV_T - 1)] - I_{ph} \qquad (2.13)$$

where n is called the ideality factor of the solar cell. For a Si solar cell, n takes values between 1 and 2.

2.2 Thin-Film Solar Cells

The first generation of solar cells is based on monocrystalline and multicrystalline silicon, which is a semiconductor with an indirect energy bandgap of 1.12 eV. The material exhibits numerous advantages, and the technology for producing and processing silicon wafers with a high degree of purity is well developed. The efficiency of the first reported (1941) solar cell based on multicrystalline silicon (mc-Si) was about 1% [19]. Over the years, the efficiency of Si solar cells evolved rapidly, approaching its theoretically predicted maximum of about 32%. In 2014, a record efficiency of 25.6% was achieved for a laboratory-produced single-crystalline Si cell [20]. The record device has an area of 143.7 cm^2 and exhibits a short-circuit current density (J_{sc}), V_{oc}, and FF of 41.8 mA/cm^2, 750 mV, and 82.7%, respectively. For mc-Si cells, Trina Solar announced a new efficiency record of 21.25% in late 2015. The cell has an area of 156×156 mm^2, V_{oc} of 667.8 mV, J_{sc} of 39.80 mA/cm^2, and FF of 80% [21], [22]. Silicon-based PV is still the dominant technology in the solar field, accounting more than 90% of total production. However, the price of electricity produced by PV is still high compared to that from other sources. One of the factors contributing to the high production cost of Si solar cells is the amount of material used. About 61% of the solar cell price is accounted by the Si wafer [23]. Due to the relatively small absorption coefficient of silicon (100 cm^{-1}), which is related to the indirect bandgap of the material, the device must have a thickness of about 100–200 μm to absorb most of the incident solar radiation and provide reasonable mechanical strength. Reducing the wafer thickness was one of the solutions applied to decrease the cost of PV-produced energy, and as of today, 180-μm-thick wafers are used. Further cost reduction requires the use of less expensive materials and technologies.

The second generation of solar cells based on thin-film technology has emerged as an alternative to the conventional Si cells. Thin-film PV provides a solution to reduce the amount of material used by employing direct-bandgap semiconductors with higher absorption coefficients; thus, the total thickness of the solar cell is in the range of a few microns. The device is fabricated on inexpensive substrates (e.g., glass, plastic, metal foils) to provide the necessary mechanical strength, and the synthesis process does not require a high degree of purity, unlike the case of Si cells. Therefore, the synthesis process of thin-film PV devices using different kinds of deposition methods is simpler and less expensive. Thin-film solar cells are based generally on heterojunctions using differently doped, dissimilar materials—where typically, a thin n-type semiconductor as a buffer layer is deposited on top of a p-type semiconductor, which represents the active absorber layer to form the p-n junction. A p-type material is preferred for the active absorbing layer, where the EHPs are generated, because the diffusion length of electrons in a p- type semiconductor is larger than the diffusion length of holes in an n-type semiconductor. The n-type layer must be thin and made of a wide-band material to enable the incident light to pass through to the absorber layer. For that, a CdS layer about 50 μm thick with an energy bandgap of 2.4 eV is commonly used. Two strong representative materials for thin-film solar cells that show device efficiencies comparable to those of mc-Si cells are cadmium telluride (CdTe) and copper indium-gallium diselenide, $Cu(InGe)Se_2$ (CIGS). Both materials have reached the commercialization stage for mass production. In addition, amorphous silicon (a-Si) solar cells are mass produced. Despite a-Si devices' low efficiency compared to CdTe and CIGS cells, they have application due to their low-cost production where low efficiencies are acceptable. We provide a brief review of the three technologies below.

2.2.1 Amorphous silicon

Amorphous silicon (a-Si) thin films are deposited at low temperatures commonly via plasma-enhanced chemical vapor deposition (PECVD) using silane (SiH_4) gas [24], [25]. Thus, a-Si can be produced on a variety of substrates including glass, plastic, or metal foils. The material exhibits non-crystalline structure (i.e., atoms are randomly arranged), which impacts the electronic properties of the semiconductor. To improve the quality of the material for PV applications, hydrogen is incorporated to passivate the dangling bonds that result from the random arrangement of the atoms. Compared to crystalline Si, the hydrogenated amorphous silicon (α-Si:H) exhibits a direct bandgap of 1.7 eV and an optical absorption coefficient $\alpha > 10^5$ cm^{-1}, enabling the absorption of most solar radiation within a few micrometers. The first α-Si:H cell of a thickness of about 1 μm with an efficiency of 2.4 % was made in 1976 by using a p-i-n a-Si structure [26]. The device can be realized as a single junction or multijunction (double or triple) with a superstrate (p-i-n) configuration (i.e., light penetrates through the substrate) or substrate (n-i-p) configuration (i.e., light penetrates through the top n-layer). Cross-sectional illustrations of single- and double-junction a-Si p-i-n cell structures in superstrate configuration are shown in Figure 2.8. The charge carriers are separated by the electric field created across the absorber intrinsic layer by the p- and n-layers. Cells based on a-Si suffer mainly from performance degradation when exposed to sunlight, a phenomenon known as the Staebler-Wronski effect (SWE) [27]. Through continued research over the last years to stabilize the efficiency of a-Si:H cells, the record device for a single junction shows stabilized efficiency of 10.2% [28]. Using a multijunction structure, the record device exhibits stabilized efficiency of 13.6 % [29].

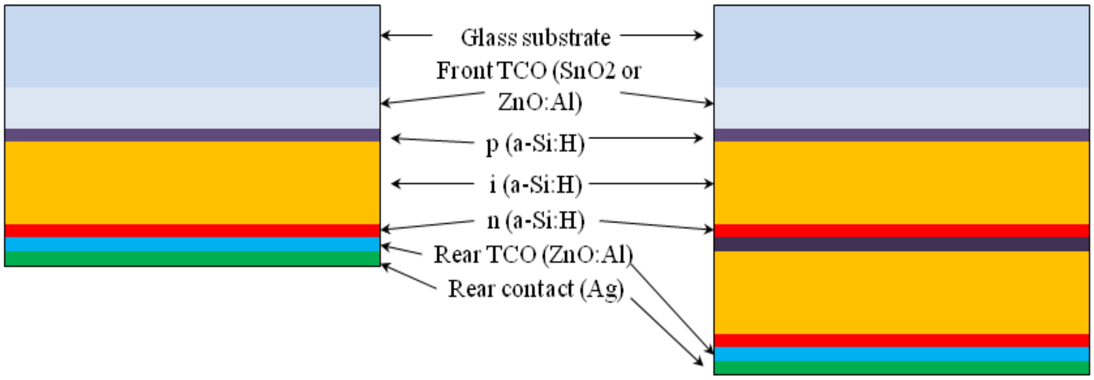

Figure 2.8: Cross-sectional illustration of typical single- and double-junction a-Si:H solar cells in a superstrate configuration.

2.2.2 Cadmium telluride (CdTe)

Cadmium telluride has long been recognized as an optimal candidate for thin-film PV applications [30] because it is a chemically stable semiconductor compound with large absorption coefficient ($>10^4$ cm^{-1}) and a direct bandgap of about 1.45 eV [31], [32]. The material can be doped both as p- or n-type; however, the absorber layer of the CdTe solar cell is a p-type semiconductor. Typically, CdTe devices are fabricated in superstrate configuration, where a transparent conducting oxide (TCO) as a front contact is first deposited on a glass substrate, followed by an n-type CdS window layer that forms the heterojunction with the p-type CdTe layer. The absorber CdTe layer is then deposited on the CdS layer at temperatures between 400 °C and 600 °C using different deposition routes—including close-spaced sublimation (CSS), which is a thermal evaporation method [33], [34]; electrodeposition [35]; sputtering [36]; and screen printing [37]. Finally, a metal film as the back contact is deposited on the CdTe layer. A schematic illustration of a conventional CdTe/CdS solar cell is shown in Figure 2.9. The PCE of CdTe-based solar cells has increased in the last few years to exceed 20%. In a February 2016 press release, First Solar announced a new world record of 22.1% for a CdTe cell [8].

Despite the progress made in the CdTe technology by achieving cost-effective, high-efficiency devices that can easily compete with mc-Si cells, some issues connected with CdTe solar cells could affect their production in the future. The main issue is the toxicity of cadmium. Another issue is the scarcity of tellurium, which could negatively impact terawatt (TW)-scale production in the future, leading to increased cell and module prices.

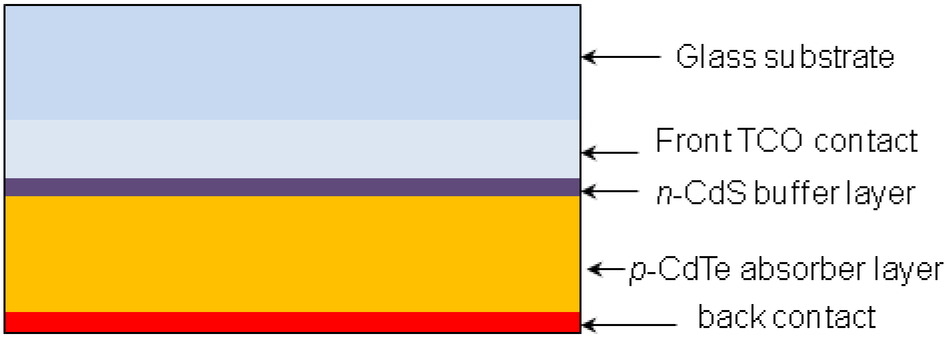

Figure 2.9: Cross-sectional illustration of a CdTe solar cell in a superstrate configuration.

2.2.3 Cu(InGa)Se_2 (CIGS)

Chalcopyrite semiconductor compounds such as copper indium diselenide ($CuInSe_2$), copper gallium indium diselenide ($CuGa_{1-x}In_xSe_2$), and copper indium disulfide ($CuInS_2$) exhibit direct bandgaps and high optical absorption coefficients, making them suitable for PV application. The potential of the CdS/$CuInSe_2$ system as a PV heterojunction was first demonstrated in 1974 [38]. The first thin-film CdS/$CuInSe_2$ heterojunction solar cell fabricated in 1976 by Kazmerski *et al.* showed an efficiency of 4.5% [39]. Later, gallium (Ga) was incorporated in $CuInSe_2$ to produce Cu(InGa)Se_2. The quaternary compound $Cu_2InGaSe_4$ (CIGS) is the most successful chalcopyrite absorber [40], with a record efficiency of 21.7% [9].

CIGS thin films have been produced using different deposition methods including sputtering [41], electrodeposition [42], spray deposition [43], and thermal evaporation [44]; however, most of the CIGS absorber layers of the devices showing the highest efficiencies were deposited by thermal evaporation. Figure 2.10 shows s cross-section of a typical CIGS solar cell. Conventionally, CIGS devices are fabricated in substrate configuration, starting with the deposition of a molybdenum layer as the back contact on a glass substrate. Thereafter, the absorber layer is deposited, followed by an n-type CdS buffer layer that forms the heterojunction with the p-type CIGS. An intrinsic ZnO layer is deposited on top of the CdS, followed by an aluminum-doped ZnO layer that serves as the top contact. Similar to the CdTe technology, indium scarcity represents an issue in CIGS PV applications, where the high price of indium impacts cell and module costs and the material could experience some shortage in the future.

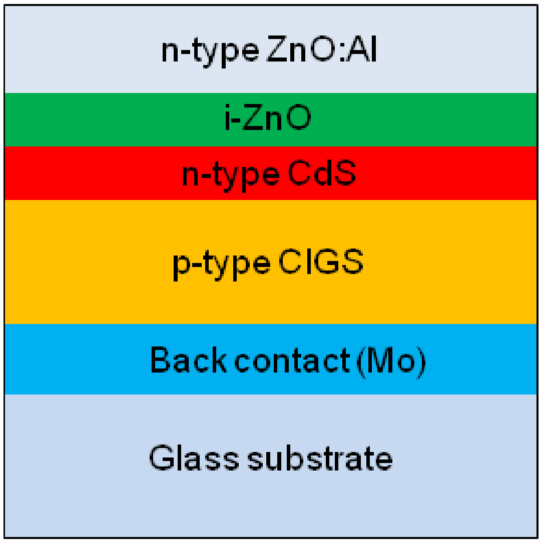

Figure 2.10: Cross-sectional illustration of a typical CIGS cell in substrate configuration.

2.3 Cu_2ZnSnS_4 (CZTS)

2.3.1 Properties of CZTS

2.3.1.1 Crystal structure

The quaternary compound Cu_2ZnSnS_4 can be derived from II-VI compounds such as zinc-blende (ZnS). By replacing two group-II atoms with one group-I and one group-III atoms, we obtain a I-III-VI_2 semiconductor such as the Cu-based chalcopyrite $CuInS_2$

(CIS). Then, by replacing half of the In atoms with group-II atoms such as Zn and the other half with group-IV atoms such as Sn, we can produce Cu_2ZnSnS_4. Similarly, the $Cu_2ZnSnSe_2$ compound can be derived from CuInSe. Figure 2.11 illustrates the derivation of CZTS from ZnS.

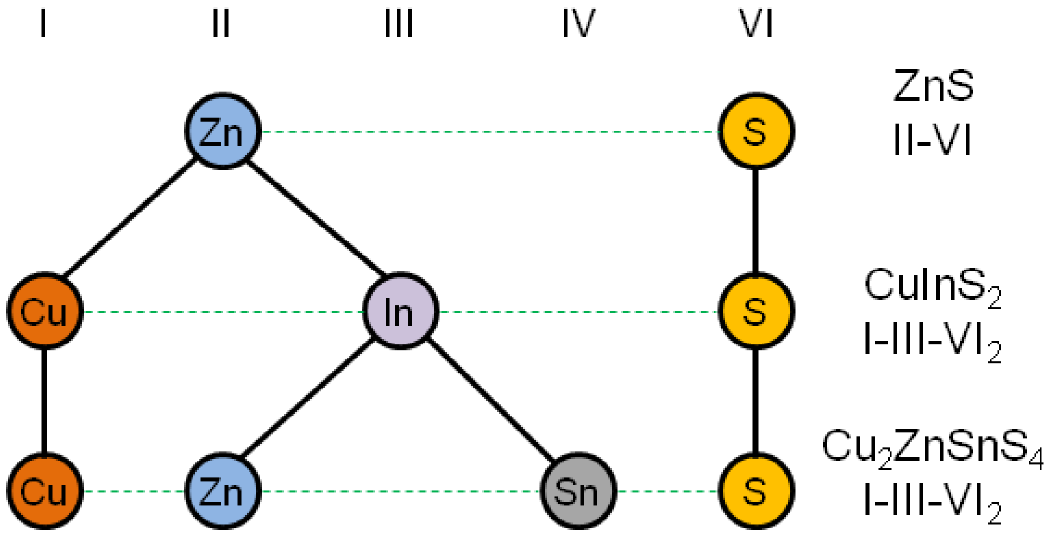

Figure 2.11: Derivation of the quaternary CZTS compound from binary and ternary compounds.

Experiments show that CZTS and CZTSe crystallize in two main structure forms: kesterite (KS)-type structure (space group $I\bar{4}$) and stannite (ST)-type structure (space group $I\bar{4}2m$) [45]–[48]. Furthermore, a primitive mixed CuAu (PMCA) structure may form in addition to kesterite and stannite. In contrast, theoretical studies based on density functional theory (DFT)—an *ab-initio* quantum mechanical method used for calculating the total energy and electronic structure—showed that the KS structure is more stable than the ST structure [49]–[51]. Although the kesterite structure is more likely to form, the small calculated total energy difference $\Delta Et = Et(\mathrm{ST}) - Et(\mathrm{KS})$ of about 3 meV/atom indicates that KS and ST ordering may coexist in the synthesized samples [48], [52]. Slightly different values for the total energy difference $\Delta\mathrm{Et}$ were also reported in the literature [49]–[51], [53]. Using neutron and X-ray diffraction, Schorr *et al.* [54] found that CZTS and CZTSe crystallize in the kesterite-type structure with a disorder within the Cu–Zn layers at z = ¼ and ¾. With theoretical and experimental results agreeing that kesterite is the more stable type of structure, the synthesized stannite CZTS films reported earlier in the literature are indeed believed to be disordered kesterites.

Both forms, KS and ST, exhibit tetragonal structure with different arrangements of Cu and Zn. In the kesterite-type structure, the cation layers CuSn, CuZn, CuSn, and CuZn alternate at z = 0, ¼, ½, and ¾, respectively, whereas ZnSn layers alternate with Cu_2 layers in the stannite-type structure. In both structures, Sn and sulfur occupy the same lattice positions. The crystal structures of kesterite and stannite CZST are illustrated in Figure 2.12. Calculated and experimentally measured values for the lattice constant 'a' of the KS and ST tetragonal unit cells are on the order of 5.4 Å, whereas the ratio c/a is close to 2. Table 2.1 lists some of the theoretically calculated and experimentally determined lattice constant values of CZTS and CZTSe reported in the literature.

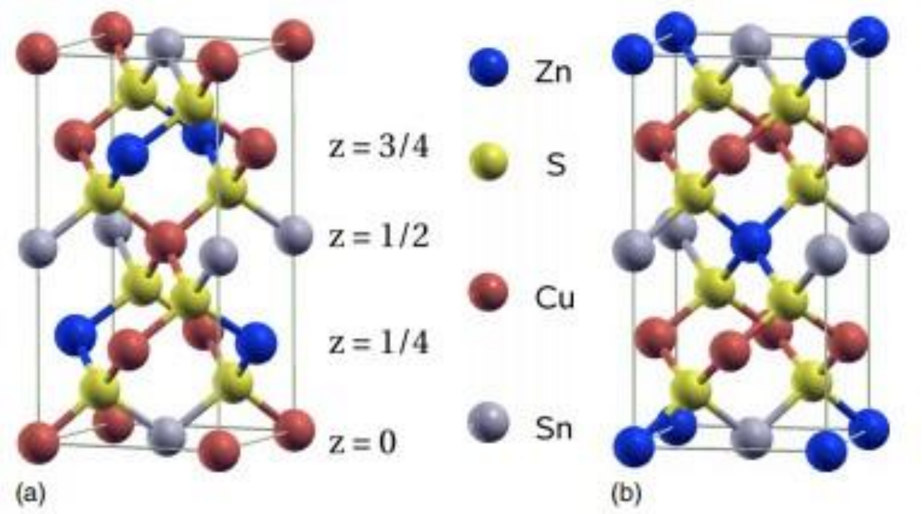

Figure 2.12: CZTS unit cells of kesterite-type a) and stannite-type b) structures [51].

Table 2.1: Lattice constants of CZTS and CZTSe determined by calculations and measurements.

	Structure	a (Å)	c (Å)	Reference	Year
Calculated	KS CZTS	5.47	10.92	[49]	2009
		5.45	10.89	[51]	2009
		5.51	11.23	[55]	2009
		5.33	10.66	[53]	2010
		5.35	10.73	[56]	2015
	KS CZTSe	5.73	11.43	[57]	2010
	ST CZTS	5.458	10.96	[49]	2009
		5.44	10.941	[51]	2009
	ST CZTSe	5.738	11.453	[50]	2012
Measured	KS CZTS	5.43	10.87	[47]	1978
		5.42	10.85	[58]	2009
		5.43	10.86	[59]	2010
		5.425	10.84	[60]	2016
	KS CZTSe	5.68	11.36	[61]	2008
	ST CZTS	5.436	-	[11]	1996

2.3.1.2 Electronic band structure

Calculations based on different methods show that both compounds, CZTS and CZTSe, exhibit comparable band structures with direct bandgaps at the Γ-point. Figure 2.13 shows the calculated electronic band structure of kesterite CZTS along the two symmetry directions (110) and (001). The theoretically calculated bandgap values of KS CZTS reported in the literature are in the range of 1.47–1.64 eV [49]–[51], [53], [56], [62], in fair agreement with the experimentally estimated bandgap of about 1.5 eV [10], [45], [46], [63]–[65]. Experimentally, the bandgap is determined using optical transmission measurements or quantum efficiency measurements in solar cells. Deviations of the 1.5-eV value have been also reported [66]. Some studies announced variation in the bandgap by changing the material composition or using different sulfurization conditions [67]–[70]. For the bandgap of CZTSe, on the contrary, experimentally determined values of about 1.5 eV [71]–[75] differ significantly from theoretically estimated values and also some experimentally determined values of about 1 eV [13], [49], [76], [77]. Ahn *et al.* [78] reported on the discrepancies of bandgap values of CZTSe reported in the literature. They demonstrated experimentally that the discrepancies are due to the presence of ZnSe phase in the synthesized films, suggesting that a secondary-phase-free CZTSe compound has a bandgap of 1 eV. Further tuning of the bandgap, realizing values between 1.0 (pure selenide) and 1.5 eV (pure sulfide), can be achieved by varying the sulfur-to-selenium ratio in the related alloy $Cu_2ZnSn(S_xSe_{1-x})_4$ (CZTSSe) [79]. Wei *et al.* demonstrated tuning of the bandgap of CZTSSe nanocrystals from about 1.28 to 1.50 eV by varying the Se/(S + Se) ratio [80].

CZTS and its related compounds have an optical absorption coefficient (α) larger than 10^{-4} cm^{-1} in the visible region of the electromagnetic spectrum [10], [58], [81], enabling the absorption of the incident light with energies higher than the bandgap in only a few microns.

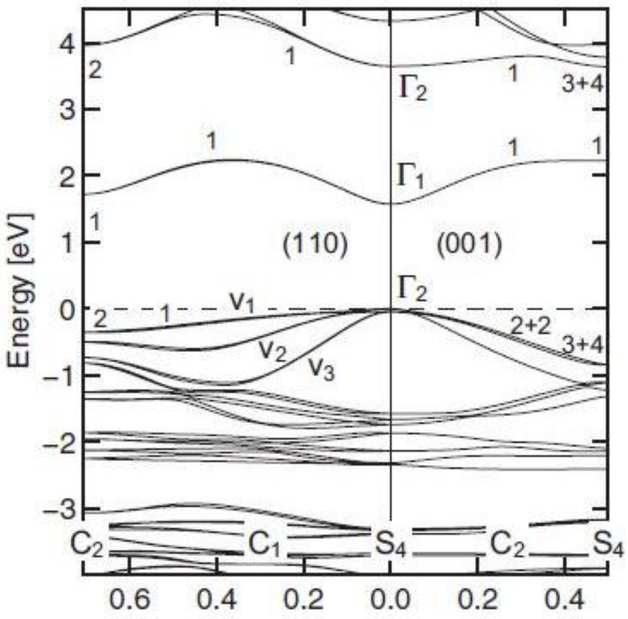

Figure 2.13: Calculated electronic band structure of kesterite CZTS along the two symmetry directions (110) and (001) [53].

2.3.1.3 Intrinsic defects

Defects in semiconductors play an important role because they affect many of their optical and electronic properties [82]. They control the material doping, change the bandgap, and influence the recombination properties of the solar cell.

CZTS and its related alloys, as quaternary semiconductors, have several intrinsic defects that can form during the compound growth. These include Cu, Zn, Sn, and S vacancies (V_{Cu}, V_{Zn}, V_{Sn}, and V_S), antisites Cu_{Zn}, Zn_{Cu}, Cu_{Sn}, Sn_{Cu}, Zn_{Sn}, and Sn_{Zn} (Cu_{Zn}: copper on Zn site), and interstitials (Cu_i, Zn_i, Sn_i, and S_i). In addition, acceptor and donor defects may compensate and form defect clusters such as (V_{Cu} + Zn_{Cu}) and ($2Cu_{Zn}$ + Sn_{Zn}).

Hot-probe method and Hall effect measurements showed that synthesized CZTS films exhibit spontaneously p-type conductivity [11], [46], [83]–[85]. Defect formation studies using first-principles calculations revealed that the p-type conductivity of CZTS is due to the Cu_{Zn} antisite defect, which exhibits the lowest formation energy among all intrinsic defects [86]–[88]. This finding differs from the chalcopyrite case, where the p-type self-doping ability of $CuInSe_2$ is attributed to the shallow-defect Cu vacancies V_{Cu} with the lowest formation energy [89].

Chen *et al.* [86] calculated the formation energies of a series of intrinsic defects and defect complexes in CZTS as a function of the atomic chemical potentials of the constituent elements. Under Cu-poor condition, five of the 13 possible point defects—namely, Cu_{Zn}, Cu_{Sn}, Zn_{Sn}, V_{Cu}, and V_{Zn}—showed relatively low formation energies (lower than 1 eV). The low formation energies of the acceptor defects compared to the relatively higher formation energies of the donor defects suggest that n-type doping of the kesterite CZTS compound is unlikely. The calculated transition-energy levels of the intrinsic defects within the bandgap of Cu_2ZnSnS_4 are listed in Figure 2.14.

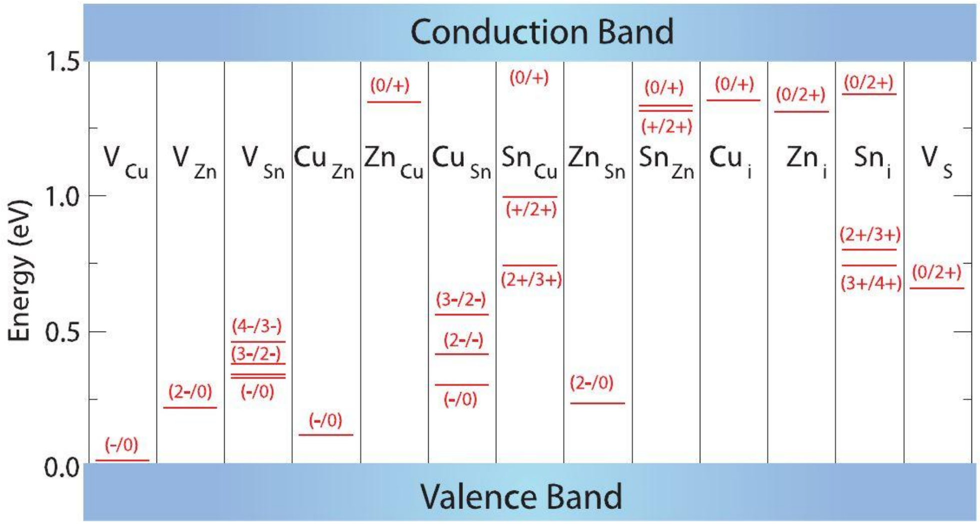

Figure 2.14: Calculated transition energy levels of intrinsic defects in the bandgap of Cu_2ZnSnS_4 [90]. The transition level ($\epsilon_X(q/\acute{q})$) of a defect X is defined as the Fermi level positions at which the formation energies of the defect in two different charge states are equal; hence, $\epsilon_{V_{Cu}}(-/0)$ is the Fermi level at which the formation energy of V_{Cu}^{-} and V_{Cu}^{0} are equal.

Low-formation-energy defects exhibiting deep transition levels in the bandgap could be detrimental to solar cell performance. The Cu_{Zn} acceptor level is predicted to lie about 0.12 eV above the valence band maximum (VBM), whereas the V_{Cu} acceptor has a shallower level at 0.02 eV above the VBM. The ionization level of Cu_{Zn} antisite was later recalculated to be 0.15 eV [91]. The low formation energy of the Cu_{Sn} defect has a deeper level close to midgap and is expected to represent the most active recombination center [86]. Using hybrid functional calculation, Han *et al.* [92] predicted that the Sn_{Zn} antisite and the defect complex $(Cu_3)_{Sn}$ are the major deep electron traps in the bandgap of CZTS. Despite the discrepancy in predicting the most active recombination center defect, both works provide an explanation to the optimal Cu-poor and Zn-rich growth condition of the CZTS absorber layer mentioned in several experimental works leading to solar cells with higher efficiencies. Low Cu concentration in the compound will lead to less concentration of the defects reported in both studies as detrimental for the device.

First-principles calculations also showed that charged-compensated defect clusters such as $(Cu_{Sn}+Sn_{Cu})$ could form in the CZTS compound and passivate the deep donor levels in the bandgap [86]. The same calculation showed that the defect complex $(Cu_{Zn} +Zn_{Cu})$ has the lowest formation energy among all defect clusters, indicating its high population in the material. This explains the structure disorder in the kesterite Cu-Zn layer reported in [54]. In a later published work, Chen and co-workers [93] reported on the abundance of $Cu_{Zn}+Sn_{Zn}$ and $2Cu_{Zn}+Sn_{Zn}$ defect clusters, which exhibit low formation energies that indicate their high population in stoichiometric composition. The $Cu_{Zn}+Sn_{Zn}$ defect was predicted to produce a deep donor level in the bandgap and the $2Cu_{Zn}+Sn_{Zn}$

defect to decrease the bandgap of the CZTS semiconductor, introducing a detrimental effect on solar cell performance. However, the formation of both defect complexes can be reduced in samples grown under Cu-poor, Sn-poor, and Zn-rich condition. The results provide a clear explanation for the high efficiencies of kesterite cells fabricated under Cu-poor, Sn-poor, and Zn-rich composition.

2.3.2 Single-phase stability and controlling CZTS chemical composition

Synthesizing a single-phase crystal is required to achieve high-quality material. However, controlling the phase stability of a quaternary compound such as Cu_2ZnSnS_4 and $Cu_2ZnSnSe_4$ is relatively challenging because of the following. On one hand, it contains four constituents, each of which can be varied independently. On the other hand, detailed analysis of the phase equilibria of the quasi-ternary system Cu_2S–ZnS–SnS_2 conducted by Olekseyuk *et al.* [94] showed that single-phase CZTS only exists in a very small region of composition, and a small deviation from the stoichiometric composition will lead to the formation of additional binary and/or ternary secondary phases in addition to the CZTS in the synthesized compound. Here, note that the phase diagram was developed for an equilibrium at 400 °C. Scragg *et al.* [95] suggested a simplified ternary phase diagram based on the study of Olekseyuk and on the assumption that the sulfur content in the synthesized film is not an independent variable. Figure 2.15 shows the ternary phase diagram for the Cu-Zn-Sn system, illustrating the narrow region of stoichiometry and the expected secondary phases that can form at 400 °C. The ratios Cu/(Zn+Sn) and Zn/Sn are widely used in the literature to represent the metal composition of the deposited CZTS films. For stoichiometric CZTS, the ratios Cu/(Zn+Sn), Zn/Sn, and S/metals should exhibit unity.

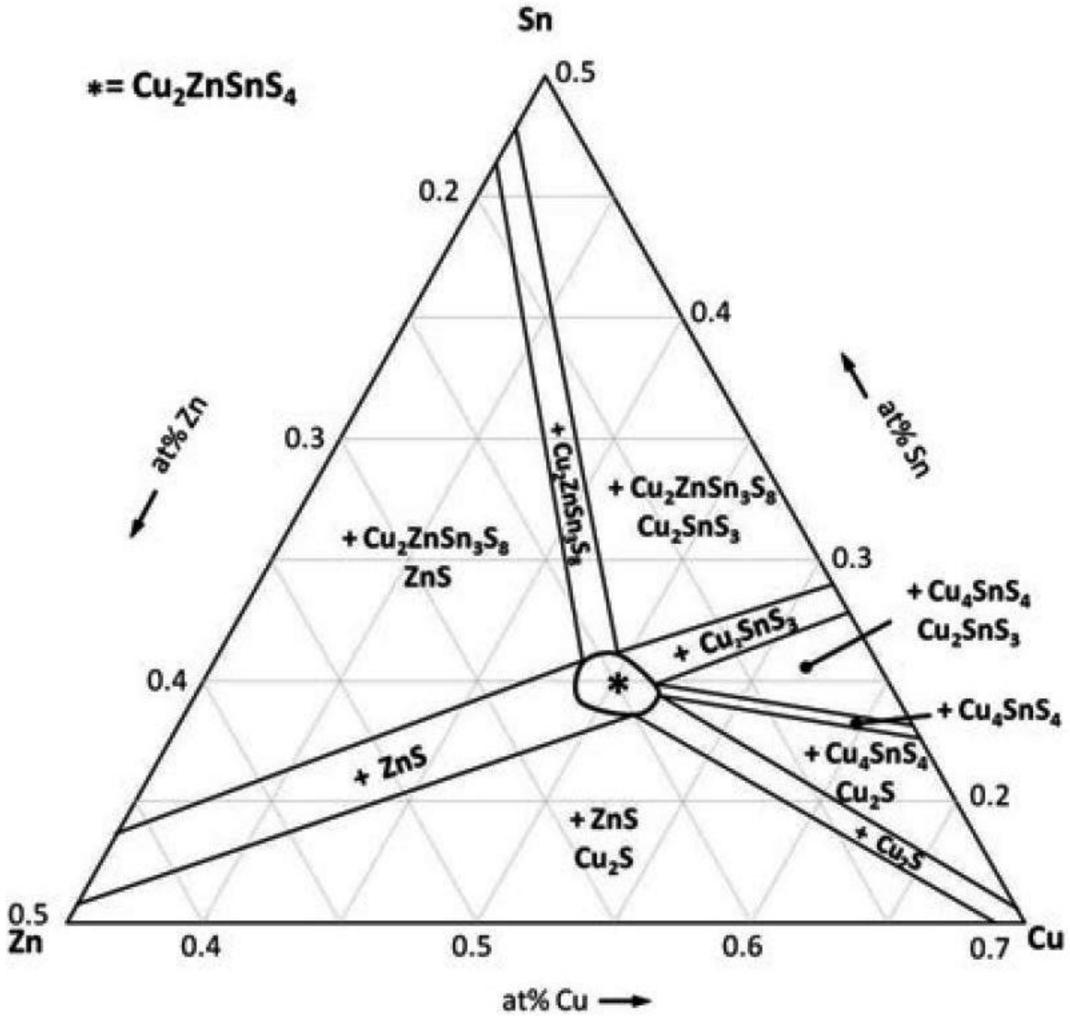

Figure 2.15: Ternary phase diagram for the Cu-Zn-Sn system, showing the expected secondary phases at 400 °C [95].

Experimentally, Muska *et al.* [96] announced that single-phase CZTS can only be grown with metal ratios of Cu/(Zn+Sn) = 0.92–0.95 and Zn/Sn = 1.0–1.03. Using first-principles calculations, theoretical studies based on the calculation of the chemical potentials of the constituent atoms confirmed the narrow regime of stable CZTS [87],

[88]. Figure 2.16 illustrates the calculated chemical-potential stability diagram of Cu_2ZnSnS_4, showing the narrow single-phase stability region (black area). The calculations have also predicted that Cu-rich and Zn-poor conditions are required to achieve single-phase stoichiometric CZTS, contrary to the reported favorable Cu-poor and Zn-rich conditions leading to devices with higher efficiencies [15], [97], [98]. According to the phase diagram, the Cu-poor and Zn-rich growth condition will likely lead to the formation of secondary phases, especially ZnS. The high efficiencies obtained from devices based on CZTS films with Cu-poor and Zn-rich composition were explained with the enhanced formation of copper vacancies and the suppression of the relatively deep-level Cu_{Zn} acceptor [88].

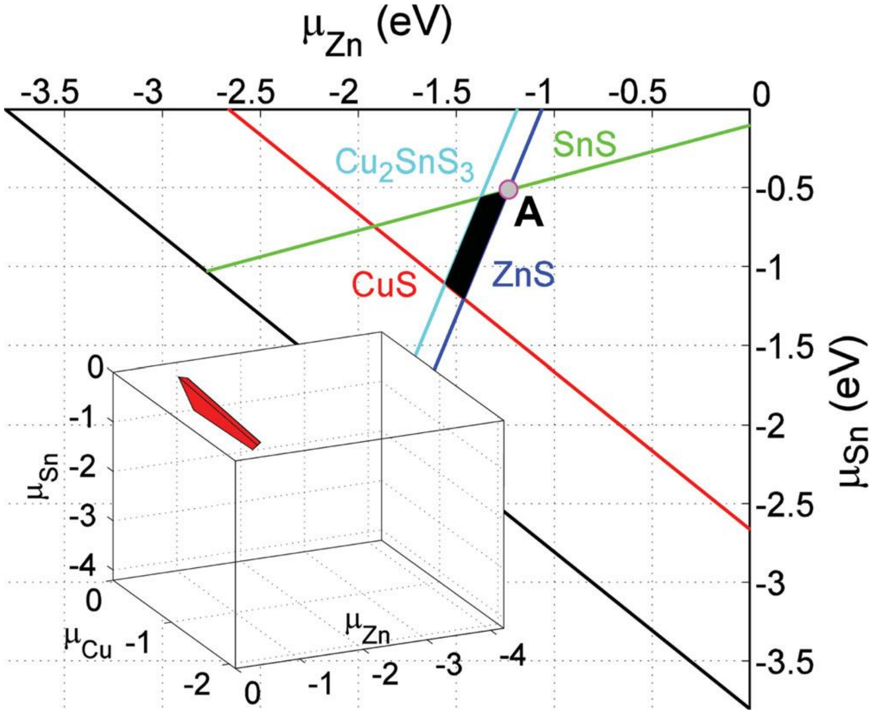

Figure 2.16: The calculated chemical-potential stability diagram of Cu2ZnSnS4 in a 2-D Cu-rich plane (stable 3-D region in inset). All values are in eV [99].

2.3.3 Effect and identification of secondary phases

Due to the small region of composition, binary and ternary secondary phases can easily form in addition to CZTS during the growth process. These phases include ZnS, SnS, SnS_2, CuS, Cu_2S, and Cu_2SnS_3. Formation of secondary phases was reported to be related the film composition [100]. As mentioned in the previous section, the optimal Cu-poor and Zn-rich composition for the CZTS device results in ZnS or ZnSe phases existing in the CZTS or CZTSe compound. Many published works reported the formation of this secondary phase in Cu-poor and Zn-rich composition [101], [102]. ZnS and ZnSe crystallize in the sphalerite and wurtzite structure types exhibiting wide bandgap (about 3.6 eV for ZnS [103]), and they will build insulator regions in the active absorbing layer of the solar cell. Depending on its concentration, ZnS can minimize the active area (where the electron-hole pairs are generated) and affect current collection. Due to the low conductivity of ZnS and ZnSe, they do not influence the V_{oc} of the device, but could cause an increase in the series resistance [104]. The copper sulfide phases (CuS and Cu_2S) are expected in CZTS samples with Cu-rich composition. They have a chalcocite structure and show p-type nature with good metallic conduction, which is due to a high concentration of holes in the valence band [105]–[107]. Their presence is detrimental to the solar cell because they can shunt the device. Tin sulfide phases can evolve in Sn-rich CZTS films as SnS or SnS_2. The SnS compound is a semiconductor with application in optoelectronic and PV fields. The material exhibits both p- and n-type conduction [108] with a bandgap of 1.2–1.7 eV [109]–[112]. Tin disulfide (SnS_2) is an n-type material with direct bandgap of 2.18–2.44 eV [108], [113], [114]. Although no harmful effects were reported of Sn-S phases on solar cell performance, a high concentration of the n-type semiconductor in the p-type active layer can build a second diode that hinders carrier collection and thus reduces fill factor. Cu_2SnS_3 (CTS) is a ternary secondary phase that forms in CZTS material with Zn-poor composition. The compound is a p-type semiconductor [115] with metallic character [116], crystallizing in different crystal structures including cubic, monoclinic, and hexagonal forms [117], [118]. However, the cubic form requires temperatures higher than 775 °C to crystallize [116]; therefore, it is unlikely to be detected in kesterite films, which are prepared in lower temperatures. Depending on the crystallographic structure, the optical bandgap is in the range of 0.93−1.35 eV [119]. As $Cu_{2-x}S$ phases, CTS is harmful to the solar cell because of its high conductivity, which could decrease the shunt resistance, and its low bandgap could reduce the V_{oc}.

X-ray diffraction (XRD) is considered the primary technique for identifying elements and compounds. However, it has some limitation when distinguishing phases with similar crystal structure in a compound. This case is present in the CZTS material because ZnS, CTS, and CZTS exhibit diffraction peaks at the same positions (Figure 2.17) due to the similarity in the crystal structure and lattice parameters [120], [121]. Other secondary phases such as Cu-S and Sn-S, on the other hand, can be detected easily by XRD.

Raman spectroscopy is widely used as a complementary technique to detect secondary phases in CZTS. The kesterite CZTS exhibits two strong peaks at 288–289 cm^{-1} and 338–239 cm^{-1}, a shoulder with a main peak at 351 cm^{-1}, and a broad peak between

368–373 cm^{-1} [122]. For the cubic zinc sulfide phase, one strong peak appears at 352 cm^{-1} and a weaker one at 271 cm^{-1} [123]. Raman shifts of monoclinic Cu_2SnS_3 appear at 290 cm^{-1} and 352 cm^{-1} [117], and of the cubic Cu_2SnS_3 at 267 cm^{-1}, 303 cm^{-1}, and 356 cm^{-1} [124], [125]. The tetragonal Cu_2SnS_3 shows two peaks at 337 cm^{-1} and 352 cm^{-1}, and a large shoulder between 280 cm^{-1} and 290 cm^{-1} with peak maximum at 297 cm^{-1} [124], [125]. Table 2.2 lists the positions of Raman shifts for CZTS and the commonly developed secondary phases.

Note that most of the previous works to characterize CZTS by Raman spectroscopy were performed using blue and green wavelength excitations of 488, 514.5, and 532 nm, which are commonly used for Raman measurements. Relatively recent studies revealed additional Raman modes by employing nonstandard excitation wavelengths. Dimitrievska *et al.* [126] conducted Raman scattering measurements of CZTS using six different excitation wavelengths—from near infrared to ultraviolet—and identified 18 CZTS peaks attributed to the 27 optical modes expected for CZTS.

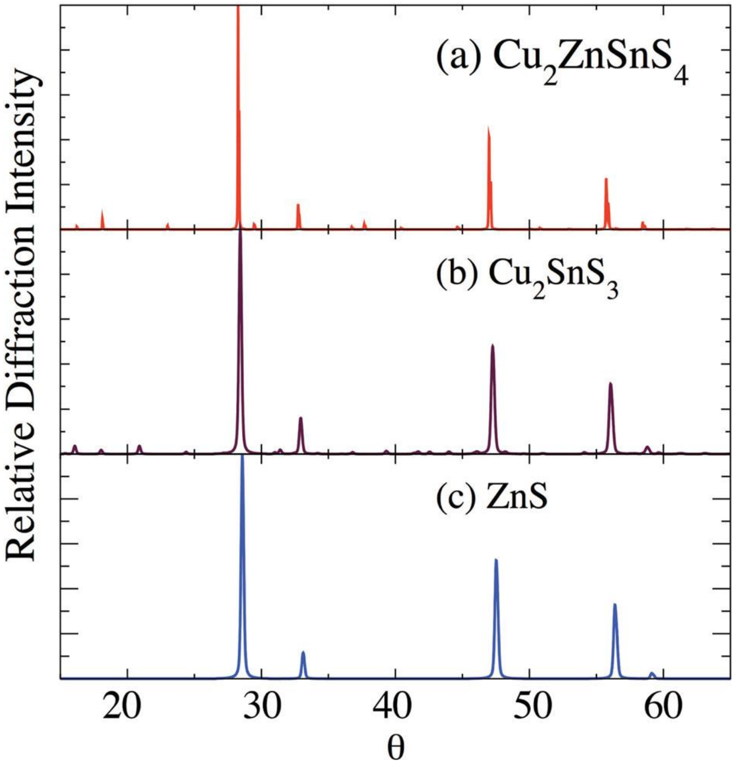

Figure 2.17: Simulated X-ray diffraction spectra of kesterite Cu_2ZnSnS_4, Cu_2SnS_3, and ZnS showing overlap of the main peaks [99].

Considering that the ZnS phase has its main Raman peak at 352 cm^{-1} and that CZTS exhibits one peak almost at the same position (351 cm^{-1}), it makes it difficult to distinguish ZnS from CZTS. The difficulty in differentiating ZnS from CZTS using Raman scattering was reported to be due to using excitation wavelengths in the visible region [127]. It has been demonstrated experimentally that the ZnS secondary phase can be successfully distinguished from CZTS by using an ultraviolet excitation wavelength of 325 nm [128]. Unfortunately, the Raman system used in our work is not equipped with the 325-nm laser source, but only with a blue and green laser; so, excluding the ZnS phase in our films was not possible using Raman spectroscopy. However, Raman measurements, unlike XRD analysis, can confirm the presence of CZTS and detect CTS phases. To identify ZnS in the synthesized films, energy-dispersive X-ray spectroscopy (EDS) was used to determine the chemical composition of small areas or even of individual grains. Detecting regions or grain with high Zn concentration implies the presence of this phase. A brief description of the work principles of the characterization technique used in this study is provided in Chapter 3.

Table 2.2: Raman shift positions of CZTS and of the common secondary phases.

Phase	Raman shifts (cm^{-1})	Reference
CZTS	287, 338, 351, 368	[76], [122]
Monoclinic Cu_2SnS_3	290, 352	[117]
Cubic Cu_2SnS_3	267, 303, 356	[124], [125]
Tetragonal Cu_2SnS_3	297, 337, 352	[124], [125]
Orthorhombic Cu_3SnS_4	318	[124], [125]
$Cu_{2-x}S$	264, 475	[121]
Cubic Zn	275, 352	[123]
SnS	163, 189, 220	[129]
SnS_2	215, 315	[129]
Sn_2S_3	52, 60, 307	[129]
Hexagonal MoS_2	287, 383, 409	[130]

2.3.4 Fabrication of Cu_2ZnSnS_4 thin films

Due to the increasing interest in synthesizing high-quality CZTS thin films for solar cell application, many methods have been developed and attempted by several research groups over the last several years to deposit kesterites. The main goals were to achieve high-quality material (homogeneous single-phase films with large grains and no voids), a low-cost fabrication process, and high deposition rate.

Kesterite CZTS(Se) can be synthesized using vacuum or non-vacuum deposition approaches in a one- or two-step fabrication process. The one-step process deposits the four constituents (Cu, Zn, Sn, and S(Se)) simultaneously on a substrate at high temperatures. High temperatures are necessary to enable the interdiffusion of the elements. In the two-step approach, a precursor containing the metals or even the four elements will first be deposited on a substrate and subsequently annealed at high temperatures in sulfur, selenium, or sulfur-selenium (for CZTSSe) atmosphere. Pure sulfide CZTS films is of preferential use compared to the selenide ones because sulfur is less toxic and less expensive than selenium, although the highest efficiencies were achieved with devices where only selenium or sulfur/selenium was incorporated in the kesterite active layer of the solar cell.

Precursors can be realized by depositing all elements at the same time (co-deposition) or as a stack of elemental layers. Growth methods and synthesis process parameters such as temperature and time were reported to influence the film properties (e.g., grain size, chemical composition, bandgap) [131]–[139].

2.3.4.1 Vacuum deposition techniques

Deposition using these techniques occurs mainly at low pressure and requires high temperatures in some methods. Generally, vacuum-based deposition techniques—including thermal evaporation, sputtering, and pulsed laser deposition (PLD)—provide good film reproducibility and easy control of film chemical composition [140].

Sputtering is one of the widely applied techniques for growing CZTS films. Because our CZTS thin films were prepared using sputtering, a brief description of the sputtering process is provided in Chapter 3. The CZTS thin-film fabrication process is usually a two-step process, where initially the precursor is deposited mostly on a glass substrate, and thereafter, is post-annealed in sulfur/selenium ambient (sulfurization/sulfurization). There are three main approaches for sputtering the precursors: sequential stacked precursors, simultaneously sputtered (co-sputtered) precursors, and precursors deposited from a quaternary target containing the four constituents. Both stacked and co-sputtered precursors can be deposited using single targets [141], [142] and/or alloy targets (binary or ternary) [143], [144]. Depositing a stacked precursor provides easier control of the film chemical composition by regulating the thickness of each element [120], whereas co-sputtering enables the deposition of a homogenous mixture of the elements and can minimize the diffusion of the metals during the annealing process. Only a few works reported on the synthesis of CZTS films deposited by sputtering from single quaternary targets [145]–[148]. This approach exhibited difficulties in controlling the film elemental composition due to the compositional deviation of the material source and the sputtered precursor [149]. Using co-sputtering to deposit the precursor followed by sulfurization step in H_2S/N_2 ambient at 525 °C, Dhakal *et al.* [150] reported fabricating a CZTS thin-film solar cell with an efficiency of 6.2%. CZTSSe-based solar cells with up 8.03% efficiency were obtained using sequential sputtering of Cu/SnS/ZnS layers followed by selenization at 570 °C [151].

Evaporation is basically based on heating a source material in a vacuum chamber so that the material evaporates and deposits on a substrate. The absorbing layer of some CIGS-based solar cells showing high conversion efficiencies were thermally evaporated [44], [152]. Using thermal evaporation, the CZTS film can be deposited in one step by evaporating all elements at high temperatures [153]–[155] or in two steps by first fabricating the precursor followed by annealing in sulfur atmosphere [156]–[158]. For pure sulfide CZTS, the highest achieved efficiency of 8.4% was with a device having an active layer prepared with thermal evaporation [15]. Cells with efficiencies of 9.2% [159] and 11.6% [160] based on CZTSe compound were also synthesized with thermal evaporation.

Pulsed laser deposition (PLD) is another physical vapor deposition (PVD) method used to prepare CZTS thin films. In this deposition technique, a pulsed laser beam with high power is used in a vacuum chamber to strike a material target, causing material evaporation from the surface of the target. The evaporated material is then deposited as a thin film on a substrate. CZTS or CZTSe/CZTSSe pellets—which were prepared by the solid-state reaction method of Cu_2S, ZnS and SnS_2 (for CZTS) or $Cu_2S(Se)$, ZnS(Se), SnS_2, Sn, S, and Se powders (for CZTSSe)—are used as a target to deposit the compound in one step [161], [162].

2.3.4.2 Non-vacuum deposition techniques

These techniques represent a cost-effective alternative to physical vapor deposition methods because they require less expensive equipment and materials. They also provide good stoichiometry control by controlling the chemical composition of the liquid precursor, and they can be used to cover a large surface. Thin-film deposition using these methods basically relies on first preparing a solution of organometallic powders dissolved in a solvent. Then, the solution is deposited on a substrate, dried, and annealed to form the required crystal phase of the compound.

Several solution-based approaches were employed to prepare CZTS and its related compounds. These include spray pyrolysis [163]–[165], electrochemical deposition [166]–[168], and spin coating [12], [169], [170]. CZTSe and CZTSSe solar cells with conversion efficiencies of over 10% were produced using solution-based depositions [171], [172]. To date, the record device based on a CZTSSe absorbing layer exhibiting an efficiency of 12.6% was fabricated using the hydrazine pure-solution approach [14]. Despite the advantages of the non-vacuum deposition methods, there are several drawbacks such as the use of highly toxic substances and the complexity of the precursor preparation in some approaches.

Chapter Three: Fabrication Approaches and Characterization Techniques

In this chapter, we present the growth method of CZTS thin films and the solar cell fabrication process used in this study. In addition, we list the different techniques employed to characterize the produced films and devices and discuss their principles of operation. All samples used in this work were fabricated and analyzed at the National Renewable Energy Laboratory (NREL) in Golden, Colorado.

3.1 Fabrication Methods

CZTS films were prepared in two steps. In the first step, a metal film containing Cu, Zn, and Sn (referred to as the metal precursor) is sputtered onto a glass substrate. The metal precursor is then annealed in sulfur atmosphere (sulfurization process) to convert the metal film into CZTS. Selected CZTS films, which were deposited on Mo layers as the back contact for the solar cell, were fabricated into complete devices by depositing the required layers on top of the CZTS layer.

3.1.1 Preparing the substrate

The main function of a substrate in thin-film technology is to provide the required mechanical support to the device or deposited layers. In general, thin films can be deposited on a wide variety of materials depending on the application and deposition method. Materials for substrates include glass, metals, ceramics, semiconductors, and polymers. The most common substrate material used to deposit CZTS has been soda-lime glass (SLG) because it provides all the necessary specifications required for fabricating

CZTS solar cells. The material with a softening temperature higher than 700 °C is inexpensive, reasonably hard, and easy to clean and cut.

In our work, SLG and molybdenum-coated (Mo-coated) SLG were used as substrates. However, depositing the Mo back contact of the device was not part of this project. Instead, Mo-coated SLG substrates with the dimension $75\times75\times2.5\ mm^3$ with Mo deposited on the airside were ordered from another group at NREL. Prior to Mo deposition, the substrates were cleaned using the following process:

1. Scrub in isopropyl alcohol (IPA) with lint-free cloth.
2. Dip for 15 minutes in Liquinox soap solution in ultrasonic bath.
3. Rinse in fresh deionized (DI) water.
4. Put in automated spin rinse/drier for 25 minutes.

The Mo layer was deposited via DC sputtering with a flow of argon (Ar) and under operating pressure of 10 mTorr. The thickness of the Mo layer is in the range of about 0.7 to1 micron.

The $7.5\times7.5\ cm^2$ Mo-coated substrates were then cut down into $2.5\times2.5\ cm^2$ to fit into the sputter-device substrate holder. The SLG substrates were used to characterize the optical properties of the CZTS thin films.

For both the Mo-coated SLG and SLG substrates, the cleaning procedure was as follows. First, the substrates were gently rubbed with a lint-free cloth in a soap solution, rinsed under flowing DI water, and then dried under nitrogen flow. Then, they were dipped in acetone bath, followed by rinsing with DI water and drying with N_2 flow. The last step was dipping them in IPA, rinsing them with DI water, and drying them with N_2

flux. The cleaned substrates were kept in a nitrogen box, ready to be loaded into the sputtering chamber.

3.1.2 Depositing the metal precursor

Sputtering is a physical vapor deposition (PVD) method widely used for the deposition of thin films. It is based on bombarding a source material with energetic ions that causes the ejection of surface atoms from the target.

The sputtering process begins by loading the substrate (onto which deposition will occur) into the coating chamber, which is then evacuated to a base pressure typically in the order of 10^{-6} torr or less to achieve a high-purity process. High vacuum inside the chamber is usually reached by using a turbo molecular pump backed by a mechanical rotary pump. Prior to sputtering, the chamber is filled with inert gas (usually argon). After reaching a prescribed gas pressure in the chamber (working pressure), a negative direct-current (DC) potential is applied to the source material (cathode) to be deposited onto the substrate, referred to as the target. The anode is represented by the substrate holder (or even the entire chamber with the substrate holder) and it is typically grounded. Under the proper conditions of gas pressure and applied voltage, the gas breaks down into a plasma discharge containing neutral gas atoms, ionized gas atoms, and electrons. A very large electrical field near the cathode accelerates the positively charged gas ions (Ar^+) toward the cathode where they strike the target surface. The incident ions with sufficiently high kinetic energy dislodge atoms from the target surface by transferring their momentum to the target surface atoms. The sputtered atoms travel to the substrate located nearby and condense on the surface to build the required layer. In addition to the sputtered atoms, there are other particles such as ions and electrons ejected from the source material. The electrons ejected from the source material are referred to as secondary electrons and they are accelerated back to the plasma discharge, where a small portion of them collide with the neutral argon atoms, causing the ejection of the outer-shell electrons of the gas atoms, and consequentially, more Ar ions are generated to sustain the plasma. The large portion of the secondary electrons passes through the plasma reaching to the anode where they strike the substrate surface and contribute to substrate heating. The principle of the DC sputtering process is illustrated schematically in Figure 3.1.

In addition to DC, the cathode can be connected to an alternating-current (AC) power supply operating at radio-frequency (RF). A frequency of 13.56 MHz is standard for most manufactured sputtering systems. Unlike DC sputtering, which is only used to deposit conductive materials (metals), an RF-powered sputtering system is used to deposit both metals and insulators. Additionally, the deposition rate in RF sputtering is higher than in DC, so that the process takes less time.

3.1.3 Magnetron sputtering

In this method, a magnet field is applied by placing magnets at the cathode plate so that a magnet field is configured parallel to the cathode. By this, the secondary electrons are confined in a region near the cathode, where they increasingly collide with Ar atoms (ionizing more atoms), and consequentially, dense plasma exists in this region. More ionization of the Ar atoms results in a higher deposition rate. In magnetron sputtering, the cathode can be powered either by DC or AC supplies. More details about sputtering can be found in the literature [173]–[175].

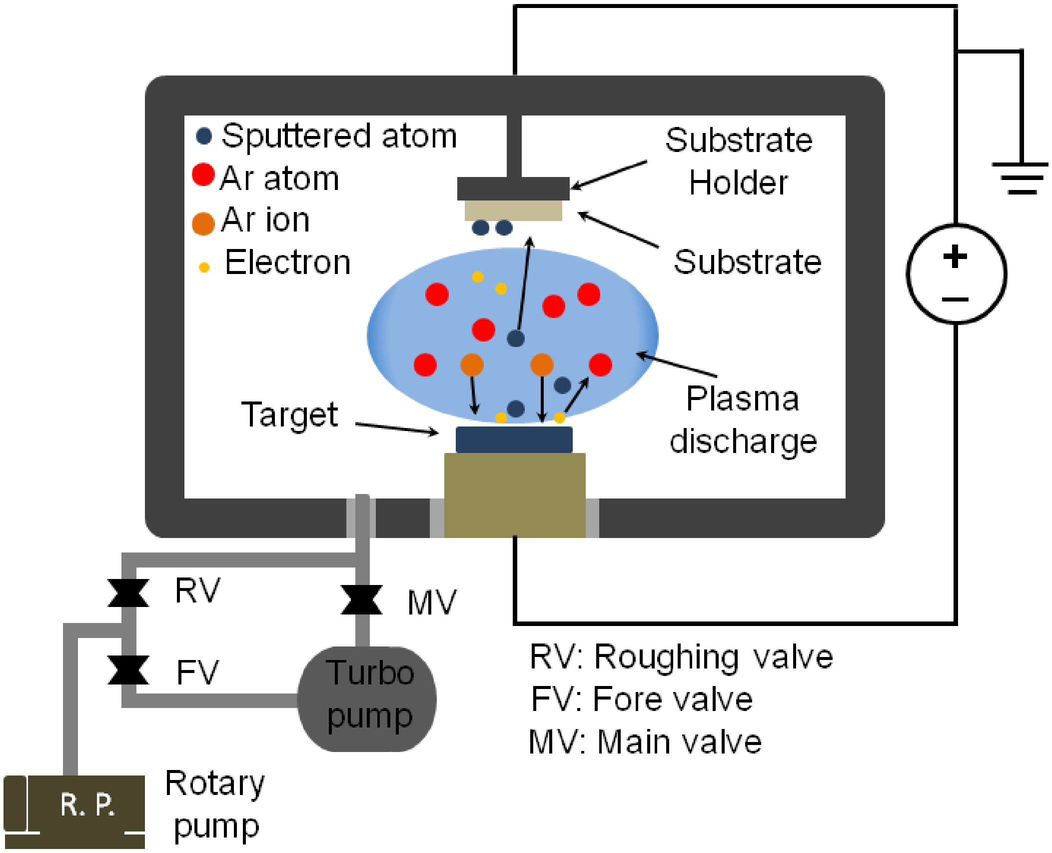

Figure 3.1: Schematic illustration of a DC sputtering system.

In this project, an RMS-200 RF&DC magnetron sputtering system from Rocky Mountain Vacuum Tech was employed to deposit the metal precursors. The system is equipped with three 4-inch cathodes having the capability of depositing three different target sources at the same time (co-sputtering). Figure 3.2 shows the sputtering system and the coating chamber containing the three target sources (Cu, Zn, and Sn). Originally, the Cu and Zn sources were powered with DC supplies that were controlled by either voltage or current. The DC power sources were replaced by RF generators because of unwanted fluctuations in sputtering power due to fluctuation in the current when the voltage was fixed or fluctuation in the voltage when the supplies were controlled by current. With fluctuating sputtering power, we had difficulties in reproducing films with the same chemical composition when using the same conditions. The parameters that can be varied to calibrate the system are:

- Substrate/target distance
- Substrate rotation speed
- Substrate temperature
- Gas flow
- Gas operating pressure
- Working power

3.1.4 Sputtering procedure

Prior to each deposition, the chamber is first pumped down to about 10^{-3} torr with a mechanical rotary pump and then evacuated to less than 10^{-6} torr using a turbo molecular pump. The Ar flow for all sputtering runs was 20 sccm and the gas pressure inside the chamber was 10 mtorr for most deposition, providing stable plasma. The process begins by applying voltage to the metal targets, which have purity of 99.9999%, whether to all targets at the same time to perform co-sputtering or to one target when depositing metal stacked layers. To obtain uniform films, the substrate rotation speed was kept at 5 rpm for all depositions. This value was recommended by the manufacturer, who carried out several experiments to optimize the film thickness uniformity. Except for a few experiments, the sputtering process was always done at room temperature. Calibration and optimization of the sputtering process will be discussed in Chapter 4.

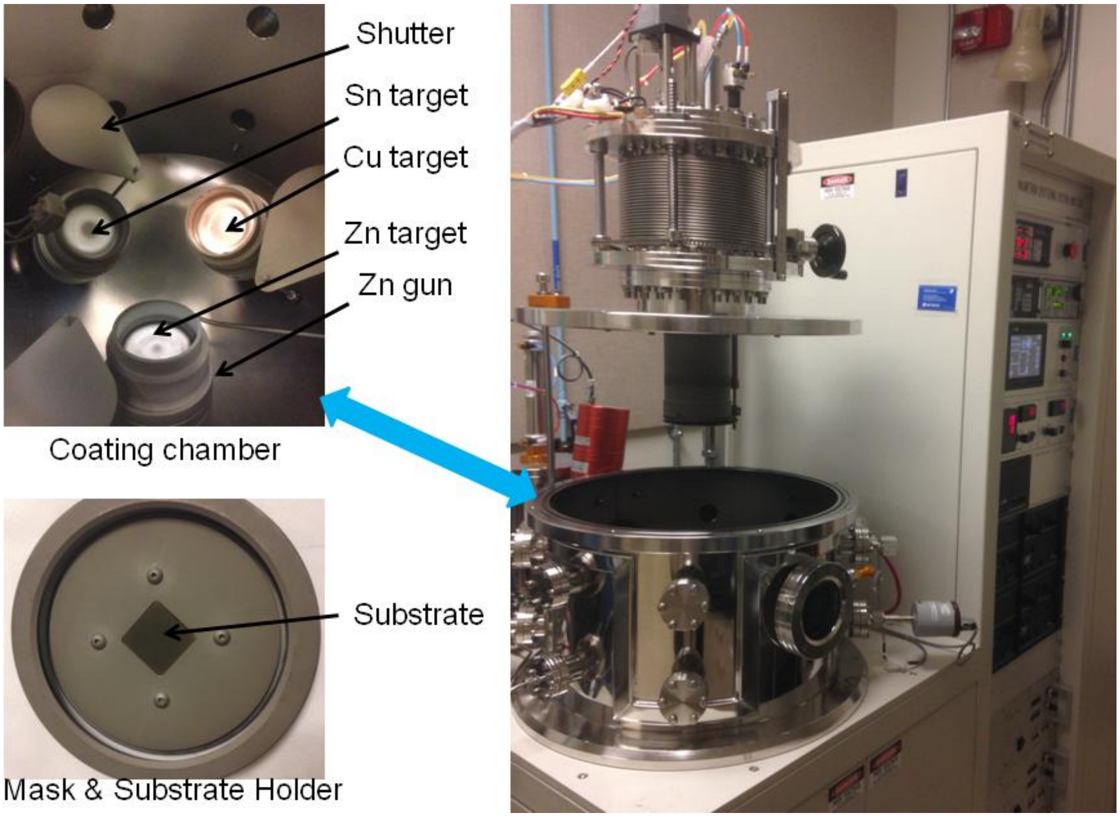

Figure 3.2: RMS-200 RF&DC magnetron sputtering system.

3.1.5 Sulfurization process

Sulfurization refers to annealing the metal precursor in sulfur ambient to incorporate sulfur and convert the precursor into CZTS film. The process occurred in a quartz-tube furnace with three heating zones. Sulfur powder was used as a source for sulfur to produce sulfur vapor inside the tube during the process. The metal precursor and sulfur powder were in alumina ceramic rectangular trays placed inside the quartz tube at the outer heating zones that were heated with different temperatures. The middle zone served as a buffering zone for adjusting the temperature difference between the outer zones. Nitrogen or argon flux was used to carry the sulfur vapor inside the tube. Three thermocouples were inserted in the tube to monitor the temperature of the sample, sulfur zone, and buffering zone. A schematic illustration of the tubular furnace is shown in Figure 3.3.

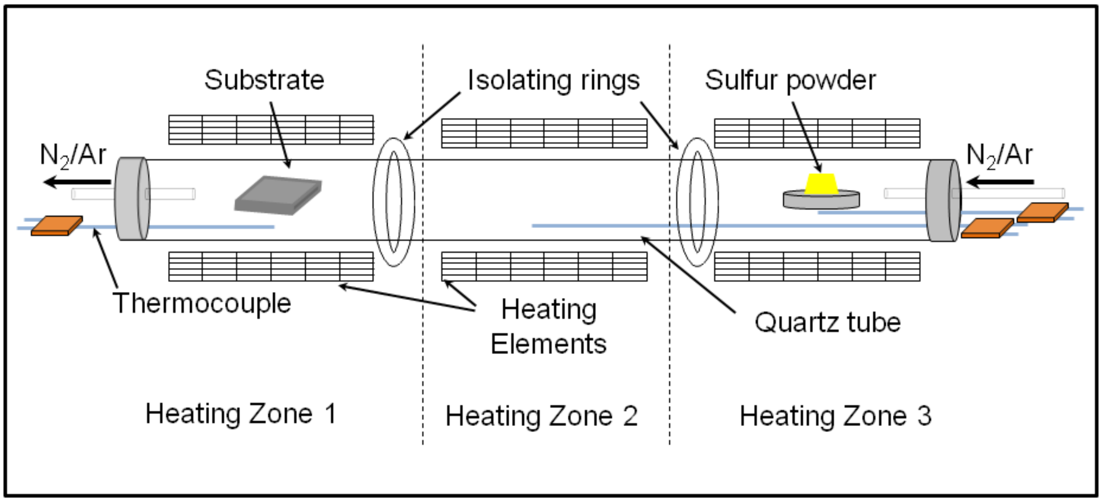

Figure 3.3: Schematic illustration of three-heating-zone quartz-tube furnace.

The parameters that can be controlled in the sulfurization process are:

- Carrying gas (Ar or N_2)
- Gas flow
- Temperature
- Ramping and dwell time for the three zones
- Sulfur vapor pressure

At the beginning of the sulfurization experiments, we faced an issue with fast evaporation of the sulfur so that about 2 grams of sulfur would evaporate within the first 10–20 minutes due to heat transfer from the substrate zones to the buffer and sulfur zone. Having sulfur vapor in the tube throughout the process is very important to ensure the supplement and incorporation of sulfur into the film during the annealing process. Table 3.1 lists the set and measured temperatures of the three zones for one of the experiments conducted to control the temperature inside the tube. Set temperature for the substrate zone was kept at 500 °C while varying the set temperatures for the buffering and sulfur zones. As the table shows, the temperature for the sulfur zone increased to 300 °C even when there is almost no heating. The temperature of this zone increased to more than 350 °C when heating the substrate zone with temperatures close to 600 °C, which resulted in even faster sulfur evaporation.

Table 3.1: Discrepancies between the set and actual temperatures of the three furnace zones caused by heat transfer.

	Substrate zone	Buffer zone	Sulfur zone
Set temperature (°C)	500	250	250
Actual temperature (°C)	505	405	330
Set temperature (°C)	500	30	30
Actual temperature (°C)	495	385	300

A second attempt to control the temperature of the heating zones and reduce the heat transfer was made by installing insolating rings made of aluminum silicate to block the heat transfer outside of the tube in the space between the quartz tube and the heating elements. This resulted in significantly reducing the heat transfer and enabled better control of the temperature inside the tube so that sulfur always remains after finishing the annealing process. Table 3.2 shows the heating profiles of the three zones after installing the insolating rings.

Table 3.2: Heating profiles of the three zones after installing the insolating rings.

	Substrate zone	Buffer zone	Sulfur zone
Set temperature (°C)	520	300	200
Actual temperature (°C)	531	313	203

After finishing the annealing process, the furnace cooled down naturally by turning down the heat and under the flow of nitrogen or argon.

3.1.6 Solar cell fabrication process

The layer sequence of the fabricated solar cells in this work is the same as the device stack showed in Figure 2.10 by replacing the CIGS layer by a CZTS layer. A standard production procedure developed at NREL for fabricating CIGS solar cells is adapted to prepare CZTS devices.

After preparing the active CZTS layer on a Mo back-contact layer, a cadmium sulfide (CdS) layer about 50 nm thick is grown via chemical bath deposition (CBD) to create the p-n-junction. Then, the transparent conductive oxide layers were sputtered by first depositing a 50-nm i-ZnO layer and then an n-ZnO layer about 200 nm thick. A Ni/Al grid as the front contact was then deposited using thermal evaporation. For the cells fabricated in this project, no MgF_2 antireflection coating was applied. Detailed descriptions of the deposition of the different layers can be found in [176]–[179]. Four cells of 0.42-cm^2 area were fabricated on each 2.5×2.5 cm^2 substrate. A photo of four CZTS devices fabricated on 2.5×2.5 cm^2 glass substrates is shown in Figure 3.4.

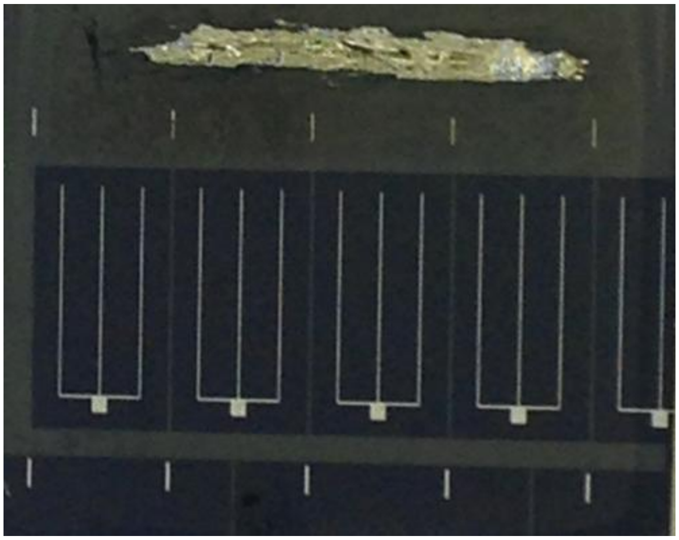

Figure 3.4: Fabricated solar cells on 2.5×2.5 cm^2 glass substrate. Each device has an area of 0.42 cm^2.

3.2 Characterization Techniques

3.2.1 Thin-film thickness measurements

Thin-film thickness is one of the crucial parameters impacting the physical properties of thin films [180]; therefore, it is of great importance to measure and control the thickness of thin films. The appropriate technique for measuring, estimating, or monitoring the thickness can be chosen depending on the application and the properties of the thin film. Some thin-film applications require the control and monitoring of the thickness during the deposition (*in-situ*), whereas in other applications the thickness is determined after the film growth (*ex-situ*). To monitor the thickness and the deposition rate during film growth, most high-vacuum deposition systems use a quartz-crystal microbalance. In some deposition systems, optical measurements systems are used to monitor the thickness. The sputtering system used in our work to grow the metal films is equipped with a quartz-crystal sensor allowing us to monitor the thickness and deposition rate. However, *ex-situ* measurements were necessary to determine the final CZTS thin-film thickness after sulfurizing the metal films. Regarding the thickness measurement after the film deposition, a wide range of techniques are employed in the industry to measure thin-film thickness, including stylus and optical profilometry [181]–[183], interferometry [184], [185], cross-sectional scanning electron microscopy (SEM) and cross-sectional transmission electron microscopy (TEM) [186], ellipsometry [187], and spectrophotometry [188].

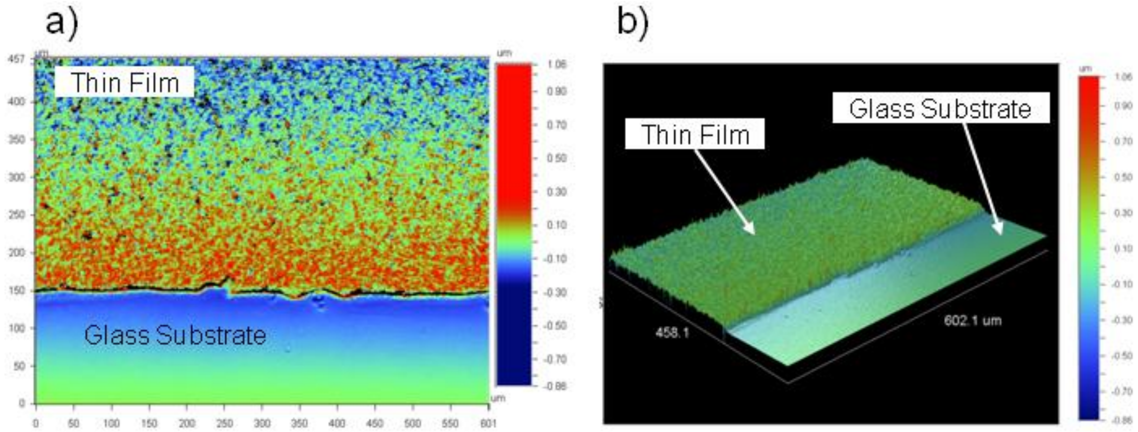

Figure 3.5: Measurement data of a Zn film that was sputtered at 50W for 60 minutes. The measurement shows: (a) Surface of the film and glass substrate. (b) 3-D image exhibiting the step between the film and the glass substrate.

In our project, we primarily used SEM and stylus profilometry to measure film thickness. In addition, some samples were characterized with an optical interferometer that provides a three-dimensional surface profile with no sample contact. Using this method, we can measure not only the surface roughness, but also, the film thickness can be precisely measured when a step is present between the substrate and the film. The optical interferometer works in phase-shifting interferometry (PSI) mode and in vertical-scanning interferometry (VSI) mode. The PSI mode allows measurements of smooth surfaces, whereas VSI allows measurements of rough surfaces. Despite the advantages of the optical profiler, it was not used throughout this work for two reasons: 1) for some samples, we had a problem obtaining clear interference fringes because the surfaces of the samples were not reflective enough; and 2) the measurement instrument was not available most of the time. Figure 3.5 illustrates top surface area and 3-D image of a Zn thin-film sputtered at 50 W for 60 minutes. The measurement was performed at the step between the film and the glass substrate to measure the thickness.

3.2.1.1 Stylus profilometer

In principle, this mechanical technique can also monitor both thickness and roughness of a thin film using a diamond-tipped stylus that scans the film surface. The stylus first moves vertically to contact the surface of the sample and then the stage moves the sample beneath the stylus so that it scans the surface with a pre-set speed and scan length. The surface roughness causes the stylus to move in the vertical direction. Electrical analog signals corresponding to the horizontal and vertical movements of the stylus are produced and converted into digital signals that can be stored or used to interpret the surface features. To measure the thickness, the stylus, similar to the optical profilomter, must move over a step between the substrate and the film surface. Such steps were obtained in our samples using a mask covering the outer edge of the substrate during the deposition of the metal films. Figure 3.6 shows schematically the operation of a stylus profilometer.

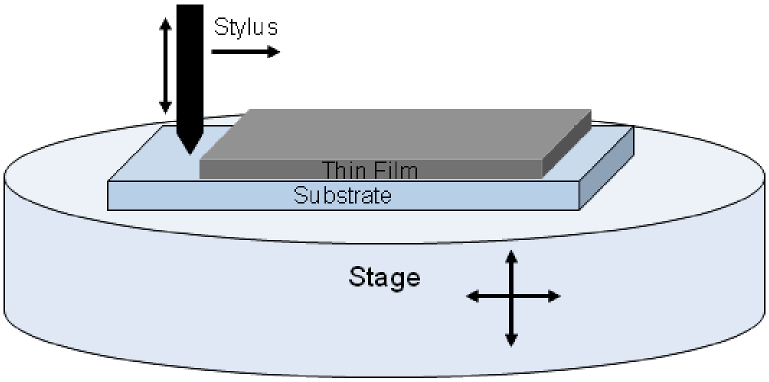

Figure 3.6: Schematic illustration of the stylus profilometer operation.

A Veeco DekTak 8 stylus profilometer was used in our work to perform the thickness measurements. Some of the instrument’s specifications are listed in Table 3.3.

Table 3.3: Some specifications of the Veeco DekTak 8 stylus profilometer.

Scan Length Range	50 mm standard; 100 mm optional
Data Points per Scan	60,000 maximum
Sample Thickness	25.4 mm maximum
Wafer Size	200 mm
Step Height Repeatability	7.5 Å, 1 sigma on 1-µm step
Vertical Range	262 µm standard; 1 mm optional
Vertical Resolution	1 Å maximum (at 6.55-µm range)
X/Y Repeatability	±5 µm

Figure 3.7 shows a line-scan profile of a sputtered metal film with stack order of glass, molybdenum, zinc, tin, and copper.

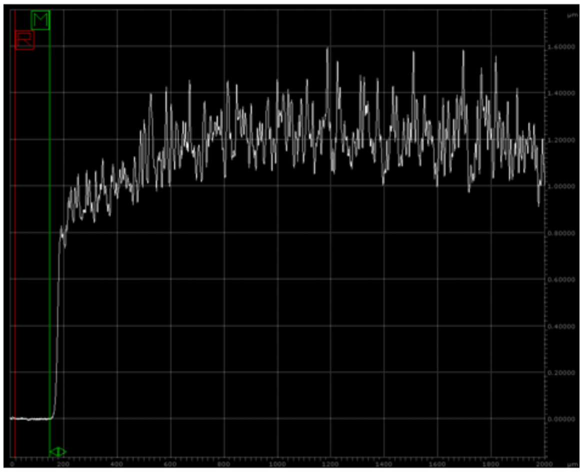

Figure 3.7: Stylus profilometer line-scan profile over a stacked metal film.

3.2.1.2 Cross-sectional SEM

In addition to analyzing the surface morphology of a thin film, SEM can be used to measure the thickness of the film. Compared to the profilometer techniques, this method does not require a step between the film and substrate. However, a clean cross-section of the film must be prepared and mounted perpendicular to the electron beam. Using the rule included in the software or the measuring bar on the micrograph, we can measure the film thickness. The precision of the measurement depends of the resolution of the instrument and what magnification was used.

Figure 3.8 shows a cross-sectional SEM micrograph of a CZTS film. As the micrograph shows, the thickness can be easily determined.

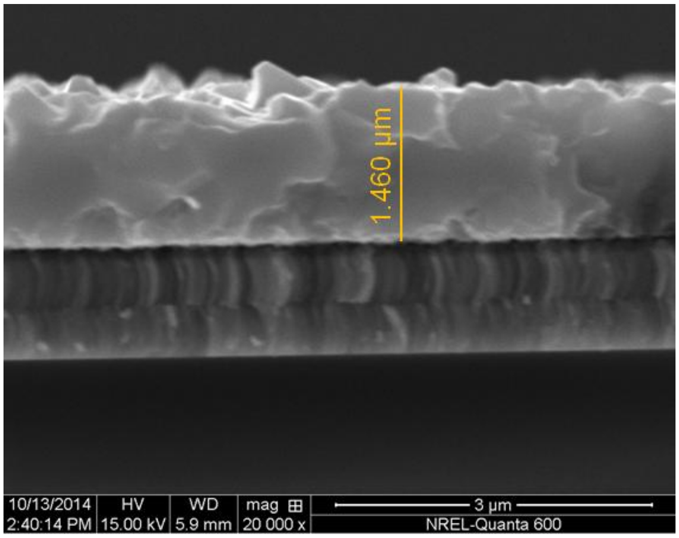

Figure 3.8: Cross-sectional SEM image of a CZTS film showing the measured thickness.

3.2.2 X-ray diffraction (XRD)

X-ray diffraction is a non-destructive technique that is widely used to analyze crystal structure of materials. It relies on the diffraction of an incident X-ray beam by the crystalline atoms, which are arranged in regular patterns (periodically repeated in a 3-D lattice). For the diffraction to occur, the wavelength of the incoming light needs to be on the same order as the crystal lattice constant. Therefore, we use X-rays, with their wavelengths on the order of few angstroms, similar to the inter-atomic spacing in crystals.

When a monochromatic X-ray beam with varying incident angle is directed at a crystalline material, it will be scattered by the regularly arranged atoms. Depending on the kind of scattering (inelastic or elastic), the scattered X-rays can destructively or constructively interfere. In constructive interference, elastically scattered rays form diffracted beams in some directions, with the intensity of its maxima (peaks) at certain angles when the path difference of two reflected waves from two parallel planes is an integral of the wavelength. This condition is described by Bragg's law and given by the relation:

$$n\lambda = 2d\ sin\theta \qquad (3.1)$$

Here, n is an integer number and is referred to as the order of diffraction, λ is the wavelength of the X-ray beam, d is the spacing between consecutive parallel planes, and θ is the incident angle. As Equation 3.1 shows, we can calculate the lattice spacing by knowing the X-ray's wavelength and the incident angle. Figure 3.9 illustrates the diffraction of X-rays by a crystal.

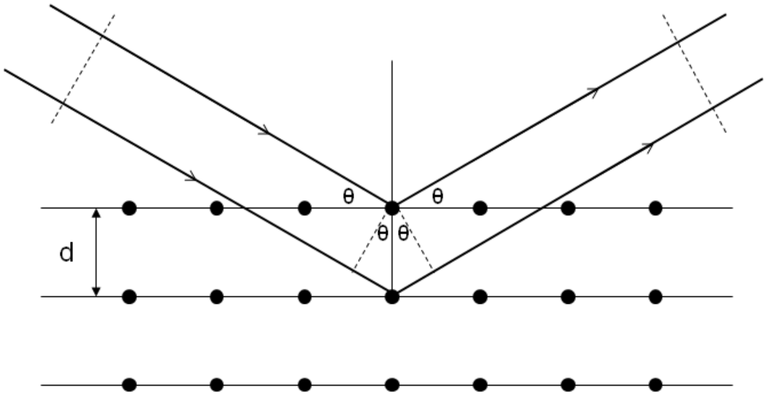

Figure 3.9: Illustration of the interaction between X-rays and crystallographic planes.

A diffractometer basically consists of an X-ray source, sample stage, and detector to measure the reflected rays. The intensities of the diffracted beam at different angles is measured by the detector and is represented in a diffraction pattern as a function of 2θ, whereas 2θ, the diffraction angle, is the angle between the transmitted beam and the diffracted beam. This scan mode is used throughout this work and is known as θ-2θ scan.

The main goal of using XRD in our work was to identify the crystalline phases in our samples. Determining the phases is obtained by comparing the experimentally measured data with standard data published by the International Center for Diffraction Data (ICDD), previously known as the Joint Committee on Powder Diffraction Standards (JCPDS), and matching the relative intensities and positions of the peaks in the diffractogram to those in the database. Jade 9 is the data analysis program used to identify the crystalline phases. The collected XRD data in databases are obtained from single-crystalline samples in powdery form so that the fine crystallites can be assumed to be randomly oriented.

If the ratios of the measured peak intensities differ from the ratios of the ones listed in databases, then the sample has preferential orientation or texture. This phenomenon is observed in multicrystalline thin films. For instance, sputtered CZTS has been reported to have preferential orientation in the 112 plane [146][189], [190].

Other structural characteristic features that can be determined by XRD are the internal strain, size of crystallites, and the quality of thin-film materials. Thin films with good crystallinity exhibit sharp and intense diffraction peaks, whereas broadened and weak peaks are obtained when the material has defects such as dislocations or impurities. Internal strain can be detected when there is a shift in the position of the diffraction peaks. The peaks shift can be toward lower 2θ (tensile stress) or toward higher 2θ (compressive stress). Occurrence of the two types of strain results in broadening the peaks. The average of the crystallite size in the material is related to peak broadening and can be estimated using Scherrer's equation [191] given as:

$$t = k\lambda / B\cos\theta \qquad (3.2)$$

where λ is the wavelength of the X-ray source in nanometers, B is the full peak width of the diffraction peak at half maximum height (FWHM) in radians, θ is the incident angle satisfying Bragg's law, and k is a constant that, depending on the shapes of the crystallites in the samples, takes values close to unity (normally 0.9) [192], [193]. For the estimation of the grain size of our films, we used scanning electron microscopy (SEM) and electron backscattered diffraction (EBSD).

The diffractometer used in this project is a Rigaku Ultima IV with Cu Kα (λ = 1.54 Å) radiation working at 40 kV and 40 mA.

3.2.3 Raman spectroscopy

Raman spectroscopy uses the Raman effect to characterize the chemical composition and structure of materials. As mentioned in Section 2.3.3, Raman spectroscopy is used in this work as a complementary technique for XRD to identify secondary phases in the CZTS compound.

3.2.3.1 Principle of Raman spectroscopy

When a material is illuminated, the incident light can be scattered, absorbed, or pass through the material. Initially, a molecule is most probably in the ground electronic state. If the photon energy matches the energy gap between the ground state and an excited state of the molecule, the photon can be absorbed, transferring its energy to the molecule, and the molecule moves to an electronic excited state. If, on the other hand, the energy of the incident photon is less than the bandgap of the material, the photon will interact with the molecule and scatter from it. In this case, when a monochromatic light with frequency υ_0 (usually a laser) illuminates a sample, the largest part of the scattered light experiences no change in its frequency (no change in the photon wavelength λ_0 or energy hv_0). This kind of scattering is referred to as elastic or Rayleigh scattering. However, a small portion of the scattered photons experiences a frequency shift (gain or loss of energy). This type of scattering is called inelastic or Raman scattering. Comparing both scattering processes, about one photon from every 10^6–10^8 scattered photons would be Raman scattered [194]–[196]. The frequency shift of the scattered photons results from exciting the vibrational state of the material molecules by the incident photons so that energy transfer occurs between the molecules and photons. Depending on the direction of energy transfer (from the molecule to the photons or from the photons to the molecule), we differentiate between two types of Raman scattering—namely, Stokes and anti-Stokes scattering. Figure 3.10 illustrates the energy-level diagram of the three types of scattering.

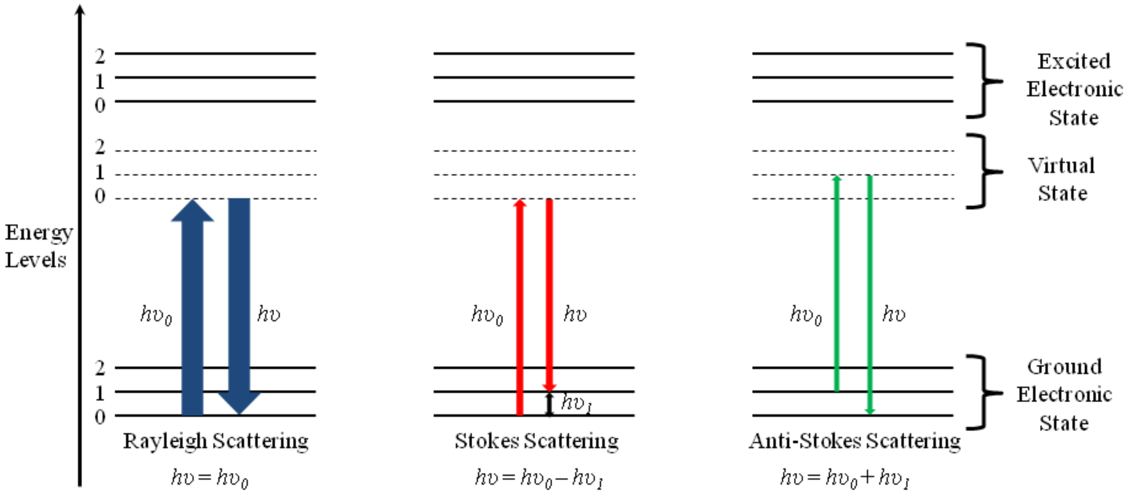

Figure 3.10: Illustration of the energy-level diagram for Rayleigh scattering, Stokes Raman scattering, and anti-Stokes Raman scattering.

Absorbing the incident photon, the molecule will be excited from the vibrational ground state to a virtual vibrational state for a very short time, and then it falls back to the ground state, emitting a photon.

- If the molecule returns back to the same state it starts from, no energy transfer will occur, and consequently, the emitted photon scatters with the same frequency as of the incident photon (Rayleigh scattering).

- If the molecule falls back to a vibrational mode higher than the state it starts from, energy transfer occurs from the photon to the vibrational mode of the molecule, and consequently, the emitted photon scatters with downshifted frequency (Stokes Raman scattering).

- If the molecule starts from an excited vibrational state and falls back to a lower energy state, energy transfer occurs from the molecule to the photon, so that its frequency is upshifted (anti-Stokes Raman scattering).

Because the frequency shift of the Raman scattered light is related to the transitions between the vibrational modes in the scattering molecule, the energy spectrum of the Raman scattered radiation (Raman spectrum) can be used to identify the material. The Raman spectrum illustrates the intensity of the Raman photons as a function of the frequency shifts (Raman shifts, lines, or bands). The Raman shift Δ_v is represented as wavenumbers with the unit cm^{-1} and can be mathematically expressed as:

$$\Delta_v(cm^{-1}) = (1/\lambda_0 \pm 1/\lambda_1)10^7 \qquad (3.3)$$

where λ_0 is the wavelength of the incident laser, and λ_1 is the wavelength of the Raman scattered light measured in nm.

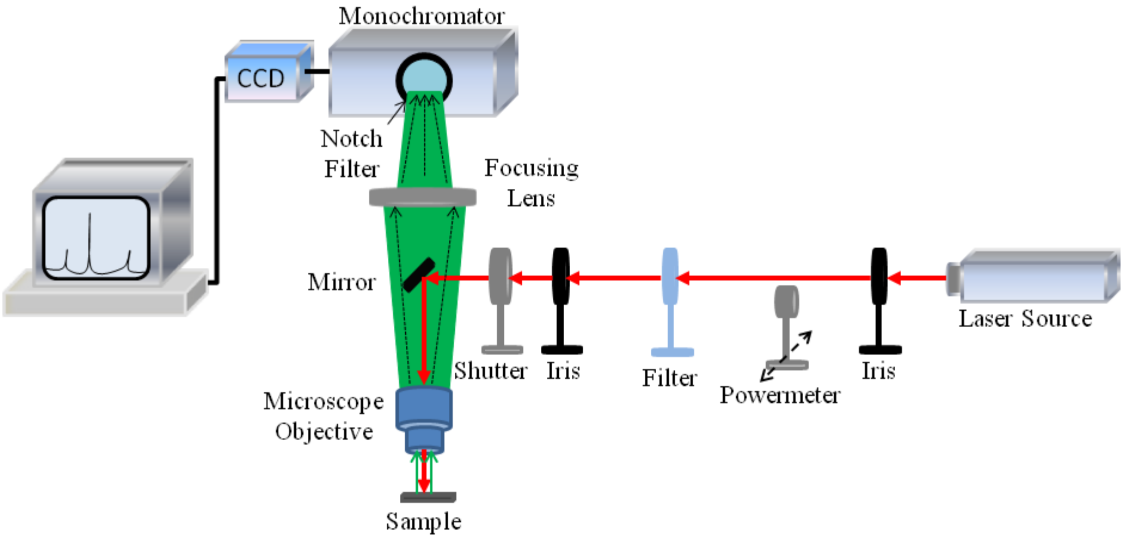

Figure 3.11: Schematic illustration of the Raman system.

Figure 3.11 shows a schematic illustration of the Raman system used in our work. The system is equipped with three laser sources—namely, an argon ion (Ar^+) laser (λ = 488 nm), Nd:YAG laser (λ = 532 nm), and HeNe laser (λ = 633 nm).

3.2.4 Scanning electron microscopy (SEM)

SEM is a widely employed microscopy technique for imaging and analyzing microstructure morphology of thin films. An electron microscope uses electrons instead of light to provide micrographs with higher resolution. The obtained high resolution is due to the much smaller wavelengths of electrons compared to those of visible light.

The principle of operation of a scanning electron microscope is based on bombarding the sample with a focused beam of electrons that originate from an electron source (electron gun), and then collecting the signals that result from the interaction between the specimen and electrons. The core components of a scanning electron microscope are the control console and the electron column, which mainly contains an electron gun (located on top of the column), electromagnetic lenses, scanning coils, and signal detectors. The microscope column and its components are under vacuum to prevent electrons from scattering before reaching the specimen. After generating and accelerating the electrons in the electron gun, they travel down the column as a beam that will be focused to a small spot size by a system of magnetic lenses. The scanning coils enable the beam to scan over an array of discrete locations on the specimen. The secondary and/or backscattered electrons emitted from the sample surface as a result of the interaction of the incident electrons and the specimen are then detected and converted to signals that are used to create the image. Detailed discussion of SEM and how it works can be found in [197].

An FEI Quanta 600 scanning electron microscope was used in our work to investigate the morphology of the fabricated metal and CZTS films, and to determine the film thickness.

3.2.5 X-ray fluorescence (XRF)

X-ray fluorescence (XRF) spectrometry is a fast and non-destructive analysis technique that is widely used to determine the chemical composition of solids, liquids, powders, and thin-film samples. XRF also delivers accurate and reproducible data. Furthermore, it is an easy-to-use method and the samples to be analyzed require minimal or no preparation for the measurement. XRF measurement, on the other hand, has some limitations. Generally, the elements that can be detected by XRF range from sodium (Na) to uranium (U) when using energy-dispersive (ED) spectrometers. When wavelength-dispersive (WD) spectrometers are used, the range can be extended down to beryllium (Be) [198].

A Fischerscope X-ray XDV-SDD, which is an energy-dispersive X-ray fluorescence spectrometer, was used in this work to determine the chemical concentration of our thin films. The device can detect the three metals Cu, Zn, and Sn, but not sulfur. Sulfur has three main lines: a doublet at about 2.3 keV and a singlet at 2.5 keV. These are relatively low in energy compared to larger atomic-number elements. The problem with low-energy X-rays is that they are easily absorbed by the detector window (beryllium foil) and the air (if present). For the duration of this project, all the XRF devices used measured samples in air and there were insufficient X-rays from sulfur to be detected.

Hence, the XRF system was only used to determine the metal concentration in both the metal precursors and the sulfurized CZTS films.

3.2.5.1 Principles of X-ray fluorescence

When a material is irradiated with X-ray photons having energy greater than the atomic binding energy, photons will be absorbed, causing the ionization of the material atoms by ejecting electrons from inner-shell orbitals (photoelectric effect). The vacancy in the atom's inner-shell orbital that an ejected electron left behind will then be filled by an outer-shell electron to stabilize the atom, and the transition from a higher to a lower energy level results in emission of secondary X-ray photons (fluorescence) from the sample. Figure 3.12 shows a schematic illustration of the XRF process. The illustration is based on Bohr's model of atomic structure, but the process can also be illustrated by the Jablonski diagram.

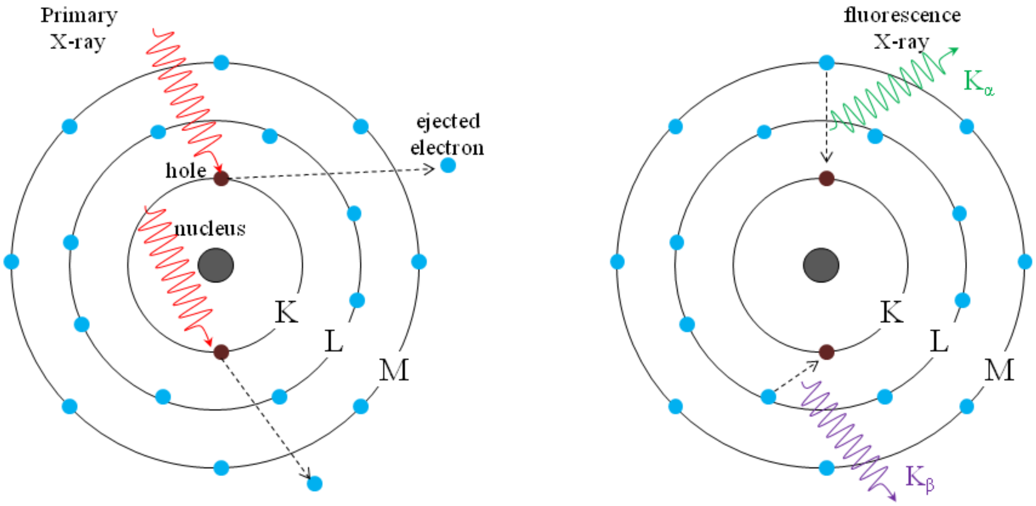

Figure 3.12: Schematic illustration of the principle of X-ray fluorescence.

The energy of the emitted fluorescence photons, which is less than the energy of the primary X-ray photons, is equal to the difference between the binding energies of the two orbitals involved in this transition. Because the atoms of each element have unique energy levels, the emitted fluorescence radiation is characteristic of the elements present in the sample and appears as lines in the measured fluorescence spectrum (energy vs. intensity). XRF delivers qualitative and quantitative analysis. In the qualitative analysis, we can identify the elements present in the sample from the energy position of the peak. The chemical composition of the sample can be calculated from the peak intensity of the characteristic fluorescence X-rays because the peaks' intensities are proportional to the concentration of the various elements in the sample. More details about X-ray fluorescence can be found in [199].

3.2.6 Energy-dispersive X-ray spectroscopy (EDS/EDX)

EDS is a measurement technique used to identify the chemical composition of compounds. Similar to XRF, EDS relies on the detection of characteristic X-ray photons produced by the elements present in a sample after bombarding the specimen with a high-energy electron beam in an electron microscope. The main difference between XRF and EDS is that EDS uses electrons instead of X-rays to excite the atoms in the sample. Another difference between the two methods is that XRF spectrometers are stand-alone analysis systems whereas EDS devices are typically coupled to SEM systems. They can be also attached to transmission electron microscopes (TEM). As in energy-dispersive XRF (EDXRF), semiconductor detectors are used to simultaneously detect the multichromatic spectrum of the X-ray photons emitted from the sample. The detector converts the X-ray photon energy into voltage pulses, and the amplitudes of these pulses correspond to the concentration of the elements present in the sample. Figure 3.13 shows an EDS spectrum of a CZTS sample, where the abscissa represents the X-ray energy in eV and the ordinate axis represents the number of counts.

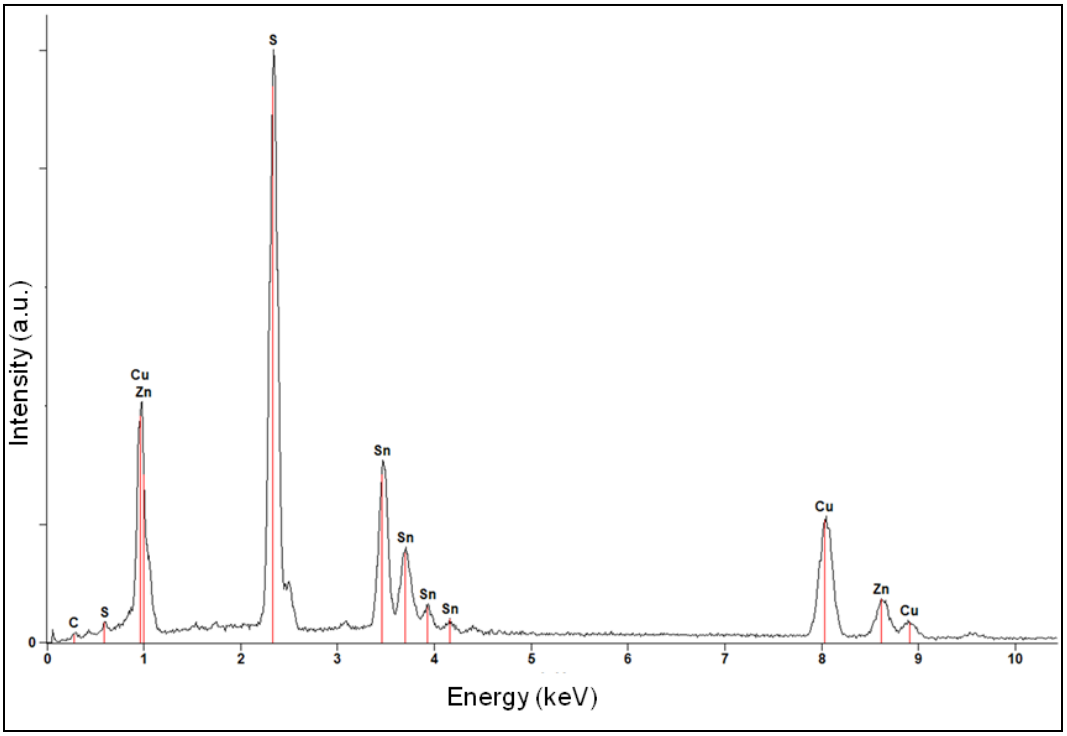

Figure 3.13: An energy-dispersive X-ray spectrum of a CZTS sample.

Unlike the EDXRF spectrometer used in this work to determine the metal concentration, the SEM/EDS system is able to detect sulfur in the CZTS films because the measurement occurs in vacuum. Here, note that the EDS measurements are not calibrated with homogeneous standard CZTS samples, which consequently could affect the accuracy of the measured quantitative data. However, the X-ray spectral analysis software can be set up to perform quantitative analysis without using standards. The analysis software identifies (either automatically or manually) the elements present in a sample and uses them for the quantitative analysis to determine their weight and atomic percentage. The software also allows the user to exclude any of the identified elements from the quantitative analysis. The excluded elements could be some sort of contamination, elements not belonging to the sample, or elements in whose concentration we are not interested. A Noran System Six is used for the acquisition and analysis of the X-ray spectrum. It consists of X-ray microanalysis acquisition electronics connected to the EDS X-ray detector and of software installed on a computer for the Xx-ray microanalysis.

Thus, EDS is mainly used in this work to quantitatively determine the concentration of sulfur in the final CZTS films. It was also used as a complementary method to XRD and Raman measurements to identify secondary phases in the CZTS compound because it can be used to determine the composition of a very small area or even of an individual grain. Additionally, the analysis software provides EDS elemental mapping that can be used to show the elemental distribution in the sample and to reveal if there are any compositional gradients.

3.2.7 Electron backscatter diffraction (EBSD)

EBSD is technique used to study crystal microstructure including texture, type of grain boundary, grain size, and crystal orientation. Typically, an EBSD system (detector) is attached to an SEM device and basically consists of a digital camera and phosphor screen (Figure 3.14).

As mentioned in Section 3.2.4, a portion of the accelerated electron beam impinging on the crystal specimen will be backscattered in all directions. The elastically backscattered electrons meeting Bragg’s condition for diffraction will form diffracted patterns (Kikuchi patterns) on the phosphor screen, where they can be captured by the camera. Analysis of the electron backscattered patterns (EPSPs) is performed using specialized computer software.

The specimen is tilted to about 70˚ so that the incident beam builds an angle of 20˚ with the sample. Tilting the sample, which enables the detection of more diffracted electrons, is required to visualize the diffraction patterns. The other requirement for the pattern to be viewed relates to preparing the sample surface. Because the backscattered electrons forming the diffracted patterns originate from a near-surface region with a depth of a few tens of nanometers, this region must be clean, strain-free, and have minimal surface roughness. To prepare our samples for EBSD, some CZTS samples were ion-milled using a cross-sectional polisher (JEOL, 1B-09010CP).

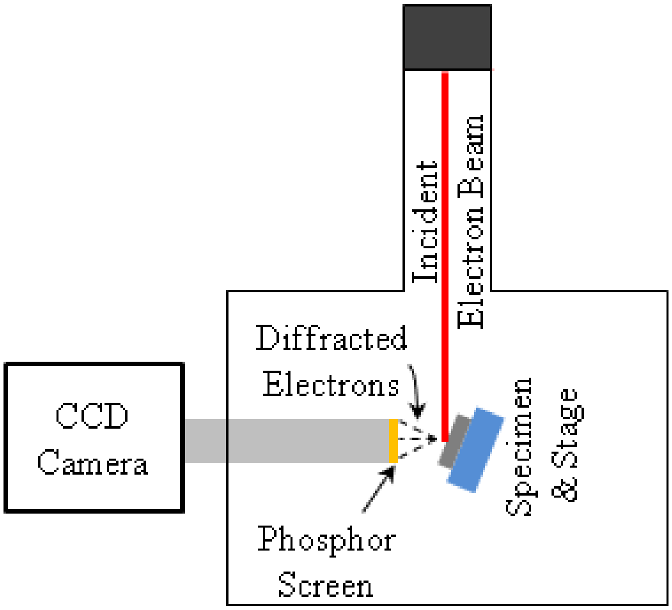

Figure 3.14: Schematic illustration of the sample setup inside the SEM chamber.

3.2.8 Atomic force microscopy (AFM)

Atomic force microscopy or scanning force microscopy (SFM) is a type of scanning probe microscopy (SPM) in which a sharp tip is used to scan across the surface of a sample and encounters features of different heights. It provides a high-resolution 3-D topographic profile of the surface. The scanning sharp tip is attached to a free end of a cantilever, and, depending on the imaging mode used, the tip either does or does not contact the surface of the sample. The changes in the cantilever deflection while scanning the sample surface are measured by a photodiode detector that monitors a laser beam reflected on the cantilever. A computer is used to store the vertical movement of the cantilever at each (x,y) point on the scanned area, and the stored data are used to produce the topographic image of the sample surface. Figure 3.15 shows a schematic of an atomic force microscope, illustrating the basic components.

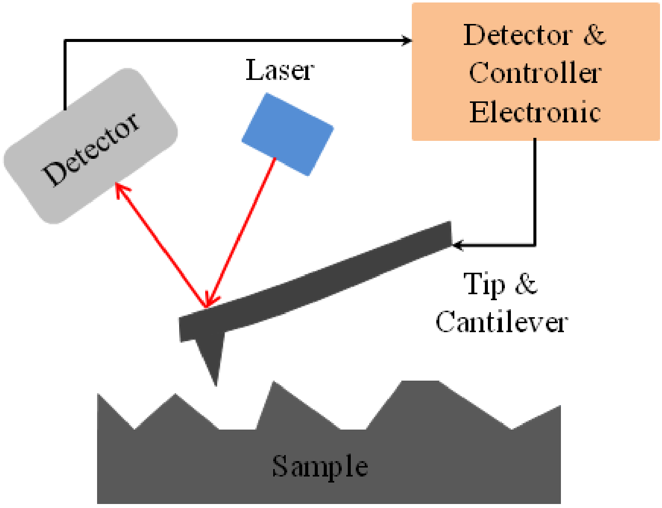

Figure 3.15: Schematic illustration of an atomic force microscope.

AFM was used in this work to evaluate the surface roughness (Z) of some fabricated CZTS films. The most commonly used parameters to judge surface roughness are the roughness average R_a and the root mean square (RMS) average. R_a is the arithmetic average of the absolute deviation from the center plane, whereas R_q is defined as the standard deviation of the roughness values from the center plane, and it can be calculated using the following formulas:

$$R_a = \frac{1}{N}\sum_{i=1}^{N}\left|Z_i - Z_{cp}\right| \qquad (3.4)$$

$$R_q = \sqrt{\frac{\sum_{i=1}^{N}(Z_i - Z_{ave})^2}{N}} \qquad (3.5)$$

where N is the number of the points in the scanned area, Z_i is the current Z value, Z_{cp} represents the Z value of the center plane, and Z_{ave} is the average Z value of the given area.

3.2.9 Ultraviolet–visible–near-infrared spectroscopy (UV-Vis-NIR)

UV/Vis/NIR spectroscopy is a measurement technique to characterize the optical properties of material by measuring reflectance, transmittance, and absorbance, covering a wavelength range from 200 to 2500 nm. An Agilent Technologies Cary 5000 UV/Vis/NIR spectrometer with 150-mm integrating sphere was used to directly measure the reflectance and transmittance spectra of CZTS thin films deposited on SLG substrates.

The optical absorption coefficient α(λ) of the films can be calculated from the measured reflectance (R(λ)) and transmittance (T(λ)) spectrum using the following relation [200]:

$$\alpha(\lambda) = \frac{1}{t} ln\left[\frac{\left(1-R(\lambda)\right)^2}{T(\lambda)}\right] \qquad (3.6)$$

where t is the thickness of the thin film. The absorption coefficient is related to the optical bandgap energy of the semiconductor, and it is given by the following equation [200]:

$$\alpha(\lambda) = \frac{A(hv - E_g)^n}{hv} \qquad (3.7)$$

where A is a constant, h is the Planck's constant, v is the frequency of the incident photons, and n defines the nature of the optical transition and can take values of 1/2, 3/2, or 2 for direct-allowed, direct-forbidden, and indirect-allowed transitions, respectively. The optical bandgap energy is obtained by considering a direct-allowed transition for CZTS ($n = 1/2$) [124], [201] and reading the intercept of the extended linear part of the $(\alpha hv)^2$ vs. hv plot with the abscissa.

3.2.10 Current-voltage (I-V) measurement

Current-voltage measurements were conducted to obtain the electrical characteristics of the fabricated CZTS solar cells. The sample containing four devices, each of which has an area of 0.42 cm^2, is mounted on a temperature-controlled stage (~25 ˚C) and the front and back contacts are then connected to a Keithley Model 2400 source meter instrument to measure the cell characteristics. The Mo back contact was exposed by scribing the device top layers.

To perform light I-V-measurements, the devices are illuminated under standard test conditions (global air mass (AM1.5) radiation, intensity of 1000 W/m^2). The devices are biased by applying a voltage of a span from -0.2 to 0.6 V, and simultaneously, the current through the cell is measured. The output is the light I-V curve from which we obtain the cell parameters (I_{sc}, V_{oc}, P_{max}, FF, and η). Additionally, the solar cell can be reverse biased without illumination to have more insight about the electrical characters. From the dark I-V curve of the solar cell, we can determine parameters such as series resistance (r_s), shunt resistance (r_{sh}), saturation currents (I_0), and ideality factor (n).

To compare the performance of solar cells produced by different research centers and groups, the short-circuit current density ($J_{sc} = I_{sc}/A$ in mA/cm^2) instead of the short-circuit current (I_{sc}) is commonly used to eliminate the dependence of the device area.

3.2.11 Quantum efficiency (QE) measurement

Quantum efficiency measures the efficiency of a solar cell in converting the incident light photons into carrier charges that can be collected from the cell. In principle, the solar cell is illuminated with monochromatic light and the current is monitored. By varying the wavelength of the incident light, we obtain a curve of the current as a function of the wavelength. Two types of quantum efficiency can be differentiated: external quantum efficiency (EQE), also known as incident photon to current efficiency (IPCE), is defined as the ratio of the number of carrier charges extracted from the cell to the number of photons incident on the cell, and internal quantum efficiency (IQE), also known as absorbed photon to current efficiency (APCE), which relates the number of carrier charges extracted from the cell to the number of photons absorbed by the cell. Both efficiencies can be expressed as a function of wavelength or energy. They are related by the following equation:

$$EQE(\lambda) = \big(1 - R(\lambda)\big)IQE(\lambda) \qquad (3.8)$$

where $R(\lambda)$ is the reflection coefficient from the device top surface.

In the literature, the external QE is sometimes referred to as the quantum efficiency because it provides information about the device’s overall efficiency considering both optical and electrical losses. The EQE spectrum can be used to determine the bandgap of the film.

The QE measurements in this work were performed using a Newport Oriel IQE 200 capable of measuring EQE and IQE at the same time. The wavelength of the incident light ranges from 300 to 1200 nm.

Chapter Four: Results and Discussion

4.1 Deposition of Metal Precursors and Conversion into CZTS Ffilms

4.1.1 Introduction

As mentioned in Chapter 2, several routes are available to prepare the metal films (precursors) using sputtering. Our approach for preparing CZTS films begins with the deposition of stacked and co-sputtered metal precursors using single metal targets of copper, zinc, and tin. Again, the main advantage of depositing a stacked precursor is the ease of controlling the metal film composition by varying the thickness of each element, whereas co-sputtered precursors can provide a more homogenous mixture of the elements, which could result in final CZTS films with better uniformity of thickness and composition.

Controlling the chemical composition is critical to producing high-quality CZTS films without secondary phases. In addition, the thickness of the final CZTS film must be in a certain predefined range to optimize the light absorption and hence the solar cell performance and to minimize the processing time and consequentially the production cost. Too thin absorber layer introduces optical losses by not absorbing all the incident radiation, thus minimizing the generation of electron-hole pairs in the active layer of the solar cell, which reduces the number of collected charge carriers. On the other hand, thicker absorber layers means wasted excess material and increased deposition time. The incident light will be totally absorbed within just a few microns of the film. For CZTS with an absorption coefficient greater than 10^4 cm^{-1}, a film thickness of 1–3 µm is sufficient to absorb most of the light spectrum.

In this section, we provide the procedure to calibrate the sputtering system to determine the deposition rate and the time required to deposit precursors with a certain composition and thickness. Moreover, we present the essential results regarding the conversion of the metal films into CZTS films.

4.1.2 Deposition of the metal films

4.1.2.1 Theoretical calculation of the precursor thickness

The required CZTS thin-film thickness as an active layer for the device ranges from 1 to 3 µm. When considering the expansion of the film by incorporated sulfur during the sulfurization process, precursor thicknesses of even less than 1 µm is sufficient to end up with final CZTS films having the required thickness. This calculation is based on a stacked metal precursor with a thickness of 1 µm. Theoretically, we can determine the composition of a compound in terms of the percentage of its constituents, and from that, we can calculate the thickness of each metal layer. The metal ratio of Cu:Zn:Sn in a stoichiometric Cu_2ZnSnS_4 is 2:1:1. Using the density and atomic weight of the three metals listed in Table 3.1, we can determine the molar mass of the metals as follows:

Mass of Cu = 2 mol * 63.55 g/mol = 127.1 g

Mass of Zn = 1 mol * 65.38 g/mol = 65.38 g

Mass of Sn = 1 mol * 118.7 g/mol = 118.7 g

From the density (ρ) = mass (g) / volume (v), the volume occupied by each element can be calculated as follows:

Volume of Cu = 127.1 g/8.96 g.cm^{-3} = 14.185 cm^{3}

Volume of Zn = 65.38 g/7.14 g. cm^{-3} = 9.157 cm^{3}

Volume of Sn = 118.7 g/7.31 g.cm^{-3} = 16.240 cm^{3}

Because the area occupied by each element will be the same as when they are deposited on the same substrate, the thickness percentage of Cu, Zn, and Sn can be calculated to be 35.84%, 23.14%, and 41.02%, respectively. For a 1-µm-thick precursor, the thickness of Cu, Zn, and Sn layers will be about 358, 231, and 410 nm, respectively.

Table 4.1: Density and atomic weight of Cu, Zn, and Sn.

Element	Density (g/cm^{3})	Atomic Weight (g/mol)
Cu	8.96	63.55
Zn	7.14	65.38
Sn	7.31	118.7

4.1.2.2 Calibration of the sputtering system

After theoretically determining the thickness of each metal layer leading to a stoichiometric composition of a 1-µm-thick precursor, the sputtering system first needs to be calibrated to determine the deposition rate. At first, the sputtering time for each metal layer was fixed at 60 minutes to apply the obtained working powers in subsequent co-sputtering deposition. For each element, three different working sputter powers were selected to estimate the deposition rate. The powers selected were 50, 60, and 70 W for copper; 40, 50, and 60 W for zinc; and 25, 35, and 45 W for tin. A DekTak Profilometer was used to measure the thickness of the deposited metal precursors. Figure 4.1 shows the power vs. thickness curves of the three metals. The deposition rates for Cu were 2.17, 2.67, and 3.5 nm for the working powers of 50, 60, and 70 W, respectively. Higher deposition rates were determined for Zn and Sn deposited at lower RF powers. As can be seen, Cu and Zn exhibit nearly linear behavior that could be used to estimate the power needed to deposit the required thicknesses. Considering that the calculated thicknesses for Cu and Zn layers are about 360 and 230 nm, respectively, and assuming a linear power-thickness relation for Cu and Zn, then the estimated powers to deposit a 360-nm-thick layer of Cu and 230-nm-thick layer of Zn are (from the graph) 110 and 41 W, respectively. The power-thickness behavior of Sn shows a slightly different behavior. However, the power of 35 W used for Sn results in a thickness of 425 nm, which is very close to the required value of 410 nm. Hence, this power was used for Sn, and a power of 40 W was chosen for Zn. For Cu, a power of 100 W instead of 110 W was chosen in order to fabricate a Cu-poor rather than stoichiometric precursor. As mentioned previously, CZTS solar cells showing high efficiencies were made out of Cu-poor and Zn-rich CZTS films; therefore, we will attempt to produce Cu-poor films with our selections.

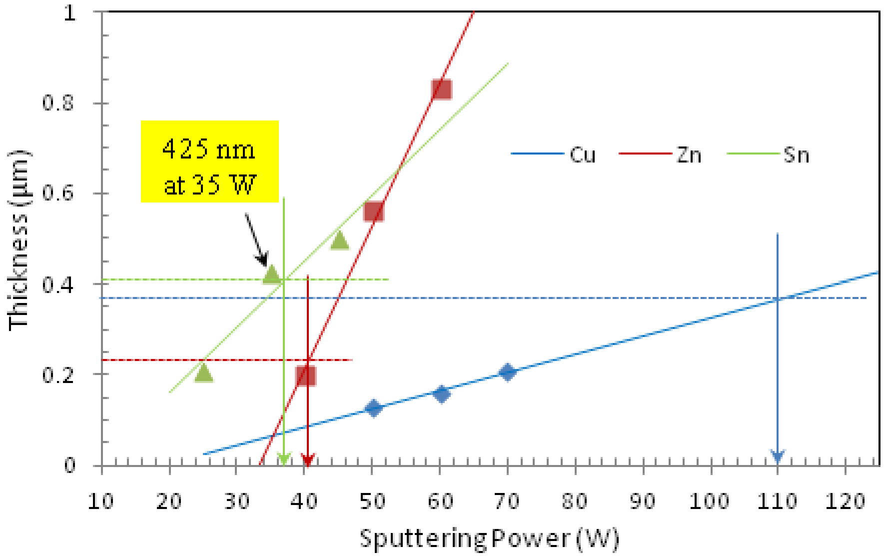

Figure 4.1: Thickness-power behaviors for Cu, Zn, and Sn.

Based on the estimated powers for the three metals, a stacked precursor was sputtered with the stack order Zn/Sn/Cu on a Mo-coated glass substrate. The choice of this stack sequence was based on what was reported in the literature—that this stack order leads to single-phase kesterite CZTS, better crystal quality, and reduced Zn and Sn loss during the annealing treatment [120], [202]. The measured thickness of this precursor was about 1.2 µm, which is close to the target thickness. The precursor's chemical compositions from XRF measurements are listed in Table 4.2. Clearly, the precursor shows a slightly Cu-rich and Sn-poor composition, whereas a stoichiometric composition was achieved for Zn. The results suggest that decreasing the sputtering power for Cu—or alternatively, a slight decrease in the Cu sputtering power with slight increase of the power for Sn—could result in the required composition.

Table 4.2: Chemical composition of a stacked metal precursor deposited on Mo-coated glass substrate with the powers 100, 40, and 35 W for Cu, Zn, and Sn, respectively.

Sample	Cu (%)	Zn (%)	Sn (%)	Cu/(Zn+Sn)	Zn/Sn
85	52.2	25.3	22.5	1.10	1.12

For further tuning of the composition, two new precursors were deposited. Precursor 86 was deposited with the powers 95, 40, and 36 W for Cu, Zn, and Sn, whereas for precursor 87, the power for Cu was lowered to 90 W by keeping the sputtering powers for Zn and Sn at 40 and 35 W, respectively. The chemical compositions of the two precursors are represented in Table 4.3. Precursor 86 is showing nearly stoichiometric values, whereas precursor 87 is slightly Cu-poor and Zn-rich, corresponding to the set target.

Table 4.3: Chemical composition of two stacked metal precursors deposited with different powers for Cu, Zn, and Sn. For sample 86, the sputtering powers for Cu, Zn, and Sn were 95, 40, and 36, respectively. For sample 87, powers of 90, 40, and 35 W were applied for the Cu, Zn, and Sn targets, respectively.

Sample	Cu (%)	Zn (%)	Sn (%)	Cu/(Zn+Sn)	Zn/Sn
86	49.1	25.7	25.2	0.96	1.02
87	47.4	26.7	25.9	0.90	1.03

The sputtering parameters determined from depositing a stacked precursor with stoichiometric and Cu-poor and Zn-rich composition were applied to deposit co-sputtered precursors with similar compositions. In the first attempt, the sputtering conditions used to prepare sample 85 were adapted, and the co-sputtered precursor was notably Zn-rich and Sn-poor. The chemical composition obtained from XRF measurements showed 50.90%, 32.90%, and 16.20% for Cu, Zn, and Sn, respectively, suggesting the increase of

Sn sputtering power and the decrease of the power applied to the Zn target. Varying the sputtering power applied to the three metal targets and measuring the elemental composition showed that there is interplay between the sputtered species, and the composition cannot be controlled by only changing the deposition rate of one element independently from the other two metals. After several trial-and-error attempts, a Cu-poor and Zn-rich composition for the sputtered precursor was achieved (Cu/(Zn+Sn) = 0.82 and Zn/Sn = 1.1). Another difference between the stacked and co-sputtered precursors was the final thickness and the surface roughness. DekTak measurements revealed that stacked precursors are thicker and exhibit rough surface compared to the co-sputtered metal films. Figure 4.2 shows the DekTak profile of co-sputtered and sequentially deposited metal precursors deposited under the same conditions. The thickness difference between both films was about 0.3 μm.

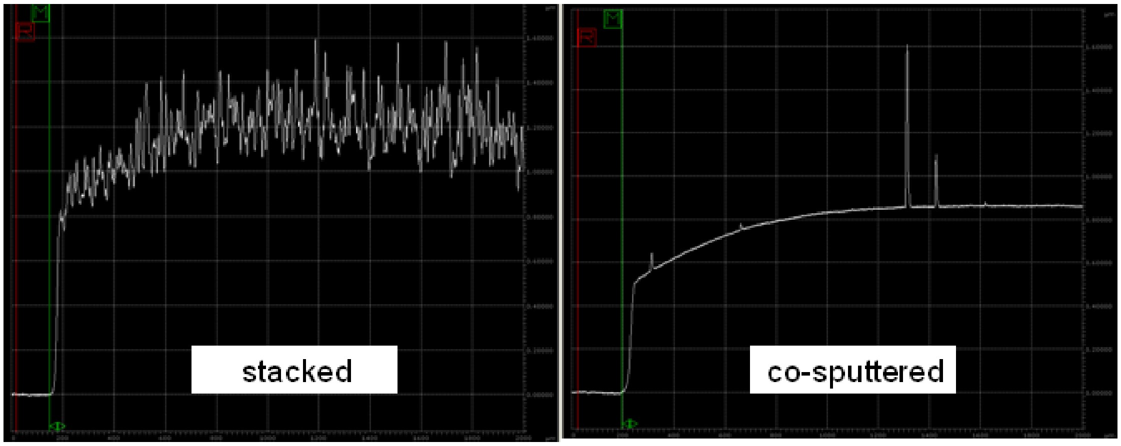

Figure 4.2: DekTak profiles of stacked and co-sputtered metal precursors deposited under the same sputtering conditions.

4.1.3 Converting the metal precursor into CZTS films

The second step in our approach to prepare CZTS films is the annealing of the metal precursors in sulfur ambient (sulfurization). The setup of the sulfurization apparatus and the description of the sulfurization process were already introduced in Chapter 3. The CZTS phase is expected to form from intermediate binary metal sulfides and ternary Cu-Sn sulfides, including CuS, Cu_2S, ZnS, SnS, SnS_2, and Cu_2SnS_3 [203], [204]. Choosing the sulfurization parameters such as the substrate temperature and duration is very crucial for the crystallization of CZTS, and the question was what temperature we should begin with and for how long. A wide range of substrate temperatures and annealing times have been reported in the literature, including values from 300 °C to 600 °C for the temperature and values from 5 min to 6 hours for the durations [64], [69], [146], [155], [205]–[213]. As a start, several sulfurization conditions were tried; nonetheless, a sulfurization temperature of 550 °C was typically selected to anneal the metal precursors for 60 min. In the preliminary experiment, stacked and co-sputtered metal precursors were sulfurized to study the basic properties of CZTS. These include the chemical composition using XRF and EDS, crystallographic structure using XRD, and the morphology using SEM. DekTak and SEM were employed to determine the thickness of the metal films and the final CZTS films. Figure 4.3 shows a flow chart of the fabrication and characterization steps used in the first stage of this study.

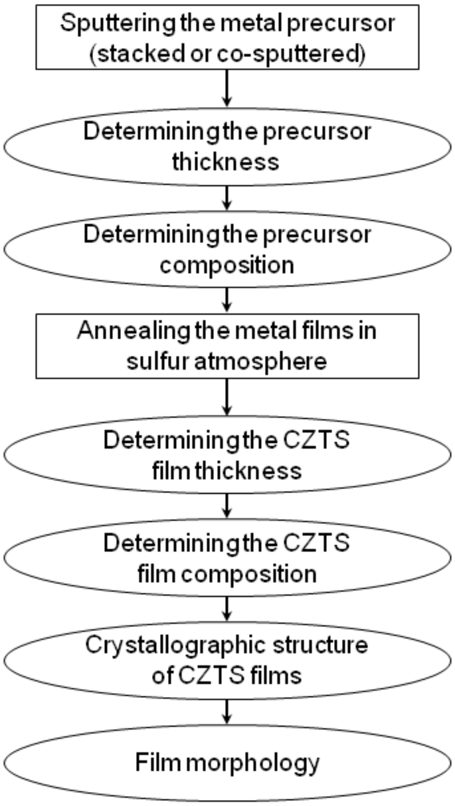

Figure 4.3: Fabrication and characterization steps used in the first stage of this study.

In the following, we will present two CZTS thin films that were prepared by the sulfurization of stacked (film #92) and co-sputtered (film #95) metal precursors. Precursor 92 with the stack SLG/Mo/Zn/Sn/Cu was deposited using sputtering powers of 87, 40, and 35 W for Cu, Zn, and Sn, respectively. The deposition time for each metal layer was 60 min. For precursor 95, co-deposition was for 60 min using sputtering powers of 70, 30, and 40 W for Cu, Zn, and Sn, respectively. The chemical composition of both metal films is listed in Table 4.4. Both precursors exhibit Cu-poor and Zn-rich composition that was targeted to produce CZTS films for solar cell application. The metal films were thereafter annealed in sulfur vapor at 550 °C for 60 min.

Table 4.4: Chemical composition of stacked and co-sputtered metal precursors prepared for the sulfurization at 550 °C for 60 min.

Sample	Precursor type	Cu (%)	Zn (%)	Sn (%)	Cu/(Zn+Sn)	Zn/Sn
92	Stacked	46.8	28.3	24.9	0.88	1.14
95	Co-sputtered	44.9	28.5	26.6	0.81	1.07

The chemical composition of both CZTS films is shown in Table 4.5. Film 92 shows similar values to the metal precursor whereas the film prepared from co-sputtered precursor exhibits significant loss of Sn. The XRD spectra of the sulfurized CZTS films are illustrated in Figure 4.4. For both films, the XRD patterns show peaks that coincide with the kesterite CZTS phase according to JCPDS card # 26-0575. Some preferential orientation in the (112) plane was observed by comparing the intensities of the CZTS main peaks. The XRD pattern of film 92 also reveals the presence of Cu-S secondary phases, whereas they could not be clearly detected in the co-sputtered film. However, an EDS scan over some grains of film 95 revealed the presence of Cu-S phases by the detection of high concentration of copper and sulfur. A plan-view SEM micrograph of film 95 is shown in Figure 4.5, where the Cu-S grains with their unique crystal shapes can clearly be seen on the film surface.

Table 4.5: Chemical composition of final CZTS films 92 and 95, prepared by the sulfurization of stacked and co-sputtered metal precursors at 550 °C for 60 min.

Sample	Precursor type	Cu (%)	Zn (%)	Sn (%)	Cu/(Zn+Sn)	Zn/Sn
92	Stacked	47.2	28.6	24.2	0.89	1.18
95	Co-sputtered	46.8	33.0	20.2	0.88	1.63

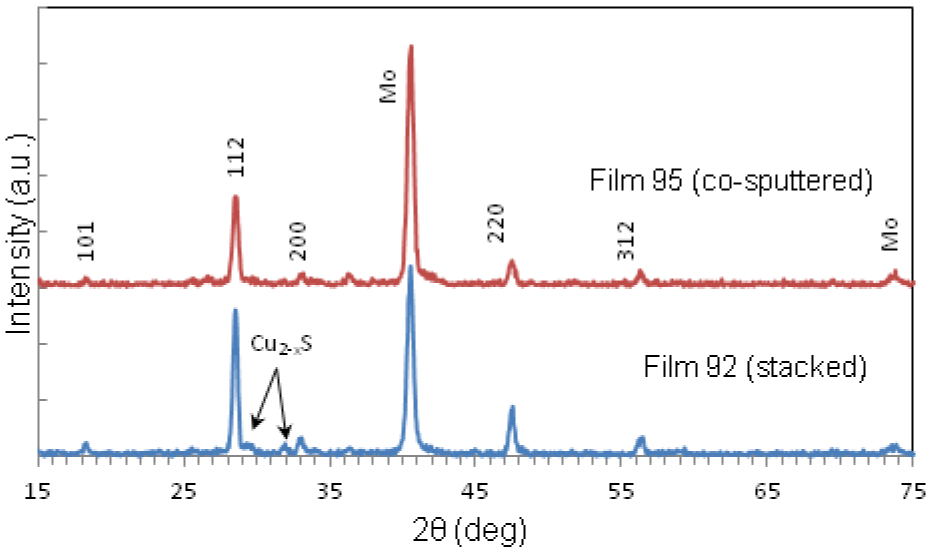

Figure 4.4: XRD spectra of CZTS films prepared by the sulfurization of stacked and co-sputtered metal precursors at 550 °C for 60 min.

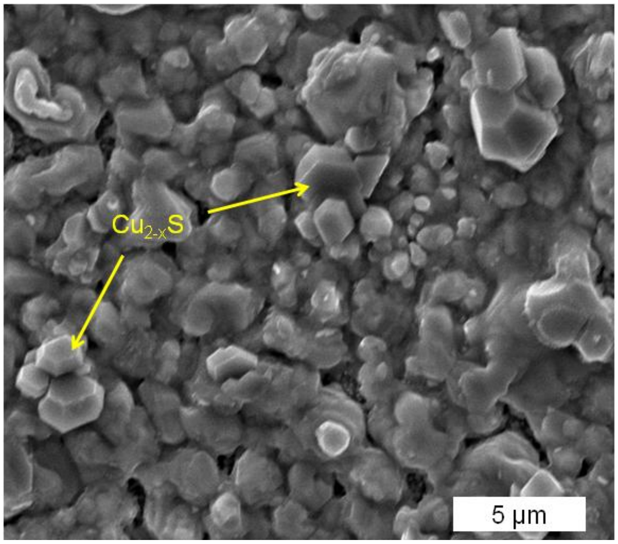

Figure 4.5: SEM plan micrograph of co-sputtered CZTS film, showing the presence of $Cu_{2-x}S$ secondary phases on the film surface.

4.1.4 Conclusion

Using the sputtering deposition method, thin metal films of Cu, Zn, and Sn were put down as stacked layers by depositing one metal layer at a time and as a mixture of the three metals by co-sputtering. The sputtering system was calibrated using several sputtering powers applied to the metal targets in order to determine the sputtering rates, and consequentially, to develop a route to control the composition and thickness of the deposited precursors. After determining the deposition rates of the three metals, the working powers leading to the required chemical composition and thickness of the precursor could be predicted and the targeted goals could be achieved with only a few depositions and measurements. Results showed that controlling the composition of the stacked films is easier than that of co-sputtered films by varying the thickness of the individual metal layers. The metal precursors were also successfully converted into CZTS films via the sulfurization process. The preliminary annealing experiments showed a clear impact of the sulfurization parameters on the properties of the final films, suggesting the performance of systematic studies to investigate the influence of the sulfurization temperature and duration on the compound properties.

4.2 Influence of the sulfurization temperature and duration

Some of the results presented in this section were published in: M. Abusnina, H. Moutinho, M. Al-Jassim, C. DeHart, and M. Matin, “Fabrication and Characterization of CZTS Thin Films Prepared by the Sulfurization of RF-Sputtered Stacked Metal Precursors,” *Journal of Electronic Materials*, Vol. 43, No. 9, 2014.

4.2.1 Introduction

Besides controlling the chemical composition of the metal precursor, the sulfurization process represents a central key for forming CZTS. As mentioned in Chapter 3, many parameters can be varied, including the substrate temperature, heating time, temperature ramping time, vapor pressure inside the tube, and carrier gas flux. Several published works reported on the impact of sulfurization temperature and time on the growth and properties of Cu_2ZnSnS_4 thin films.

Guan *et al.* [214] studied the sulfurization time effect on the structural, optical, and compositional properties of CZTS films prepared using the solution-based chemical bath deposition method. They found that films sulfurized for 20 and 40 min exhibit $Cu_{2-x}S$ and Cu_2SnS_3 secondary phases, whereas those annealed for 60, 80, 100 min showed single-phase CZTS. Consequentially, the energy bandgap of the sulfurized films showed variation due to the presence of secondary phases. In sulfurizing sputtered stacked metal precursors at temperatures between 500 °C and 575 °C for 3–4 hours, Emrani *et al.* [215] reported achieving compact CZTS films with large grains leading to solar cells with an efficiency of 5.75% when using a sulfurization temperature of 550 °C. The films sulfurized at lower temperatures showed voids, small grains, and the presence of some secondary phases. González *et al.* [216] sulfurized sputtered metal precursors at 520 °C for 10, 30, and 90 min and found that the crystallite sizes showed some increase when increasing the annealing time. Gurav *et al.* [136] studied the effect of soft annealing of metal precursors prepared using electrodeposition. The precursors experienced soft annealing treatment at temperatures of 250 °C–300 °C in Ar atmosphere for 1 h before they were sulfurized at 580 °C for 2 hours. They achieved single-phase CZTS films when soft annealing the precursors with a temperature of 300 °C whereas secondary phases were present in films treated with 250 °C and 350 °C. Ge *et al.* [217] compared the influence of the sulfurization ramping time using two different annealing ramping rates and found that slow ramping results in films with better crystallinity. Khalkar *et al.* [218] sulfurized co-sputtered precursors at different sulfurization pressures in a H_2S/N_2 atmosphere at 550 °C for one hour and compared the performance of solar cells based on CZTS absorber layers prepared at different sulfurization pressures. They achieved a conversion efficiency of 6.75% with CZTS films sulfurized at atmospheric pressure, whereas an efficiency of only 1.67% is obtained when using CZTS absorber sulfurized at low pressure. Pawar *et al.* [132] fabricated void-free CZTS thin films by sulfurization of stacked metallic precursor films at 580 °C for 60, 120, and 180 films. They showed an increase in the energy bandgap by increasing the annealing time. Seol *et al.* [45] sulfurized sputtered precursors in Ar+S_2(g) at 250 °C–400 °C and announced the enhancement of film crystallinity with the increase of the annealing temperature. Sulfurizing Cu/ZnSn/Cu stacked precursors in sulfur vapor at 560 °C and 580 °C for 30 min with a ramping rate of 100 °C/min, Chalapathy *et al.* [219] reported single-phase

CZTS films and achieved a solar cell conversion efficiency of 4.59%. Using a Cu–Zn–Sn ternary alloy target, Amal *et al.* [220] annealed sputtered metal precursors at 530 °C, 550 °C, and 570 °C for 30 min in Ar/H_2S environment with a heating rate of 10 °C/min, and reported films with no secondary phases and with compact morphology using a substrate temperature of 570 °C.

Generally, most of the published work agrees that the increase of both sulfurization temperature and time leads to improved morphology and crystallinity, avoids the evolution of secondary phases, and affects the energy bandgap of the produced CZTS films; however, the values published for annealing temperatures and duration are not the same. The small deviation in the reported values resulted in high-quality CZTS films, which could be due to the different growth method used to prepare the precursors and to the different setups of the sulfurization process used to convert the precursors into CZTS films.

The aim in this study was, first, to optimize the sulfurization process and determine the range of substrate temperature and sulfurization time leading to high-quality films. Second, we wanted to investigate the impact of the substrate temperature and sulfurization duration on the properties of the final CZTS films and to understand the formation pathway, as well. Literature reports that CZTS starts crystallizing at an annealing temperature of 400 °C and that temperatures up to 600 °C resulted in films with good crystallinities [143], [205]; therefore, we selected a combination of three different temperatures with three annealing times, yielding a total of nine conditions. The selected annealing times and substrate temperatures were 30, 60, and 120 min and 450 °C, 500 °C, and 550 °C.

4.2.2 Experimental

The metal precursors were deposited as a stack onto 2.5×2.5-cm^2 Mo-coated SLG substrates with the sequence Mo/Zn/Sn/Cu using RF sputtering powers of 85, 40, and 38 W applied to Cu, Zn, and Sn single targets, respectively, for 60 minutes. Five metal precursors were prepared in total with the same sputtering conditions to investigate the effect of the sulfurization parameters. After the deposition, each precursor was cut into two pieces. Of the ten precursors, nine were sulfurized under different conditions. An X-ray fluorescence spectrometer from Solar Metrology (System SMX) was used to determine the chemical composition of the as-deposited metal films. The metal precursors were then annealed in sulfur vapor and N_2 environment using the three-heating-zone quartz-tube furnace. The sulfurization profile used in this study is illustrated in Figure 4.6. The ramping times for the three furnace zones were kept constant (10 min for the substrate zone and 5 min for the buffering and sulfur zone). For all conditions, the buffering zone was heated at 350 °C and the sulfur zone at 220 °C. After sulfurization, the tube was cooled naturally. Surface and cross-section morphology of the sulfurized films was characterized by SEM, which was also used to determine the thicknesses of the precursors and final CZTS films. Crystallographic structure of the CZTS films was carried out by X-ray diffraction (XRD). Energy-dispersive spectroscopy (EDS) was employed to determine the chemical composition of the final CZTS films, and also, as a complementary technique to XRD for identifying secondary phases. In addition to XRF and EDS, electron probe microanalysis (EPMA) and Auger electron spectroscopy (AES) were used to determine the composition of the films. To analyze the optical properties of the synthesized CZTS films, new films were fabricated on SLG substrates (without the back-contact Mo layer) to enable light transmission through the film. Measuring the optical properties of the films was done by an ultraviolet (UV) spectrophotometer.

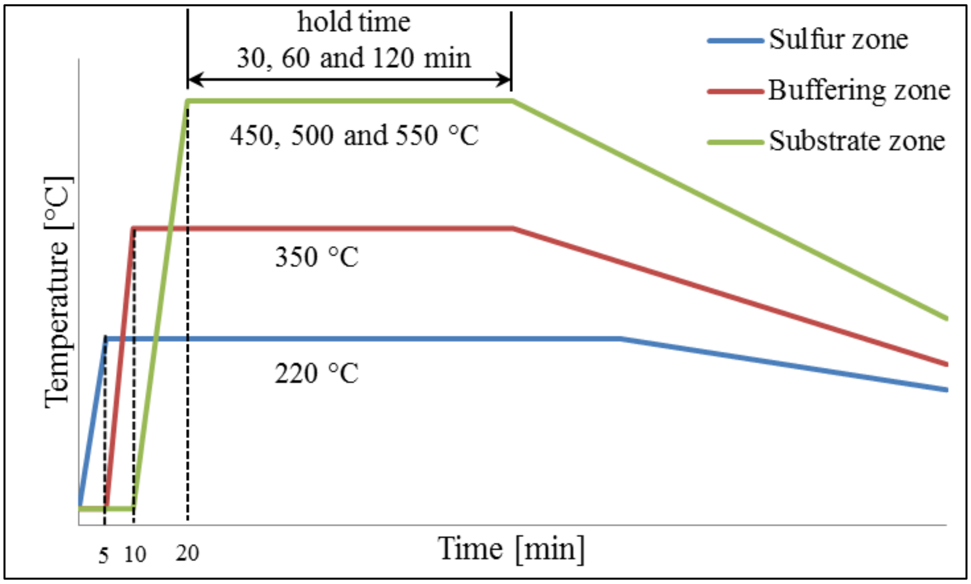

Figure 4.6: Schematic illustration of the annealing temperatures and durations used. The cool-down curves for the three zones are not to scale [141].

4.2.3 Results and discussions

To investigate the thickness uniformity of the precursors over the entire substrate, one of the as-deposited films was cut into nine pieces to perform cross-sectional SEM thickness measurement. The measurements were conducted at the center of each piece as shown in Figure 4.7. Compositional ratios of this precursors from XRF were 0.89 for Cu/(Zn + Sn) and 1.13 for Zn/Sn. SEM thickness measurements at various areas showed that the precursor’s thickness ranges between about 1.04 and 1.38 μm, with an average of about 1.2 µm, confirming the surface roughness of stacked precursors revealed by DekTak measurements. From the cross-sectional micrographs, the relatively large grains of the copper top layer could be easily identified. The thickness of the Cu layer varied between about 450 and 480 nm. On the other hand, Zn and Sn layers could not be distinguished. In addition to the rough surface, the metal films showed features of voids near the Mo/film interface.

Table 4.6: The elemental composition and the composition ratios of the as-deposited stacked metal precursors from XRF.

Precursor	**Cu (%)**	**Zn (%)**	**Sn (%)**	**Cu/(Zn+Sn)**	**Zn/Sn**
97	47.4	27.7	24.9	0.90	1.11
98	47.1	28.2	24.7	0.89	1.14
99	47.4	27.1	25.5	0.90	1.06
102	47.3	27.8	24.9	0.90	1.12
104	46.4	27.9	25.7	0.87	1.09

The elemental compositions of the as-deposited precursors are shown in Table 4.6. All precursors exhibit slightly Cu-poor and Zn-rich concentrations, whereas Sn shows nearly stoichiometric values.

Table 4.7: Sulfurization conditions assigned to the precursors.

	450 °C	**500 °C**	**550°C**
30 min	97-1	102-1	99-1
60 min	98-1	102-2	104-1
120 min	97-2	98-2	99-2

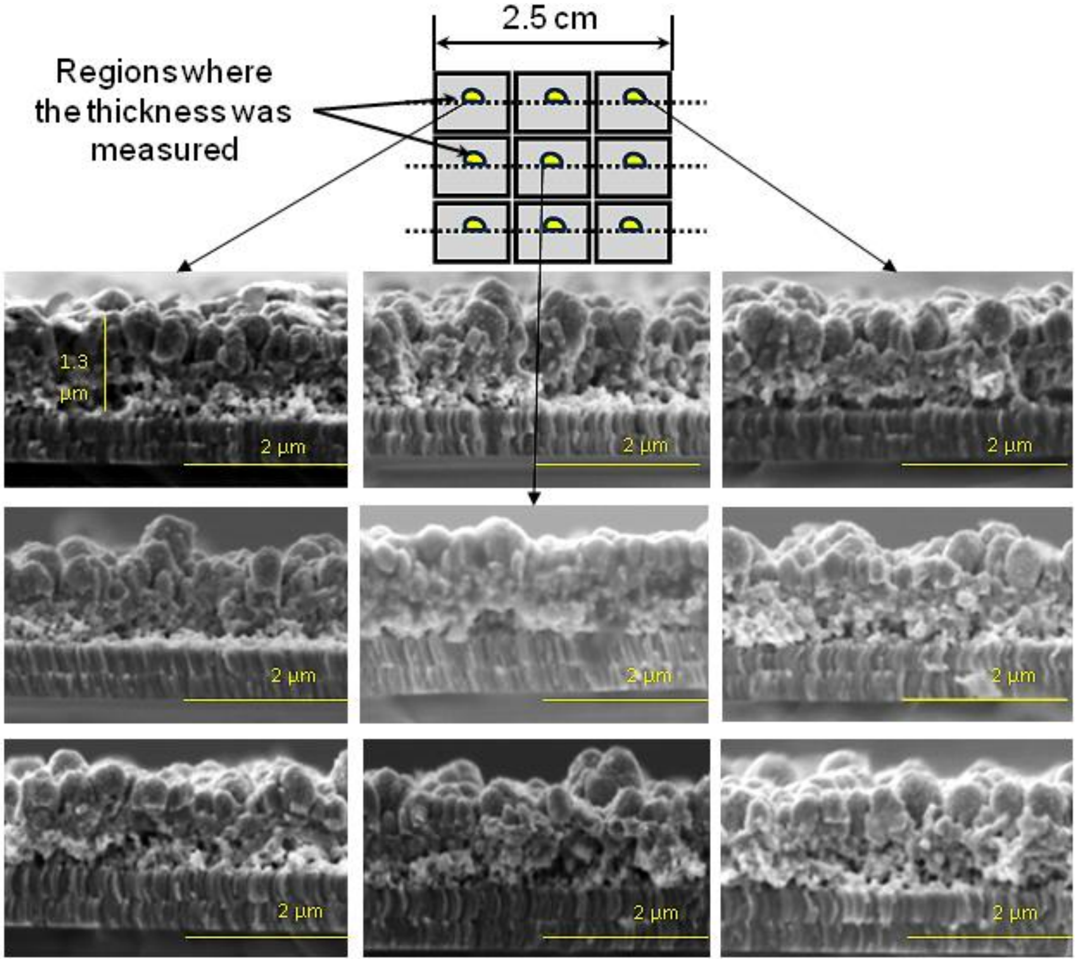

Figure 4.7: Cross-sectional SEM micrographs of metal precursor taken at different regions to investigate the thickness uniformity.

Table 4.7 shows the sulfurization conditions assigned to the precursors. To clearly connect the fabricated CZTS films to the different annealing conditions, the samples will be identified in the following by substrate temperatures and sulfurization times instead of by sample names.

4.2.3.1 Composition study

The composition data from XRF showing the metal concentration in the sulfurized CZTS films is listed in Table 4.8. Generally, the Zn content in the films with an average of about 28.50% did not show a noticeable difference to the values obtained for the precursors. In contrast, Cu and Sn ratios showed variations that could not be clearly connected to a trend with respect to temperature or time changes. Indeed, some of the values are unexpected. For instance, Sn loss was expected after annealing, as reported elsewhere [221], especially when using high temperatures and long duration. However, on the contrary, Sn showed a concentration of 26.43% in the film treated at 550 °C for 120 min, higher than that of the film annealed at 450 °C for 30 min. Based on these results, detailed investigation of the films' composition is needed to clarify the discrepancies.

Table 4.8: Chemical composition from XRF for the CZTS films sulfurized at different conditions.

Film	**Cu (%)**	**Zn (%)**	**Sn (%)**	**Cu/(Zn+Sn)**	**Zn/Sn**
A: (450 °C, 30 min)	48.6	28.6	22.8	0.95	1.25
B: (450 °C, 60 min)	45.8	27.1	27.1	0.85	1.00
C: (450 °C, 120 min)	49.0	27.9	23.1	0.96	1.21
D: (500 °C, 30 min)	44.7	29.7	25.6	0.81	1.16
E: (500 °C, 60 min)	44.3	31.1	24.6	0.80	1.26
F: (500 °C, 120 min)	42.7	28.9	28.4	0.75	1.02
G: (550 °C, 30 min)	45.6	27.6	26.8	0.84	1.03
H: (550 °C, 60 min)	44.6	28.3	27.1	0.81	1.04
I: (550 °C, 120 min)	45.8	27.8	26.4	0.85	1.05

EDS chemical composition data acquired at 15 kV are listed in Table 4.9. Similar to the XRF data, no clear trend correlates the data to the various sulfurization conditions. Unlike the XRF data, the composition of the films annealed at 550 °C indicates a slight loss of Sn. Almost all sulfurized films, except the ones treated at 500 °C for 120 min and at 550 °C for 60 min, exhibit a high S/metal ratio close to stoichiometric, indicating the completion of the annealing process. In some films, a high amount of Zn and Cu was detected that could indicate the presence of ZnS and $Cu_{2-x}S$ phases.

Table 4.9: Chemical composition from EDS for the CZTS films sulfurized at different conditions.

Film	Cu (%)	Zn (%)	Sn (%)	S (%)	S/metals	Cu/(Zn+Sn)	Zn/Sn
A: (450 °C, 30 min)	23.4	16.2	13.0	47.4	0.90	0.80	1.25
B: (450 °C, 60 min)	23.4	19.00	10.7	46.9	0.88	0.79	1.78
C: (450 °C, 120 min)	20.3	16.3	15.7	47.7	0.91	0.63	1.04
D: (500 °C, 30 min)	19.9	16.2	12.2	51.7	1.07	0.70	1.33
E: (500 °C, 60 min)	23.4	17.3	12.5	46.8	0.88	0.79	1.38
F: (500 °C, 120 min)	33.2	19.0	13.1	34.7	0.53	1.03	1.45
G: (550 °C, 30 min)	18.4	20.5	9.4	51.7	1.07	0.62	2.18
H: (550 °C, 60 min)	23.9	27.5	11.2	37.4	0.60	0.62	2.46
I: (550 °C, 120 min)	23.8	15.4	10.8	50.0	1.00	0.91	1.43

Table 4.10: Chemical composition from EPMA for the CZTS films sulfurized at different conditions.

Film	Cu (%)	Zn (%)	Sn (%)	S (%)	S/metals	Cu/(Zn+Sn)	Zn/Sn
A: (450 °C, 30 min)	33.9	9.5	9.0	47.6	0.91	1.83	1.06
B: (450 °C, 60 min)	27.3	11.1	10.6	51.0	1.04	1.26	1.05
C: (450 °C, 120 min)	27.8	9.7	11.2	51.3	1.05	1.33	0.87
D: (500 °C, 30 min)	24.0	17.8	8.4	49.8	0.99	0.92	2.12
E: (500 °C, 60 min)	23.2	17.4	9.2	50.2	1.01	0.87	1.89
F: (500 °C, 120 min)	24.2	10.6	12.9	52.3	1.10	1.03	0.82
G: (550 °C, 30 min)	20.6	19.0	9.6	50.8	1.03	0.72	1.98
H: (550 °C, 60 min)	22.4	16.4	10.5	50.7	1.03	0.83	1.56
I: (550 °C, 120 min)	21.9	18.2	9.5	50.4	1.02	0.79	1.93

EPMA measurement was conducted to better evaluate the film composition. The data are shown in Table 4.10. In contrast to EDS, EPMA data show a stoichiometric sulfur value for almost all films, indicating complete incorporation of sulfur in the films. For the film annealed at 450 °C for 30 min, a high Cu value and low Zn and Sn values were observed. Because Cu is the top layer in the metal stack, this result could mean that the interdiffusion of the metals is not complete and that only the elements near the surface were detected. An increase in the sulfurization time to 60 and 120 min at the same temperature results in a decrease in the Cu amount, which could indicate better migration of Cu toward the bulk and Zn toward the surface. Generally, the films annealed at 450 °C showed a high concentration of Cu. The films annealed at 500 °C and 550 °C show a Cu ratio close to the initial precursor values and high Zn/Sn ratios compared to the metal precursors.

4.2.3.2 Study of the crystallographic structure

The XRD spectra of all sulfurized CZTS films are shown in Figure 4.8. The spectra are categorized into three groups, with each group including three films annealed at the same temperature for different durations. In general, all XRD patterns exhibit good crystallinity in the form of sharp peaks that correspond to the kesterite CZTS phase according to JCPDS card No. 26-0575; however, the patterns revealed extra peaks, indicating the presence of secondary phases. Some preferential orientation in the (112) plane was observed in the XRD patterns of all CZTS films. The peaks not belonging to CZTS and located at 2θ values of 26.6°, 29.9°, 31.8°, 33.9°, 46.3°, and 51.9° could be best assigned to Cu_2SnS_3, Cu_2S, and CuS. Some of the extra peaks could not be clearly attributed to a specific phase. As mentioned in Chapter 2, the ZnS phase cannot be detected using XRD because it has peaks at the same positions of those of kesterite CZTS; nevertheless, a diffraction peak located at 51.9° in the spectrum of the film sulfurized at 450°C for 30 min could belong to ZnS (JCPDS 2-1310). The presence of the ZnS phase in the final CZTS was expected because the metal precursors are Zn-rich. Regarding the Sn-S phases, no clear evidence of their existence could be observed.

450 °C

By comparing the spectra of the CZTS films annealed at 450 °C for 30, 60, and 120 min (Figure 4.8a), we noticed an increase in the 112 peak intensity and a slight decrease in the full width at half maximum (FWHM) of this peak when increasing the sulfurization time from 30 to 60 and 120 min. This clearly indicates enhanced crystal quality of the film when annealed for a longer time at this temperature. Furthermore, increasing the sulfurization time clearly impacted the formation of secondary phases so that the peaks assigned to them decreased or even disappeared when increasing the duration of annealing. For instance, the peak located at 33.9° in the pattern of the film annealed for 30 min disappeared, whereas the peak located at 26.6° showed a noticeable decrease with increased treatment time.

500 °C

For the peaks corresponding to secondary phases, we observed no change relating their presence to the variation of sulfurization time. However, the 112 peak of the film sulfurized for 120 min showed a slight decrease compared to those of the films annealed for 30 min and 60 min; the other CZTS main peaks did not show any obvious change in intensity. This decrease of the main CZTS peak intensity could imply an altering in the crystal preferential orientation.

550 °C

XRD spectra of the films annealed at 550 °C exhibit similar behavior to that of the films sulfurized at 500 °C, excluding the peak at $2\theta = 26.6°$, which could belong to

Cu-S or Cu-Sn-S phases, that did not appear in the spectrum of the film sulfurized for 30 min.

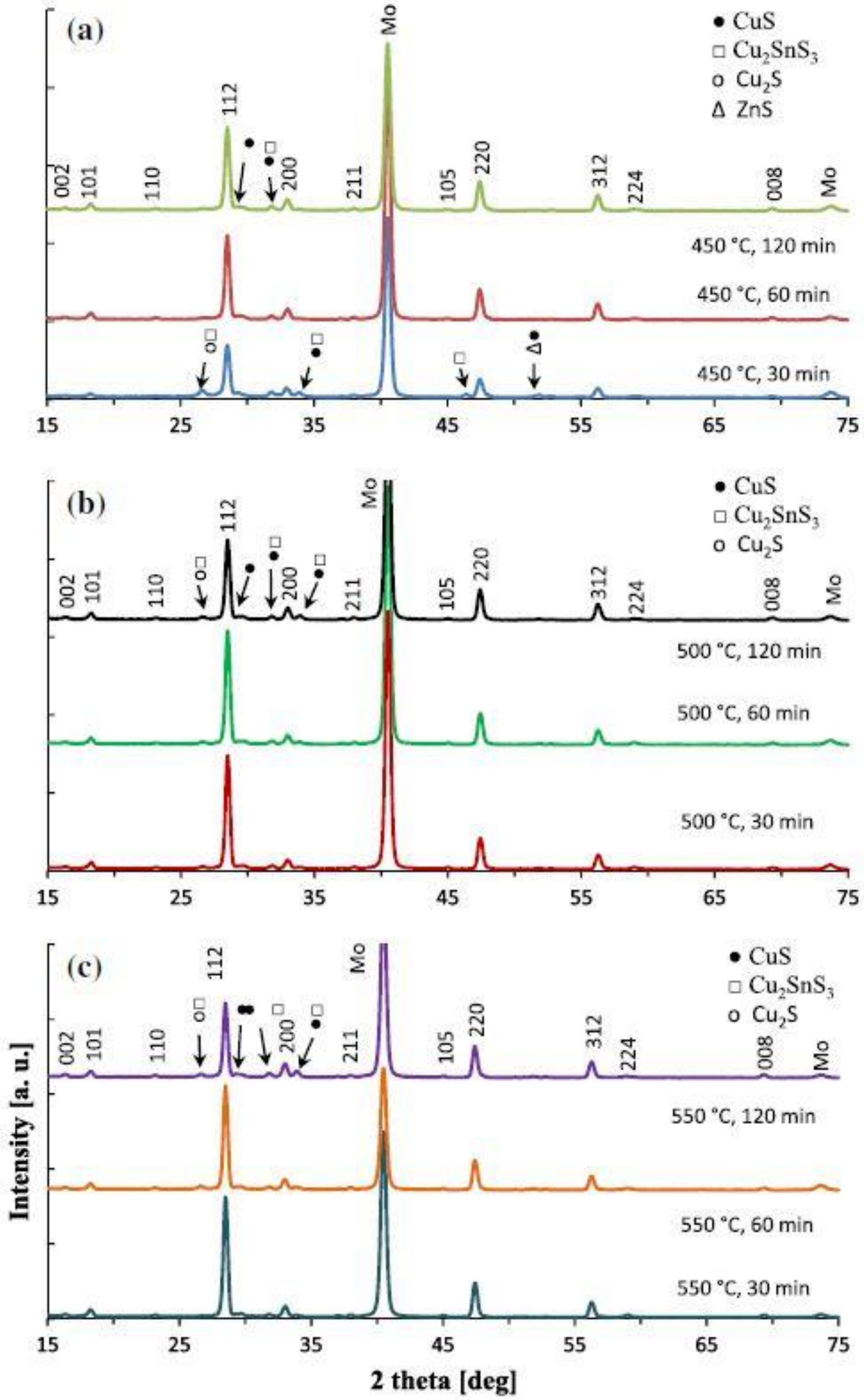

Figure 4.8: XRD patterns of all CZTS films annealed at (a) 450 °C, (b) 500 °C, and (c) 550 °C [141].

4.2.3.3 Study of the film morphology

Figure 4.9 shows plan-view SEM micrographs of the sulfurized CZTS films. EDS scan measurements were conducted at several areas of the films and over individual grains to identify secondary phases based on the concentration of constituents. The grains belonging to different phases identified by EDS are marked on the micrographs by circles for the CZTS phase, squares for the $Cu_{2-x}S$ phases, rectangles for the Cu-Sn-S phases, and triangles for the ZnS phase.

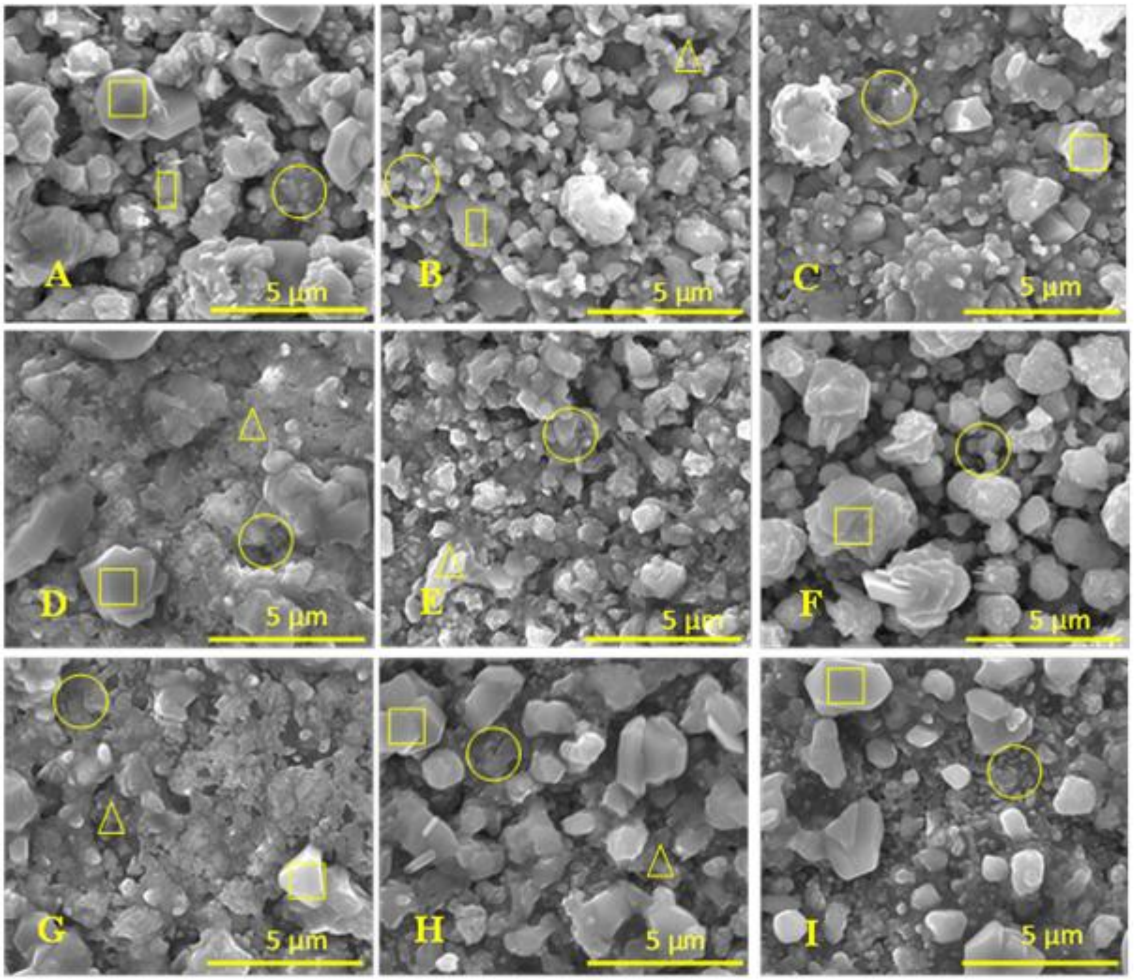

Figure 4.9: Plan-view SEM images of CZTS films sulfurized at various temperatures for different durations [141].

450 °C

The micrograph of the film annealed for 30 min shows a porous morphology in the form of non-compact large-grain features on the surface, leading to a very rough surface. These grains were identified by EDS as $Cu_{2-x}S$. Cu-Sn-S phases were also found in some areas of the film. Some grains also exhibited a high concentration of Zn compared to Cu and Sn, indicating the presence of the ZnS phase. In general, this film showed the formation of various secondary phases in addition to the CZTS phase. Micrograph B shows the impact of increasing the sulfurization time, specifically, a more compact morphology and less secondary phases, indicating enhanced CZTS phase formation. Increasing the annealing duration to 120 min led to improved film compactness and eliminated the ZnS and Cu-Sn-S phases. Only Cu-S phases were identified in this film.

500 °C

The film annealed for 30 min exhibited a dense structure and the presence of Zn-S and $Cu_{2-x}S$ secondary phases in addition to CZTS. Comparing this film with film A, which was sulfurized for the same duration but at a lower temperature, we also note the positive impact of increasing the annealing temperature. This result is consistent with the XRD data, showing improved film crystallinity when annealed at higher temperature. Increasing the sulfurization time resulted in enhanced CZTS phase formation. As seen on the micrograph, the film consists mostly of small CZTS grains generally with an average grain size of less than 1 μm. We identified the formation of Zn-S and $Cu_{2-x}S$ secondary phases, but with lower concentration compared to the films sulfurized at lower temperature or for less duration. For the film annealed for 120 min, we observed the clear segregation of $Cu_{2-x}S$ crystallites on the film surface. The microstructure image shows that the small CZTS grains formed underneath the $Cu_{2-x}S$ crystallites.

550 °C

Generally, the films annealed at 550 °C revealed compact morphology with more $Cu_{2-x}S$ grain segregation on the surface when increasing the treatment duration from 30 min to 60 and 120 min. Film G showed a minimal existence of the ZnS phase.

Cross-sectional SEM micrographs of all sulfurized films are illustrated in Figure 4.10. All films annealed at 450 °C showed voids at the Mo/film interface; however, increasing the sulfurization temperature led to more dense films with fewer or even no voids. Film thicknesses of more than 3.5 μm were measured for the films annealed at 450 °C, independent of the treatment time. On the other hand, the films annealed at 550 °C exhibit an average thickness of about 2.4 μm when neglecting the segregated $Cu2_{-x}S$ crystallites.

In general, Cu-S phases were identified in all sulfurized films no matter what parameters were used to anneal the precursors. The segregation of Cu-S phases in CZTS films has been widely reported in the literature and was explained by the annealing of Cu-rich precursors in sulfur ambient [98], [204]. However, our metal precursors are considered slightly Cu-poor based on the XRF data. Therefore, more investigation is needed to understand the evolution mechanism of these unwanted secondary phases. The presence of these phases, with their metal-like behavior in the absorber layer of the solar cell, is detrimental to the device performance; however, these phases can be removed if accumulated on the surface using potassium cyanide (KCN) etching. Unfortunately, this treatment influences the overall film composition and leads to very Cu-poor films. Several published works reported the successful removal of $Cu_{2-x}S$ crystallites segregated on the CZTS film surface [202].

The segregation of the $Cu_{2-x}S$ grains that are nonuniformly distributed on the film surface explains the discrepancies in the composition of the sulfurized CZTS films obtained by different measurement techniques. It also explains the variation in the elemental concentration that could not be related to the sulfurization conditions. For instance, a high Cu concentration will be measured if we scan an area with a high presence of Cu-S crystallites, and consequently, Zn and Sn will show low concentration, and vice versa.

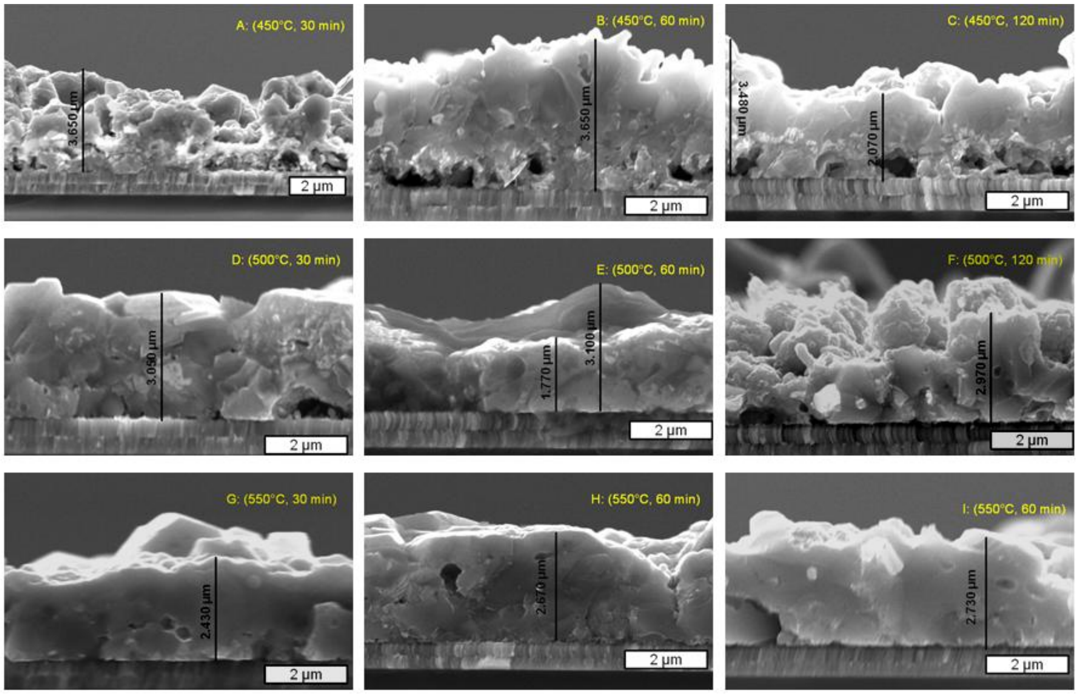

Figure 4.10: Cross-sectional SEM micrographs of all CZTS films sulfurized at different conditions.

To investigate the influence of annealing temperatures higher than 550 °C on the morphology and chemical composition of the CZTS films, we prepared a new metal precursor using the same sputtering conditions applied to the previous ones. The metal film was annealed in sulfur vapor at 600 °C for 120 min, and then characterized by SEM and EDS. The top-view micrograph (Figure 4.11) of this film exhibits a porous and rough surface, but with fewer $Cu_{2-x}S$ crystallites on the surface. An EDS scan over the area shown exhibited a chemical composition of 49.83% S, 24.72% Cu, 13.60% Zn, and 11.85% Sn. Comparing the metal ratios of the final CZTS film to those of the metal precursor showed nearly similar values, with no indication of Sn loss. From these results, we can conclude that higher temperatures and/or longer sulfurization times are required to produce high-quality CZTS films in terms of void-free compact films with fewer or no secondary phases.

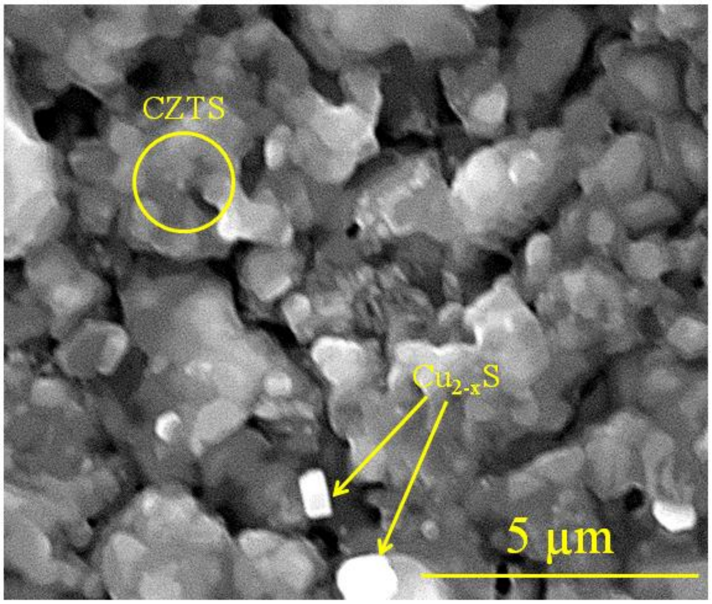

Figure 4.11: Top-view SEM micrograph of CZTS film sulfurized at 600 °C for 120 min [141].

4.2.3.4 Formation of CZTS and reaction pathway

Hergert *et al.* [203] described the formation of kesterite from binary sulfides by a two-step reaction pathway as follows:

$$Cu_{2-x}S + SnS_2 \rightarrow Cu_2SnS_3 \qquad (4.1)$$

$$Cu_2SnS_3 + ZnS \rightarrow Cu_2ZnSnS_4 \qquad (4.2)$$

Schorr *et al.* [204] investigated the reaction of three different mixtures of binary and ternary sulfide compounds at 700 °C and obtained quaternary kieserite Cu_2ZnSnS_4 from all reactions according to the following equations:

$$2CuS + SnS + ZnS \rightarrow Cu_2ZnSnS_4 \qquad (4.3)$$

$$Cu_2S + SnS_2 + ZnS \rightarrow Cu_2ZnSnS_4 \qquad (4.4)$$

$$Cu_2SnS_3 + ZnS \rightarrow Cu_2ZnSnS_4 \qquad (4.5)$$

They also reported that the kesterite CZTS phase starts to form even below 300 °C; however, CuS, SnS, and ZnS phases are present in addition to Cu_2ZnSnS_4. Further investigation of the formation at a temperature range of 350 °C–450 °C showed the presence of ZnS and Cu_2SnS_3, where a transition occurs from Cu-S and Sn-S into Cu_2SnS_3.

In our films, based on XRD and EDS analysis, we observed the formation of Cu-S, Cu-Sn-S, and ZnS phases in addition to CZTS in the films sulfurized at 450 °C for 30 and 60 min, and only $Cu_{2-x}S$ phases were identified when the time was increased to 120 min. The Sn-S phases, including SnS and SnS_2, were not detected. From that, we can infer that binary sulfides are formed earlier in the reaction at low temperature by introducing sulfur vapor to the metals according to the following equations:

$2Cu + S \rightarrow Cu_2S$ (4.6)

$Zn + S \rightarrow ZnS$ (4.7)

$Sn + 2S \rightarrow SnS_2$ (4.8)

According to Eq. 1, the binary sulfides $Cu_{2-x}S$ and SnS_2 will first form Cu_2SnS_3. And considering that Sn is evaporated from SnS phase at temperatures higher than 350 °C [221], [222], we can assume that there is insufficient SnS to react with some $Cu_{2-x}S$ to form Cu_2SnS_3 and that the extra $Cu_{2-x}S$ remains as solid grains in the film. This can be represented by the following equation:

$Cu_{2-x}S + SnS_2 \rightarrow Cu_2SnS_3 + Cu_{2-x}S$ (4.9)

From the resulting binary and ternary sulfides, only Cu_2SnS_3 reacts in the second step with ZnS to form Cu_2ZnSnS_4. If there is an excess of ZnS, it will precipitate in the film with $Cu_{2-x}S$ as solid grains, as observed in our films. The reaction results in case of excess of Cu and Zn can be described by the following equation:

$Cu_{2-x}S + Cu_2SnS_3 + ZnS \rightarrow Cu_2ZnSnS_4 + Cu_{2-x}S + ZnS$ (4.10)

From Eq. 4.10, we can suppose that the evolution of $Cu_{2-x}S$ phases can be avoided by having a sufficient amount of Sn in the starting metal precursor or by providing extra Sn as vapor to the precursor during the sulfurization process.

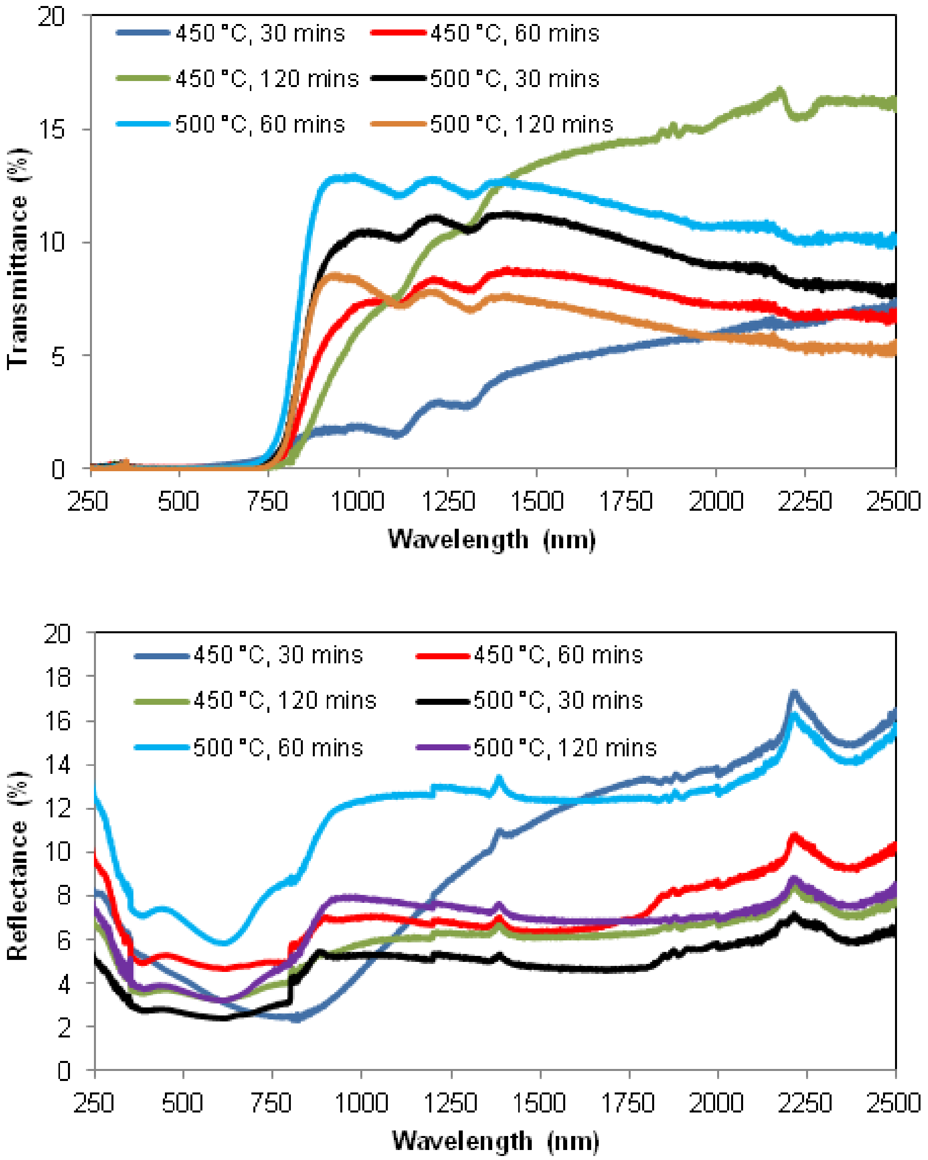

Figure 4.12 Transmittane and reflectance spectra of the CZTS films annealed at 450 °C and 500 °C.

4.2.3.5 Optical properties

Using the same sputtering and sulfurization conditions, new CZTS films were deposited on SLG substrates to conduct the reflectance and transmittance measurements. Figure 4.12 shows the optical reflectance and transmittance spectra of the CZTS films annealed at 450 °C and 500 °C. The absorption spectra of these films were calculated from the measured reflection and transmission using the relation:

$A = 1 - (R + T)$ (4.11)

where A is absorption, R is reflection, and T is transmission. Figure 4.13 shows the optical absorption spectra of the CZTS films sulfurized at 450 °C and 500 °C for 30, 60, and 120 minutes. Generally, all films show that more than 90% of the incident light is absorbed in the visible range, indicating a large absorption coefficient and sufficient film thickness. The absorption coefficient α was calculated with an estimated thickness of 2.5 µm for all films. The value of the absorption coefficient in the visible range obtained for all films was larger than 10^4 cm^{-1}.

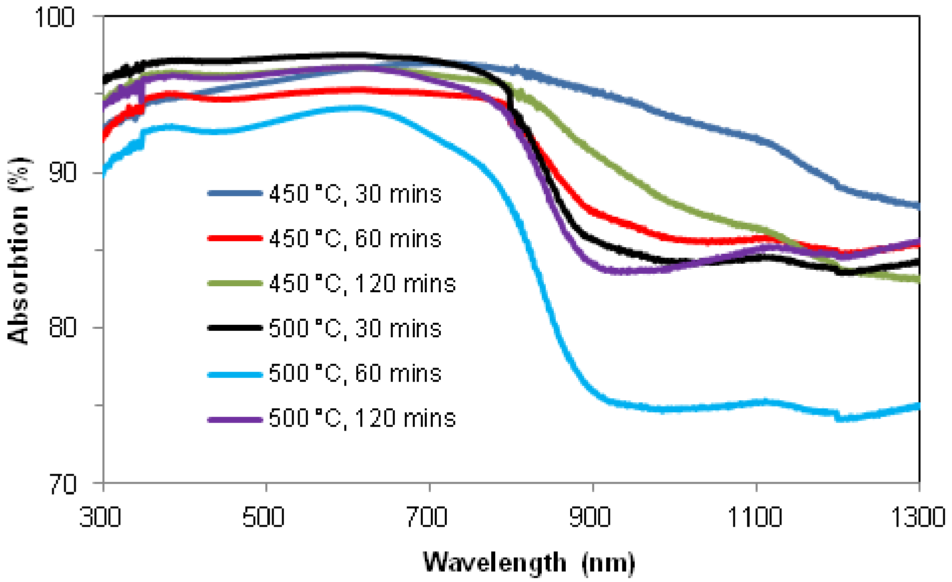

Figure 4.13 Absorption spectra of the CZTS films sulfurized at 450 °C and 500 °C for 30, 60, and 120 minutes.

The optical bandgap energies of the CZTS films were calculated using the following relation:

$\alpha hv = A(hv - E_g)^n$ (4.12)

where α is the absorption coefficient, A is constant, *hv* is the photon energy, *Eg* is the bandgap energy, and *n* is a constant that takes the value 1/2 for direct transitions.

The plot of $(\alpha h\nu)^2$ versus $h\nu$ for all CZTS films annealed at various conditions is illustrated in Figure 3.14. We obtain the optical bandgap by extrapolating the linear region of the curves to the $h\nu$ axis. For the films annealed at 450 °C for 30, 60, and 120 min, the estimated optical bandgaps were 1.33, 1.47, and 1.42 eV, respectively. The narrow bandgap of the film annealed at 450 °C for 30 min can be explained by the presence of Cu_2SnS_3 and $Cu_{2-x}S$ phases, with their smaller bandgaps of 0.93−1.35 eV for Cu_2SnS_3 and 1.21 eV [223] for Cu_2S leading to the lowered bandgap of the films. Although the presence of these phases was detected in other films, XRD showed that they have a high concentration in film A compared to their existence in the other films. The estimated bandgap energy for films sulfurized at 500 °C and 550 °C for 30, 60, and 120 min were 1.49, 1.52, 1.5, 1.5, 1.49, and 1.51, respectively. The bandgap energies of these films are in agreement with the reported values for CZTS.

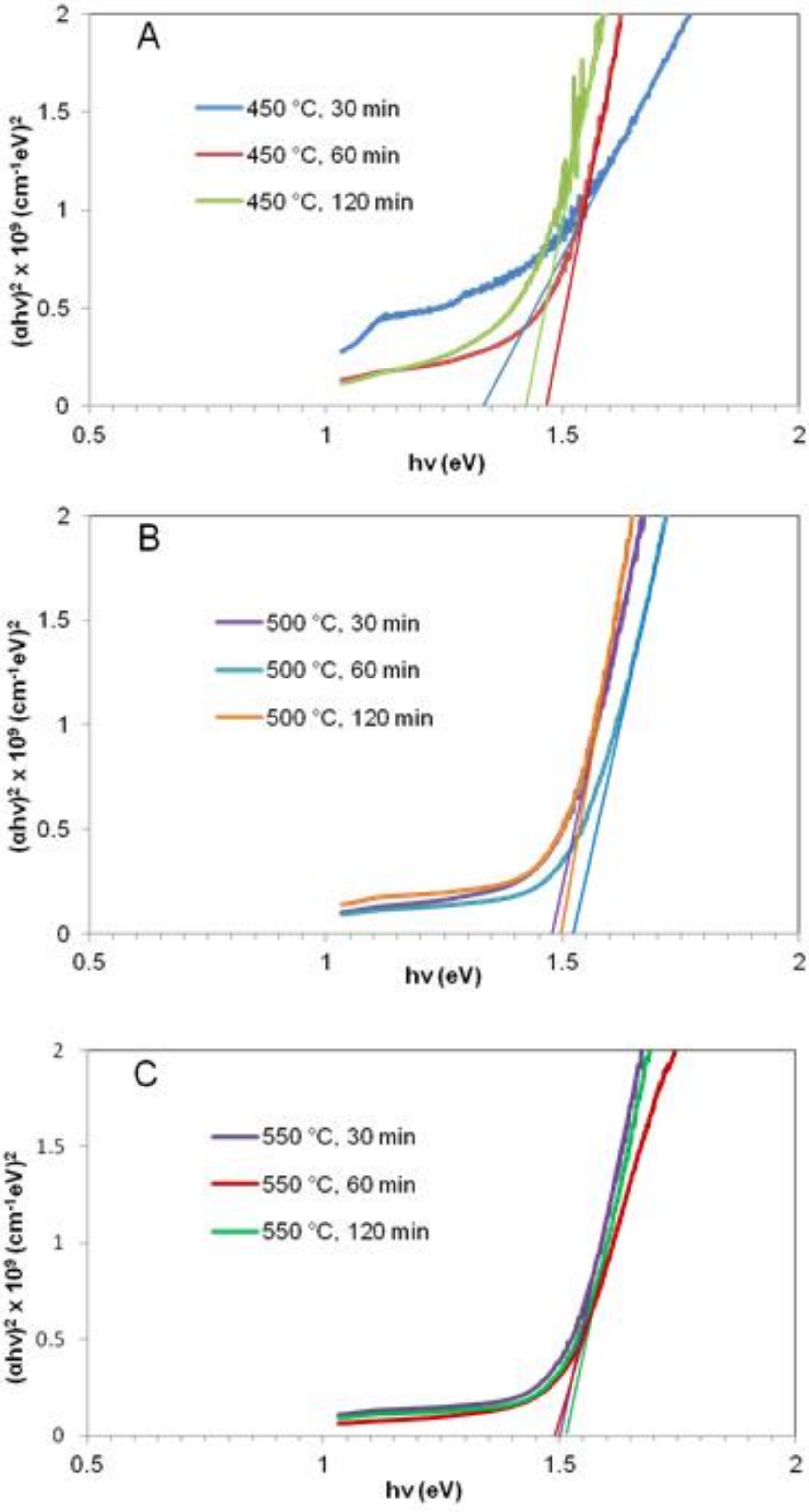

Figure 4.14: Plot of $(ahv)^2$ versus hv to estimate the bandgap for the CZTS films sulfurized under different conditions [141].

4.2.3.6 Compositional analysis by Auger electron spectroscopy (AES)

AES depth profiling of selected samples was conducted to reveal the chemical composition of the films at the surface and in the bulk. Figure 4.15 shows AES depth profiles of the films annealed at 450, 500, and 550 °C for 30, 120, and 60 min, respectively.

For the film annealed at 450 °C for 30 min, the analysis shows a Cu-rich layer at the surface. This could be explained by the copper sulfide grains that were distributed on the surface and revealed by SEM. The deficiency of sulfur throughout the entire depth profile clearly indicates incomplete sulfur incorporation, and hence, that the sulfurization process was not completed. The oxygen detected in the bulk and at the back explains the presence of voids at the Mo/film interface; it could also indicate some oxides.

AES depth profiling analysis of the film annealed at 500 °C for 120 min revealed a slight Sn-rich layer at the surface and a high amount of Zn in the film bulk. As the figure shows, the film exhibits more compositional uniformity, which indicates enhanced interdiffusion of the elements. However, it exhibits a lack of sulfur. In contrast to the film sulfurized at 450 °C for 30 min, the analysis did not show any sign of oxygen in the bulk or at the back. The amount of oxygen detected at the surface could be explained by the film porosity at the surface.

For the film sulfurized at 550 °C for 60 min, the depth profiling shows greater incorporation of sulfur in the film; however, the film exhibits Cu deficiency and a very high amount of Zn. The SEM analysis showed clear segregation of $Cu_{2-x}S$ crystallites on the surface, and EDS revealed a high concentration of Zn and small amount of Cu at the regions without the $Cu_{2-x}S$ grains on the surface. Therefore, it is believed that the AES measurement occurred at a region not containing $Cu_{2-x}S$ crystallites.

The analyzed films also showed a high concentration of sulfur and molybdenum at the interface of the film and Mo layer, indicating the presence of a Mo_2S phase.

4.2.4 Conclusion

In this study, CZTS films were prepared by annealing slightly Cu-poor and Zn-rich Cu/Sn/ Zn/Mo stacked metal precursors in sulfur atmosphere. The precursors were sulfurized under different conditions to optimize our process and to investigate the effect of annealing parameters on film properties. Relatively uniform distribution of the copper, zinc, and tin metal layers over the entire substrate was observed. The discrepancies and variation in the chemical composition were explained by the nonuniform distribution of the Cu-S grains on the film surface so that some film areas would show high Cu concentration, and consequently, low amount of Zn and Sn, whereas other regions would exhibit a low amount of Cu and high Zn and Sn concentration. Analyzing the compositional, structural, morphological, and optical data showed that the films annealed at 500 °C and 550 °C showed better crystallinity, dense structures, and energy bandgaps close to the optimal value of 1.5 eV. The segregation of $Cu_{2-x}S$ crystallites on the film surface was attributed to an insufficient amount of Sn, and a route to avoid their evolution was suggested. Based on the results, most of the annealed films in our study are treated at temperatures between 500 °C and 550 °C. In some cases, substrate temperatures of up to 600 °C were applied.

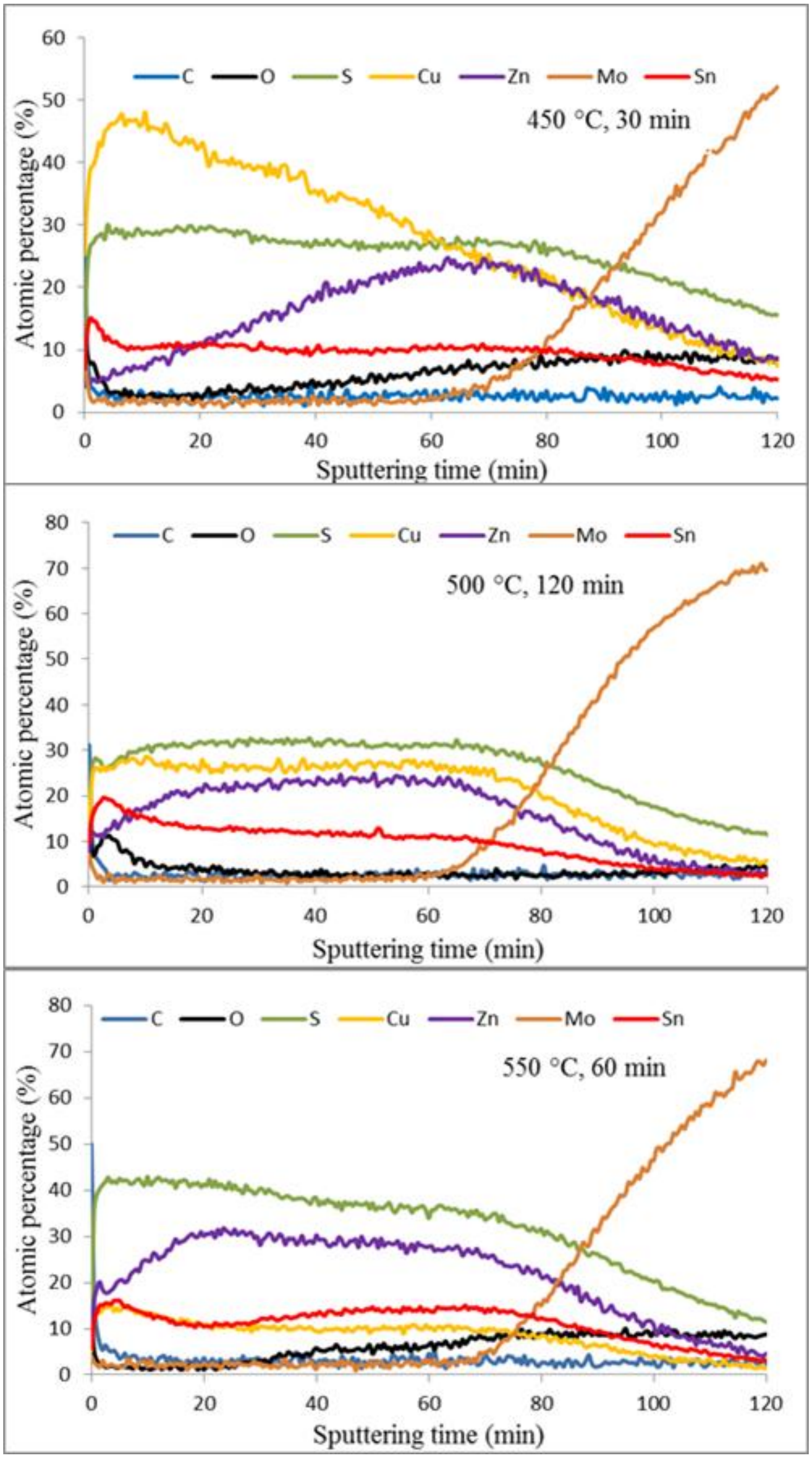

Figure 4.15: AES depth profiling of the films annealed at 450, 500, and 550 °C for 30, 120, and 60 min, respectively.

4.3 Role of the precursor thickness

One thought stemming from the results in Sec. 4.2 was the reduction of the precursor thickness to facilitate the diffusion of metals during the annealing process. The idea is that the migration of Zn to the film surface and Cu to the bottom is more efficient in terms of completing the reaction to form the CZTS phase and to reduce the development of secondary phases.

To pursue this idea, a new metal precursor was sputtered on Mo-coated SLG substrate with the same stack sequence Mo/Zn/Sn/Cu. The elemental composition of the metal precursor was close to the ones used in the previous experiment set. The chemical composition from XRF was 49.8%, 26.3%, and 23.9% for Cu, Zn, and Sn, respectively, showing a slight Zn-rich and Sn-poor concentration. Cu, on the other hand, shows a stoichiometric value. The average of the measured thickness of the metal film before sulfurization was about 310 nm, which is less than a third of the precursors used previously.

In the following step, the thin metal film was the heated in sulfur atmosphere at a temperature of 530 °C, between 500 °C and 550 °C, for 60 min. All other parameters, such as the heating rate, carrier gas, and sulfur vapor pressure, remained the same. After the treatment, a thickness of about 800 nm was measured. The thin CZTS absorber layer was then characterized by XRD, SEM, and EDS.

Figure 4.16 shows the XRD spectrum of the sulfurized 310-nm-thick precursor. The XRD diffraction peaks correspond to kesterite CZTS, excluding the peaks at $2\theta =$ 29.30° and 31.85°, which were assigned to $Cu_{2-x}S$ phases. Similarly, the pattern of this film shows the suppression of secondary-phase peaks observed in the previously prepared thicker films at the diffraction angle 2θ of 26.6° and 33.9°. The peaks also showed low intensities due to the thinner film thickness. The sharp CZTS peaks indicate good film crystallinity.

Figure 4.17 illustrates plan-view SEM micrographs of the thin CZTS film. As micrograph A shows, the film displays dark spots with segregated crystallites on the surface. These crystallites were identified by EDS as $Cu_{2-x}S$ grains. EDS also showed an S/metal ratio of 1.1, demonstrating the completion of the sulfurization process. The Cu/Zn+Sn and Zn/Sn ratios were 1.0 and 1.4, respectively, indicating a stoichiometric value for Cu and some deficiency of Sn. Comparing the precursor Zn/Sn ratio of 1.1 and the CZTS film Zn/Sn ratio of 1.4 indicates the loss of Sn during the sulfurization process. No other phases in addition to Cu_2ZnSnS_4 and $Cu_{2-x}S$ could be detected using XRD and EDS.

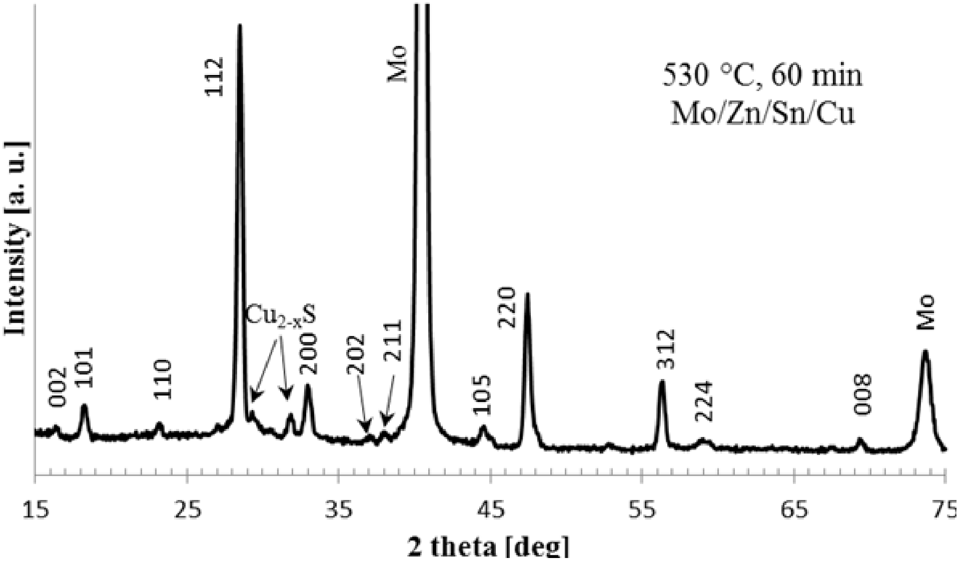

Figure 4.16: XRD spectrum of the sulfurized 310-nm-thick precursor [141].

Further, micrographs B and C exhibit the morphology of two different areas with and without $Cu_{2-x}S$ grains. Both regions show compact morphology with well-defined and densely packed fine CZTS grains.

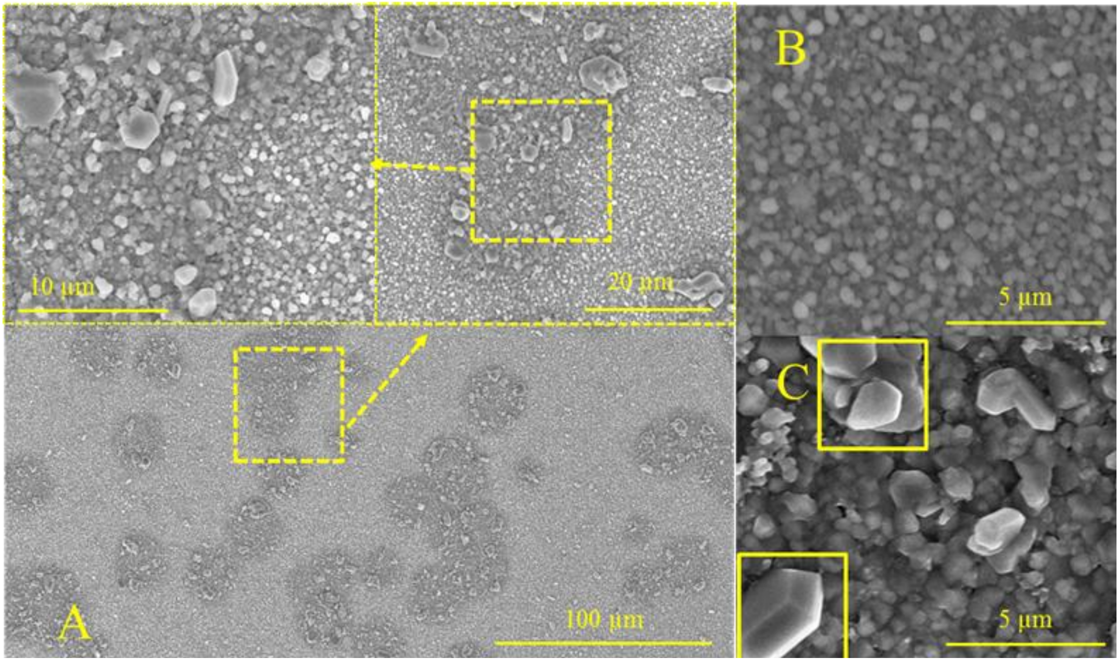

Figure 4.17: Plan-view SEM micrographs of 800-nm-thin CZTS film. Cu2-xS crystallites are marked with squares [141].

Clearly, the reduction of the precursor thickness results in minimizing the secondary phases and the $Cu_{2-x}S$ crystallites accumulated on the film surface. However, $Cu_{2-x}S$ are still present and represent a serious problem regarding the use of the film as an active layer in the device. The high concentration of copper in the starting precursor (about 50%) and consequently in the final CZTS film suggests the fabrication of CZTS film based on Cu-poor precursors to avoid developing $Cu_{2-x}S$.

4.4 Dependence of secondary phases on the film chemical composition

The results from this section were published in: M. Abusnina, M. Matin, H. R. Moutinho, J. L. Blackburn, J. Alleman, C. DeHart, B. To, and M. Al-Jassim, “Suppression of the $Cu_{2-x}S$ Secondary Phases in CZTS Films through Controlling the Film Elemental Composition,” *IEEE Journal of Photovoltaics*, vol. 5, no. 5, 2015.

4.4.1 Introduction

As stated Chapter 2, secondary phases can be very detrimental to the solar cell and avoiding them is very desirable to obtain good-quality absorber layers. The existence of secondary phases in the compound depends on the composition of the precursor. However, it is also affected by the sulfurization process where, for instance, the loss of Sn or Zn could lead to the evolution of $Cu_{2-x}S$ phases. Tanaka *et al.* [46] reported on the evaporation of Zn at a substrate temperature above 450 °C and suggested using ZnS targets instead of elemental Zn to reduce its evaporation. Sn loss during the annealing process has also been widely reported in the literature [46], [221], [224].

From the results achieved in Section 4.2, we concluded that the presence of $Cu_{2-x}S$ secondary phases in the form of relatively large crystallites segregated on the surface of our films is due to a high Cu concentration in the metal precursors and/or to an insufficient amount of Sn. Yoo *et al.* [142] reported that the separation of $Cu_{2-x}S$ phases in CZTS films is due to the sulfurization of Cu-rich metal precursors. Weber *et al.* [221] have reported on the decomposition of Cu_2ZnSnS_4 at temperatures above 350 °C, and as a consequence, SnS evaporates from the compound leaving copper sulfides and zinc sulfides as solid phases in the film.

The main goal of this study was intended to fabricate $Cu_{2-x}S$-free CZTS films by lowering the amount of Cu in the metal precursor and to investigate the impact of the amount of Cu on the film properties. Additionally, we wanted to study the influence of the chemical composition, in general, on the structural and morphological properties of the kesterite CZTS compound.

4.4.2 Experimental

The metal precursors were sequentially deposited on Mo-Co SLG substrates with the stack order Mo/Zn/Sn/Cu after the procedure described in Chapter 3. The composition of the metal precursors was controlled by varying the sputtering power of each element to realize metal films with a wide range of composition. The precursors were then annealed in sulfur ambient at 540 °C for 60 min under the flow of N_2. After sulfurization, the chemical composition of the final CZTS films was determined using EPMA. Investigation of the surface and cross-sectional morphology of the sulfurized films was carried out by SEM. XRD and Raman scattering spectroscopy were used to identify the crystallographic phase of the prepared films. EDS was employed as a complementary tool to identify secondary phases. Electron back-scattered diffraction (EBSD) was used to estimate grain size and reveal grain orientation. Prior to conducting EBSD measurements, the surface of the films was ion-milled using a cross-sectional polisher (JEOL, 1B-09010CP).

4.4.3 Results and discussions

4.4.3.1 Study of the chemical composition

In this study, a total of eight films with different composition were prepared; however, only six of them will be presented because the other two showed values close to two of the films presented here. The composition data of the CZTS films from EPMA are listed in Table 4.11, starting with films with higher Cu/(Zn+Sn) ratios and going to films exhibiting lower Cu/(Zn+Sn) ratios. In addition to investigating the role of the amount of Cu in developing $Cu_{2-x}S$ phases, we wanted to study the impact of both Zn and Sn concentration in the film on the evolution of these phases. For that, the Zn/Sn ratio was varied to produce films with diverse Zn/Cu and Sn/Cu ratios.

Table 4.11: Chemical composition from EPMA data of sulfurized CZTS films with different Cu concentration [225].

Film	Cu (%)	Zn (%)	Sn (%)	S (%)	S/metals	Cu/(Zn+Sn)	Zn/Cu	Sn/Cu	Zn/Sn
133	25.95	13.35	11.35	49.35	0.97	1.05	0.52	0.44	1.18
141	24.82	12.16	11.98	51.04	1.04	1.03	0.49	0.48	1.02
137	24.60	11.92	13.65	49.83	0.99	0.96	0.48	0.55	0.87
142	22.88	12.88	13.47	50.77	1.03	0.87	0.56	0.59	0.96
139	22.52	12.67	13.67	51.64	1.07	0.85	0.56	0.61	0.93
134	22.55	16.21	11.68	49.56	0.98	0.81	0.72	0.52	1.39

As the table shows, the sulfur-to-metals ratio exhibits a nearly stoichiometric value, indicating the completion of the sulfurization process. The first three samples in the table—S133, S141, and S137—exhibit a nearly stoichiometric Cu/(Zn + Sn) ratio; however, the Zn/Sn ratio experienced some decrease due to the decrease of the amount of Zn and the increase of Sn concentration. Sn amount was deliberately increased to follow the thought developed in Section 4.2 that a sufficient amount of Sn could lead to suppressing $Cu_{2-x}S$ phases. For S142, S139, and S134, the Cu content was kept nearly constant realizing Cu-poor films, whereas Sn/Cu and Zn/Cu ratios were varied. Film S134 was realized with an excess of Zn and deficiency of Cu and Sn to check the possibility of $Cu_{2-x}S$ evolution in a Cu-poor and Sn-poor composition.

4.4.3.2 Effect of the composition on the film crystallographic structure

The composition of the sulfurized CZTS films is represented in the ternary phase diagram (Figure 4.18) introduced in Chapter 2 to illustrate the secondary phases expected in each sample. For sample 133, which is Cu-rich and Zn-rich, Cu_2S and ZnS phases are expected. The stoichiometric sample (141) lies in the single-phase stable region and is expected to exhibit single-phase kesterite, whereas the Zn-poor and Sn-rich sample (137) is expected to form the ternary Cu_2SnS_3 and quaternary $Cu_2ZnSn_3S_8$ phases in addition to CZTS. ZnS would form in the Zn-rich films (134, 139, and 142), and additionally, $Cu_2ZnSn_3S_8$ is expected to form in the Sn-rich films (139 and 142).

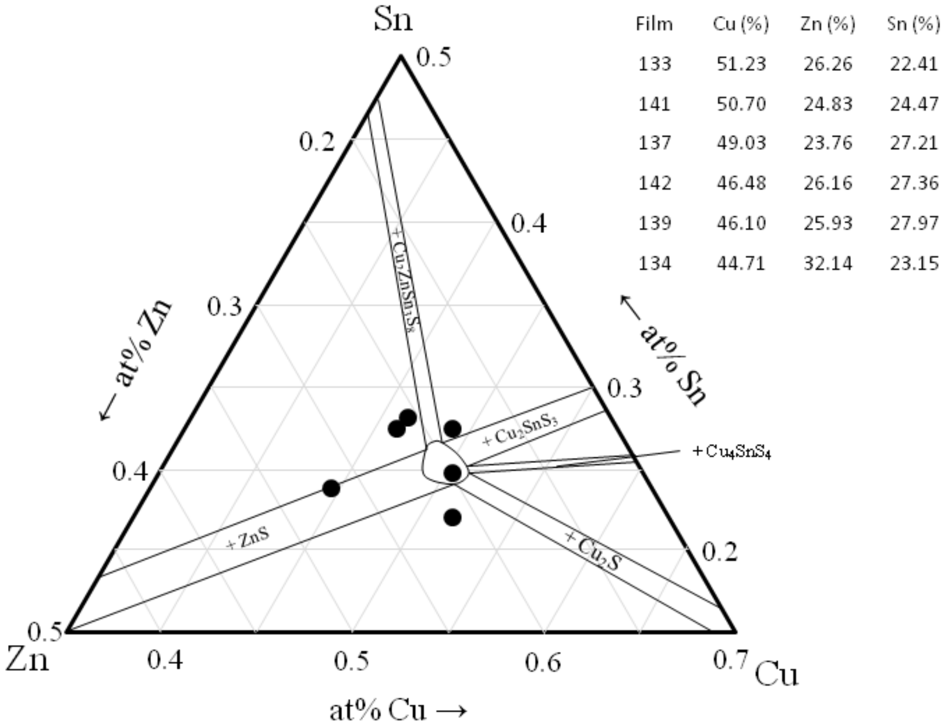

Film	Cu (%)	Zn (%)	Sn (%)
133	51.23	26.26	22.41
141	50.70	24.83	24.47
137	49.03	23.76	27.21
142	46.48	26.16	27.36
139	46.10	25.93	27.97
134	44.71	32.14	23.15

Figure 4.18: Composition of sulfurized CZTS films with different Cu concentration acquired using EPMA.

XRD spectra of the six samples are shown in Figure 4.19. The spectra are displayed in a diffraction angle range from 15° to 75°. Additionally, enlarged regions of 2θ in the ranges 27°–35° and 51°–61° are shown to visualize the small peaks in these ranges. The patterns of all films show a crystal structure of polycrystalline kesterite CZTS according to the powder diffraction file (PDF) # 00-026-0575. CuS phase (PDF# 01-079-2321), marked with "•" on the graphs, was, as expected, detected in the slightly Cu-rich films (133), but was also observed in the nearly stoichiometric sample (141). The Cu/(Zn+Sn) ratio of sample 141exhibits very little deviation of the stoichiometric value of 1, so the film could also be considered as slightly Cu-rich. This shows how narrow is the stability of the single-phase region. The patterns also exhibit good crystallization of the compound in the form of sharp peaks. On the pattern of sample 133, some broadness caused by the CuS peak located at the diffraction angle of 59.45°can be seen in the (224) peak at 58.84°. As predicted in the phase diagram, $Cu_{2-x}S$ phases could not be identified in the other Zn-rich and Sn-rich samples. As mentioned in Chapter 2, the predictable ZnS and Cu_2SnS_3 phases anticipated in the Zn-rich and Sn-rich films cannot be detected with XRD because they have peaks at the same positions as those of CZTS. Some preferential orientation in the (112) plane could be assumed when comparing the intensity ratio of the main CZTS peaks with values from the JCPDS cards.

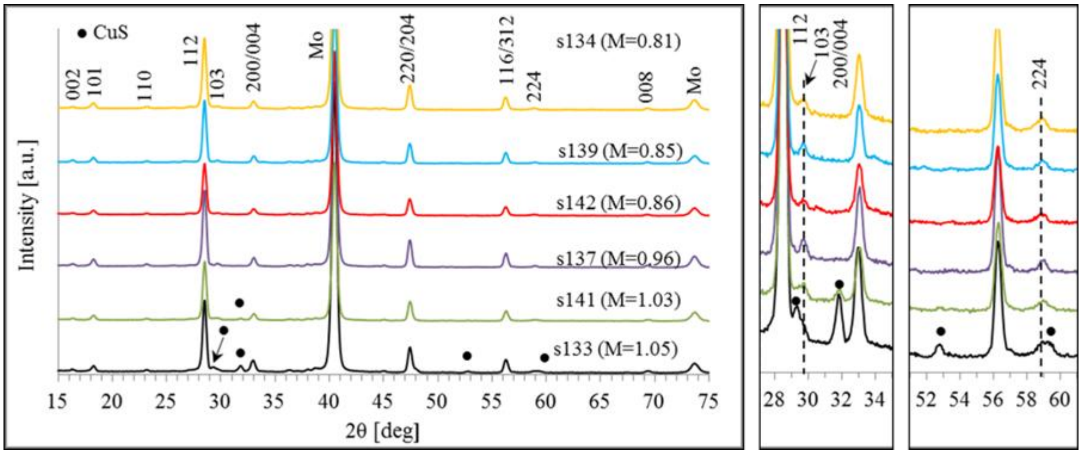

Figure 4.19: X-ray diffraction spectra of CZTS films with different Cu/(Zn+Sn) ratio [225].

Figure 4.20 shows the Raman scattering spectra of the CZTS films with various Cu/(Zn+Sn). In good agreement with the literature, all film spectra demonstrate the most intense CZTS peaks located at 288 and 338 cm^{-1}, except for the pattern of film 139, which only shows the main CZTS peak at 338 cm^{-1}. Confirming the XRD results, the patterns of the slightly Cu-rich films 133 and 141 show the presence of the $Cu_{2-x}S$ phases with their peak at 475 cm^{-1}. The comparison of the peak intensities of both films implies the reduction of $Cu_{2-x}S$ phases in film 144, although their Cu/(Zn+Sn) ratios represent nearly the same value. In addition to the main peaks, CZTS exhibits in some cases, as reported in [76], [122], a shoulder at 351 cm^{-1} and a broad peak between 368 cm^{-1} and 373 cm^{-1}. This can be seen in the patterns of films 141, 142, 139, and 134. However, this peak expands to 377 cm^{-1} on the pattern of film 139. As anticipated, in Zn-rich films, the cubic ZnS phase with its main peak at 352 cm^{-1} could not be distinguished from CZTS using a laser source with an excitation wavelengths in the visible region of 488 nm. Similarly, no clear signs of the presence of the Cu_2SnS_3 phase were seen on the Raman spectra of the Sn-rich films.

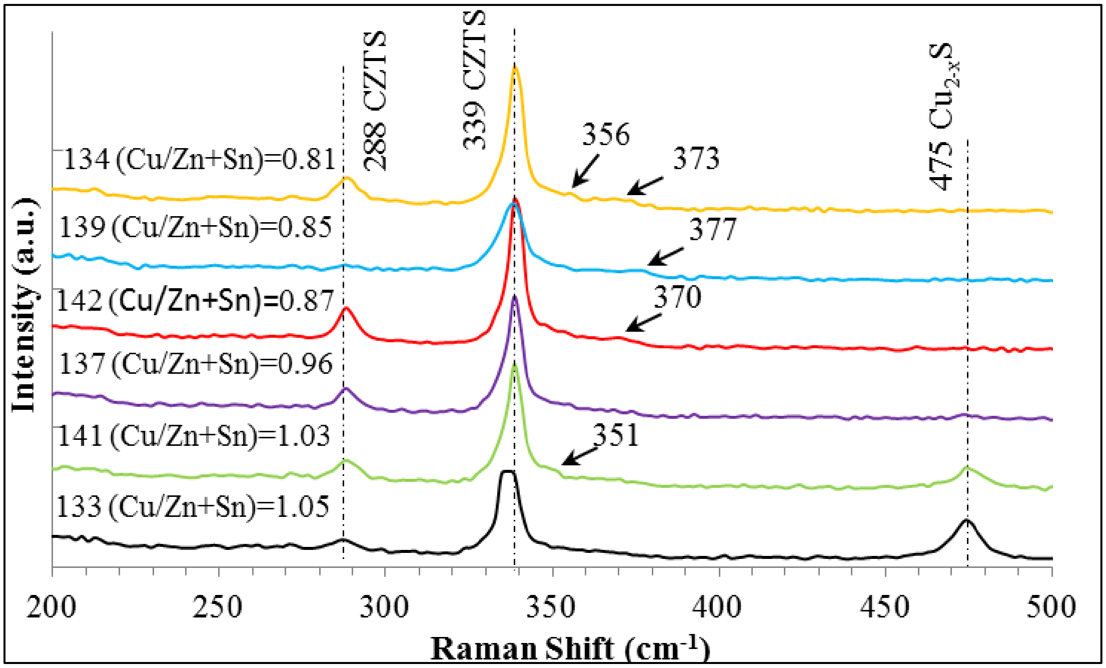

Figure 4.20: Raman scattering spectra of CZTS films with different Cu/(Zn+Sn) ratio [225].

4.4.3.3 Effect of the composition on the film morphology and micro structure

Plan-view and cross-sectional (inset) SEM micrographs of the CZTS films with different chemical compositions are shown in Figure 4.21. Both Cu-rich films with Cu/(Zn + Sn) ratio higher than unity exhibit features of large grains segregated on the surface and are marked with circles in the micrographs. EDS identified these grains as

$Cu_{2-x}S$, confirming the results from XRD and Raman scattering spectroscopy. Furthermore, surface morphology revealed that film 133 has, in average, large grains whereas film 141 exhibits dense structure. The slight difference in grain size could be related to the slight difference in the amount of Cu in both films. In the literature, two contradictory statements were made relating the grain size growth to the amount of copper in the film. For instance, the grain-size growth was enhanced when decreasing Cu content in films prepared using sol–gel sulfurization [226]. In contrast, grain-size increase was related to the increase of Cu amount in films produced using coevaporation [227]. Thus, detailed investigation is needed to clarify the discrepancy in relating the grain size to the copper concentration in CZTS films. The Zn-poor and Sn-rich film (137) exhibits grains with sizes that range from smaller than 0.5 μm to about 2 μm. On the other hand, the Zn-rich films (142, 139, and 134) with Cu/(Zn + Sn) ratios of 0.87, 0.85, and 0.82, respectively, show dense morphology with small CZTS grains. Notably, these films have less Cu than the films exhibiting larger grains, which could indicate enhancement of grain size under Cu-rich growth.

In addition to the development of $Cu_{2-x}S$ phases in the Cu-rich films, these phases were detected in some areas of the most Cu-poor film (134). Grains with a high concentration of Zn and S were also identified in this film, indicating the presence of ZnS phase (ZnS grains are marked with squares on the micrograph of film 134). Unlike the segregation of $Cu_{2-x}S$ phases, the existence of ZnS in this film was expected, as predicted from the phase diagram, because the film is considerably Zn-rich. ZnS grains were also found at the CZTS/Mo interface, and they appear in the SEM cross-sectional micrograph as brighter grains compared to the CZTS grains. For the Sn-rich films (137, 142, and 139) with Sn/Cu ratios of 0.55, 0.59, and 0.61, respectively, no signs of secondary phases were observed.

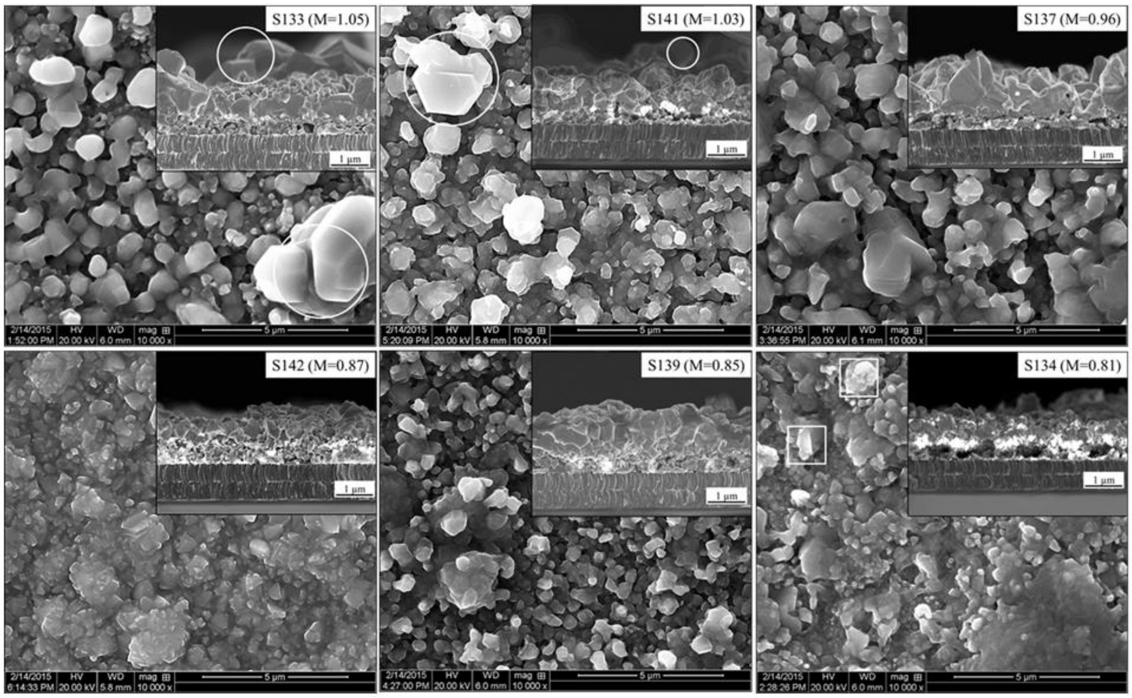

Figure 4.21: Plan-view and cross-sectional SEM micrographs of CZTS films with different Cu/(Zn+Sn) ratios [225].

To explain the development of $Cu_{2-x}S$ in the most Cu-poor film (134), we noted, as Table 4.11 shows, that the film Sn/Cu ratio of 0.52 is nearly stoichiometric. The second note is that the chemical composition from EPMA represents an average of measurements taken at five different regions. Generally, the composition values show minimal deviation. However, at one of the measured regions of film 134, the Sn/Cu ratio was about 0.45 and the Cu/(Zn+Sn) ratio was about 0.97. According to the assumption made based on the results from Section 4.2, we believe that the Sn deficiency in some regions led to the development of $Cu_{2-x}S$. Based on that, we can suggest a route to prepare $Cu_{2-x}S$-free CZTS films by incorporating a sufficient amount of Sn in the film during the growth process so that the Sn/Cu ratio is always higher than 0.5. Theoretically, a high amount of Sn will result in the presence of Sn-S phases or could even lead to the evolution of Cu_2SnS_3, which is harmful to the solar cell, just like the $Cu_{2-x}S$ phases. The development of Cu_2SnS_3 can be avoided by providing excess Zn in the metal precursor (Zn/Cu ratio higher than 0.5) so that Zn reacts with Cu_2SnS_3 to form CZTS. Clearly, too high a Zn concentration in the metal film causes the formation of a ZnS phase; therefore, the Zn content in the film needs to be enough to suppress the segregation of Cu_2SnS_3, and at the same time, to not lead to ZnS growth. If, on the other hand, Sn-S phases exist in the film, they might evaporate, especially when annealing for a long time. In the worst case, they are present in the compound as solid crystallites, but with no or less harm to the device compared to Cu_2SnS_3 or $Cu_{2-x}S$ phases.

Table 4.12: Compositional ratios of Cu-rich and Cu-poor CZTS films with Cu/(Zn+Sn) ratios of 1.2 and 0.66.

Film	S/metals	Cu/(Zn+Sn)	Zn/Cu	Sn/Cu	Zn/Sn
S226	1.00	1.12	0.35	0.55	0.63
S228	1.00	0.66	1.07	0.45	2.34

To finally prove that the evolution of $Cu_{2-x}S$ phases can be controlled by the Sn/Cu ratio rather than by the Cu/(Zn+Sn) ratio, we prepared two additional CZTS films (226 and 228) with different Cu/(Zn + Sn) and Sn/Cu ratios. Film 226 was Cu-rich and Sn-rich with a Cu/(Zn + Sn) ratio of 1.2 and Sn/Cu ratio of 0.55 as listed in Table 4.12, whereas film 228 was prepared as Cu-poor and Sn-poor with a Cu/(Zn + Sn) ratio of 0.66 and Sn/Cu ratio of 0.45.

Raman scattering spectroscopy and EDS were used to detect the presence of the $Cu_{2-x}S$ phases in the films. Figure 4.22 shows Raman spectra and top-view micrographs of the films. Both techniques showed the presence of $Cu_{2-x}S$ in the Cu-poor film, whereas they were suppressed in the Cu-rich film by ensuring a Sn/Cu ratio higher than 0.5.

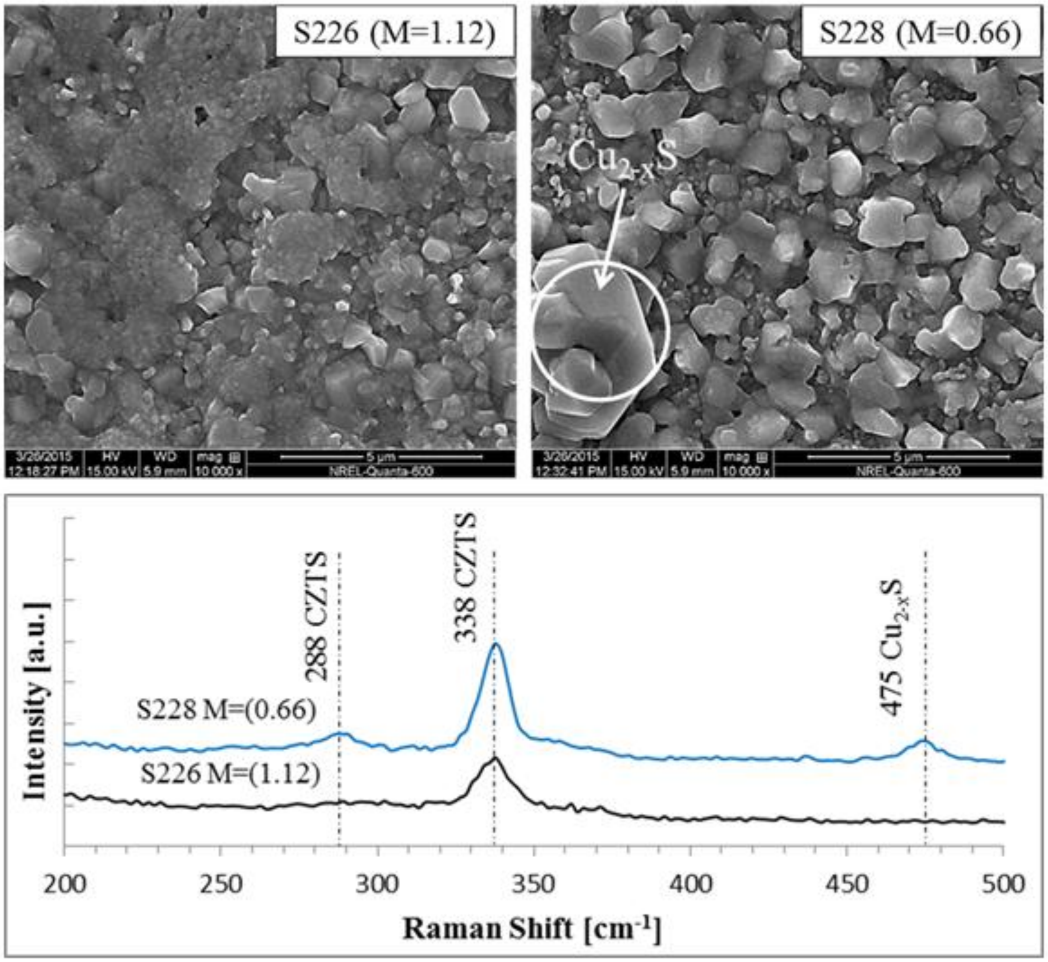

Figure 4.22: Plan-view SEM micrographs and Raman spectra of Cu-poor and Cu-rich CZTS films with Cu/(Zn + Sn) ratios of 0.66 and 1.12, showing the evolution and suppression of Cu2−xS phases in Cu-poor and Cu-rich composition by controlling the Sn/Cu ratio [225].

To gain more insight into the microstructure of the prepared CZTS films, two of the samples with no $Cu_{2-x}S$ segregation were analyzed with EBSD. The technique can provide data about film grain size, film texture, and local orientation distribution. Film 137 was chosen to be examined because it revealed a chemical composition close to stoichiometry and large CZTS grains, which is beneficial for the cell absorber layer to minimize the carrier recombination due to the grain-boundary defects. Film 139, on the other hand, was chosen because it exhibits dense morphology and to inspect the relationship between grain size growth and Cu content in the film. To reduce the surface roughness typically associated with films originating from stacked metal precursors, the films were ion-milled at 3 kV for 90 min.

Inverse-pole-figure (IPF) colored maps, showing grain boundaries and the local orientation of each grain, of the chosen CZTS films are displayed in Figures 4.23 (a) and (b). The maps also show some grain boundaries highlighted in green and blue. These satisfy the conditions for twin boundaries, and hence, the grains with these boundaries could be seen as twins. The figure also shows grain-color maps after removing the twin boundaries (Fig. 4.23 (c) and (d)) to judge the grain size in both films. Here, note that the color in these two maps is not associated with the grain orientation.

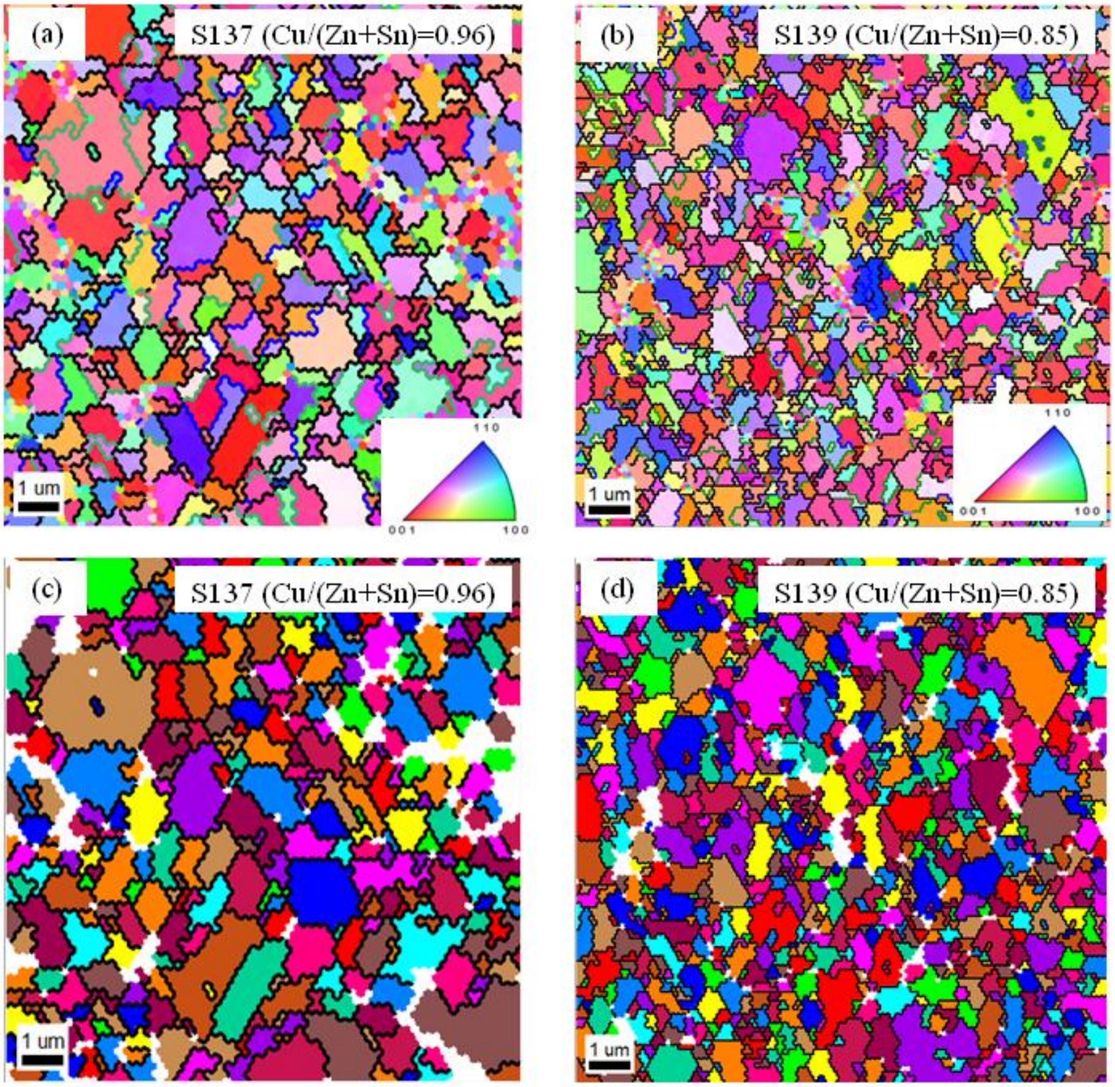

Figure 4.23: Surface normal-projected IPF orientation maps of sample S137 (a) and S139 (b), showing the grain boundaries and the local orientation of each grain, and grain color maps after removing the twin boundaries (c) and (d).

To obtain suitable grain size and orientation distribution, data from EBSD have to contain a large number of grains [228]. To investigate the possibility of crystal preferential orientation, EBSD data were collected at a different area of sample 137 with a large number of grains. The IPF colored maps and the orientation-distribution IPF of this area are illustrated in Figure 4.24. As can be seen, the orientation-distribution IPF shows a randomly oriented film with no preferential orientation, different than what we observed in the XRD spectra.

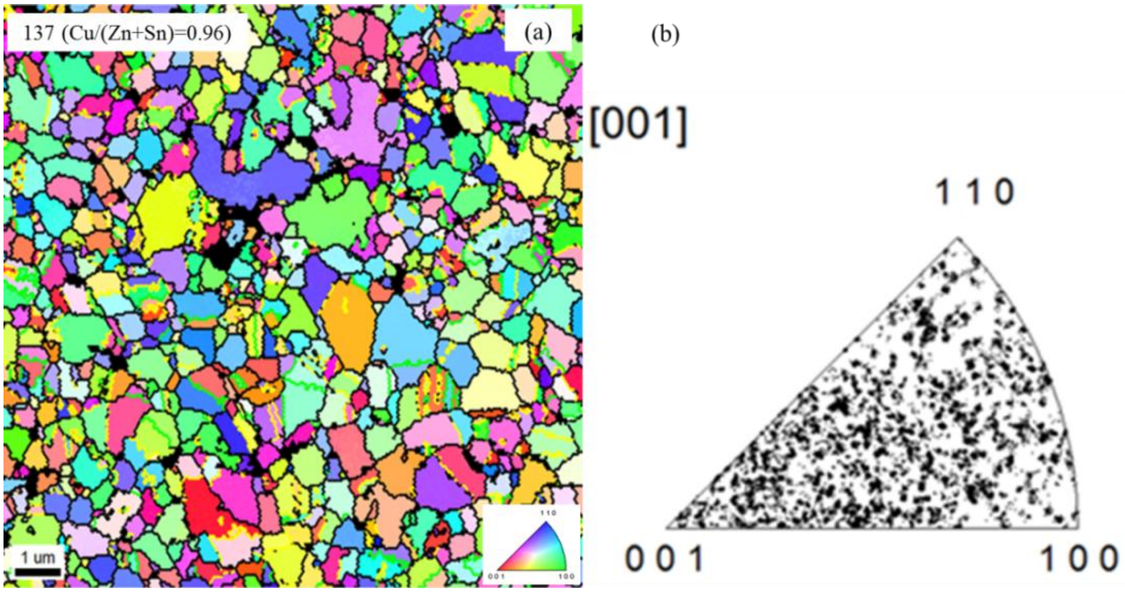

Figure 4.24: EBSD surface normal-projected colored IPF orientation map (a) and EBSD IPFs representing the orientation distribution (b) of sample 137 acquired at an area with a large number of grains.

The data-processing software installed on the system computer was used to calculate the grain-size statistic of both films. Based on the EBSD IPF maps illustrated in Figure 4.23, the grain-size distributions of the films are displayed in Figure 4.25.

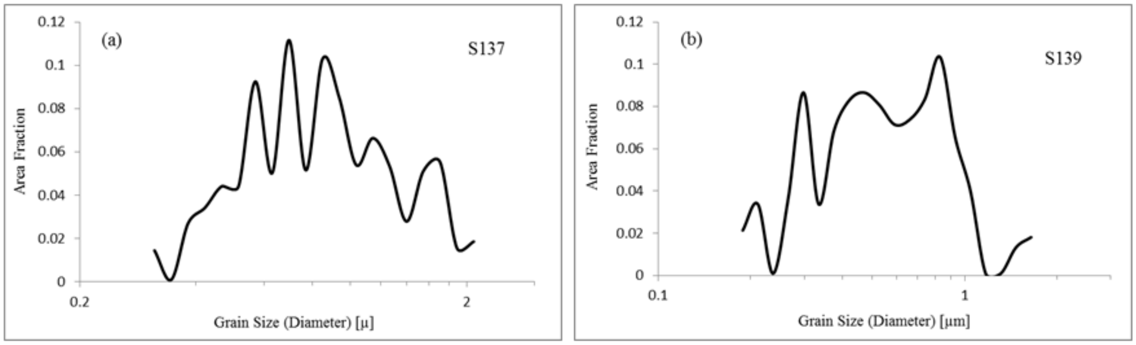

Figure 4.25: Grain-size distribution over the area shown in Fig. 4.23 for sample 137 (a) and sample 139 (b) calculated by the data-processing software.

From the graphs, about half the area of film 137 contains grains of about 0.85 μm to larger than 2 μm, whereas grains smaller than 0.85 μm are distributed over the other half of the area. Furthermore, no grains smaller than 0.31 μm were detected. The determined average grain size for film S137 is about 0.92 μm, which is considered a good size for the absorber layer. Film 139, on the other hand, exhibits grains of a size ranging from about 0.188 and 0.52 μm distributed over about 50% of the area where data were acquired, whereas the other half contains grains with a size between 0.52 and 1.6 μm. The determined average grain size of film 139 is about 0.59 μm. The EBSD grain-size analysis agrees with the observation made by comparing the films' morphology using SEM—that film 137 has an average grain size larger than the average grain size of film 139. Comparing the composition of both films, we could relate the enhanced grain-size growth to the increase in Cu content in the film, in good agreement with what was reported in [227], [229].

4.4.4 Conclusion

In this study, polycrystalline kesterite CZTS were fabricated by annealing metal precursors with a stack order of SLG/Mo/Zn/Sn/Cu in sulfur atmosphere at 540 °C for 60 min. The metal films were prepared to exhibit Cu-poor and Cu-rich composition, and additionally, Zn-rich and Sn-rich films were fabricated to investigate the impact of the composition on developing secondary phases in the final CZTS film and on the properties of the synthesized compound. Controlling the chemical concentration of the metal films was obtained by regulating the thickness of the layers. After sulfurization, the CZTS films showed Cu/(Zn + Sn) ratios ranging between 0.81 and 1.05. Films with different Sn concentration were also realized to inspect the possibility of suppressing $Cu_{2-x}S$ phases by providing an excess of Sn. EPMA data showed a S/metal ratio of 1, indicating that sulfurizing the precursors at 540 °C for 60 min is sufficient to complete the conversion of the metal films into CZTS.

As anticipated, the ZnS phase was identified in Zn-rich films; however, the result revealed that the Sn/Cu ratio is the controlling factor of the evolution of $Cu_{2-x}S$ phases, rather than the Cu/(Zn + Sn) ratio. Ensuring a Sn/Cu ratio greater than 0.5 led to avoiding the growth of $Cu_{2-x}S$ in Cu-rich films, whereas Sn/Cu ratio less than 0.5 led to their development in Cu-poor films..

EBSD orientation distribution measurements showed that the synthesized films are randomly oriented. Both SEM and EBSD revealed grain-size growth enhancement when a high amount of Cu was incorporated in the film.

4.5 Impact of the precursor stack order

The results from this study were, in part, presented in the IEEE PVSC and published in the conference proceeding as: M. Abusnina, M. Matin, H. Moutinho, and M. Al-Jassim, “Impact of the Stack Order in Cu-Zn-Sn Metal Precursors on the Properties of Cu_2ZnSnS_4 Thin Films,” IEEE PVSC, 2015.

The complete results were prepared for publication in the IEEE Journal of Photovoltaic as: M. Abusnina, M. Matin, H. Moutinho, and M. Al-Jassim, “Thin Film Solar Cells Based on CZTS Absorber Fabricated by the Sulfurization of Sputtered Metal Precursors with Different Stacking Orders,” IEEE Journal of Photovoltaic.

4.5.1 Introduction

Prior to our study, several published works reported on the influence of the stacking sequence in the metal precursor on the properties of CZTS thin films; however, most of them reported on only some of the total achievable stacking-sequence combinations that can be realized. In addition, the precursor chemical composition and the sulfurization conditions were not the same as the ones used in our work to conclude a general valid statement.

Araki *et al.* [230] reported preparing CZTS films by the sulfurization of electron-beam-evaporated metal precursors with six different stacking orders at 560 °C for 2 hours. They realized CZTS films with different compositions and reported that the highest conversion efficiency was observed in the cells with a stacking order where Cu and Sn were adjacent. The best PCE of 1.79% was obtained in cells having precursors with stacking order Mo/Zn/Cu/Sn. Shin *et al.* [120] prepared CZTS films by the sulfurization of sputtered precursors with three different stacking orders at 550 °C for 10 min in N_2/H_2S atmosphere. The realized stack orders were A: glass/ZnS/SnS_2/Cu, B: glass/SnS_2/Cu/ZnS, and C: glass/Cu/ZnS/SnS_2. They achieved single-phase kesterite films with dense morphology using stack order A, whereas secondary phases and voids were observed in the films based on stack orders B and C. Features of voids were also observed in CZTS prepared by the sulfurization of stacked metal films sputtered from elemental single targets. The existence of the voids in the films was justified by separating Cu and Sn by the Zn layer and by depositing Cu as the first layer in the stack [142]. Using two different stack sequences of Mo/Zn/Cu/Sn and Mo/Zn/Sn/Cu, Fernandes *et al.* [202] reported CZTS films with better crystal quality using Mo/Zn/Sn/Cu. Additionally, the Cu layer on top reduces the loss of Zn and Sn and allows better control of the chemical composition. From previous works, we can conclude the stacking order of the layers in the precursor has an impact on the chemical composition, film morphology, development of secondary phases, and material energy bandgap.

The stack sequences realized in our Cu-Zn-Sn metal precursors were A: Mo/Sn/Zn/Cu, B: Mo/Sn/Cu/Zn, C: Mo/Cu/Zn/Sn, D: Mo/Cu/Sn/Zn, E: Mo/Zn/Cu/Sn, and F: Mo/Zn/Sn/Cu, as illustrated in Figure 4.26. Throughout the text, the letters A–F refer primarily to the metal precursors, but also to the CZTS films and devices prepared based on the related precursors.

4.5.2 Experimental details

The metallic precursors were deposited with different stack orders of Cu, Zn, and Sn onto Mo-coated SLG substrates applying RF powers of 60, 35, and 32 W to the Cu, Zn, and Sn targets, respectively. The deposition time for each layer was fixed at 40 min. Thereafter, the metal precursors were converted into CZTS films by post-annealing at 540 °C for 60 min in sulfur atmosphere.

Chemical composition of the metal precursors and of the final CZTS films was carried out by XRF, whereas the structural characterization of the CZTS films and the phase identification were carried out using XRD and Raman scattering spectroscopy. An argon-ion laser operating at 488 nm was used as the excitation source in the Raman system. The surface and cross-section morphology of the sulfurized films was characterized by SEM. Energy-dispersive spectroscope was used to determine the elemental compositions of the final CZTS films, especially the sulfur/metal ratio. Furthermore, EDS is used to complement XRD and Raman measurements for identifying secondary phases. EDS measurements were performed at 15 kV. Atomic force microscopy measurements were conducted to investigate the effect of precursor stacking order on surface roughness of the CZTS films. The EBSD method was used to determine average grain size.

Solar cells based on the precursors with different stacking order were produced by the procedure described in Chapter 3. Current density-voltage (J-V) characteristics and external quantum efficiency (EQE) of the cells were then measured. Device J-V characteristics were measured under standard test conditions (AM1.5, 1000 W/m^2).

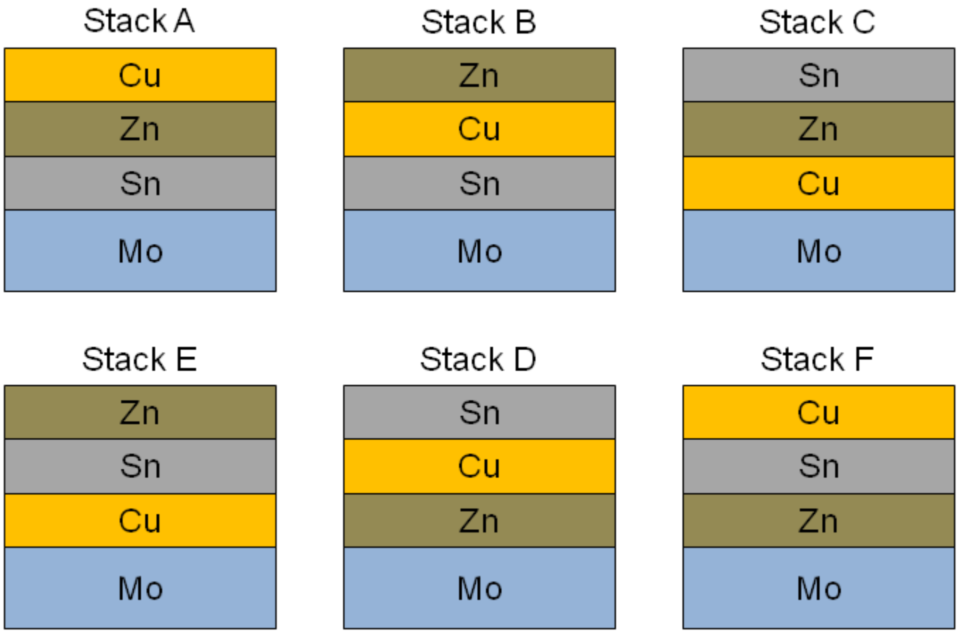

Figure 4.26: Six precursor stacking orders used in our study.

4.5.3 Results and discussion

4.5.3.1 Chemical composition study

The compositional data from XRF for the metal precursors and CZTS films with different stack orders are listed in Table 4.13. Data show that all precursors have Cu-poor, Zn-rich, and Sn-rich composition with minimal percentage deviation depending on the stacking order. Cu and Sn concentration experienced a small decrease in the precursor when sputtered directly onto the Mo layer. This observation could be explained by the dependence of the sticking coefficient of the different elements on the surface coverage. In contrast, there is only a minor variation in Zn amount in all precursors, indicating very little or no dependency of the Zn sticking coefficient on the surface coverage (Mo, Cu, or Sn). For Sn, enhanced growth is noticed when sputtered on Cu or Zn. After sulfurizing the precursors, Sn loss was generally observed in all films. However, annealed films with the Cu layer on the Sn layer—whether deposited directly on Sn or indirectly on the Zn/Sn layer—exhibited less Sn loss, indicating that the Cu layer deposited on top of Sn reduces the loss of Sn, as reported in [202].

Table 4.13: Chemical composition of the metal precursors and sulfurized CZTS films with different stacking sequences from XRF.

Sequence	**Before sulfurization**			**After sulfurization**		
	Cu (%)	Zn (%)	Sn (%)	Cu (%)	Zn (%)	Sn (%)
A: Mo/Sn/Zn/Cu	42.6	31.1	26.3	43.3	32.1	24.6
B: Mo/Sn/Cu/Zn	41.5	31.8	26.7	43.8	32.4	23.8
C: Mo/Cu/Zn/Sn	39.6	31.8	28.6	42.5	33.9	23.6
D: Mo/Cu/Sn/Zn	40.5	30.4	29.1	43.6	32.1	24.3
E: Mo/Zn/Cu/Sn	40.7	30.2	29.1	43.4	32.9	23.7
F: Mo/Zn/Sn/Cu	40.5	31.4	28.1	42.0	33.7	24.3

To better illustrate the change in composition after sulfurization, the metal concentration of precursor and CZTS films is represented in the ternary phase diagram (Figure 4.27). The composition of the samples before sulfurization is shown by black dots and after sulfurization by red dots. As can be seen, the initial composition was Cu-poor, Zn-rich, and slightly Sn-rich. Due to the Sn loss during annealing, the composition experienced a slight shift toward the Zn-rich and Cu-rich region. Due to the high concentration of Zn in all CZTS films, the ZnS phase is expected to develop in all CZTS films.

The chemical composition of the sulfurized CZTS films was also determined by EDS. The composition data are listed in Table 4.14. For all films, a S/metal ratio of about 1 was obtained, providing a good indication of completing the sulfurization process. Like XRF, EDS exhibited Zn-rich and Cu-poor composition with Cu/(Zn+Sn) ratios similar to those from XRF. Even the Zn/Sn ratios showed similar values to the ratios determined by

XRF, except for film A, which showed a high lower value. This could be due to nonuniformity of the composition in this film.

Table 4.14: Chemical composition of the sulfurized CZTS films with different stacking sequences from EDS.

Sequence	Cu (%)	Zn (%)	Sn (%)	S (%)	S/metals	Cu/(Zn+Sn)	Zn/Sn
A: Mo/Sn/Zn/Cu	20.05	15.04	13.51	51.40	1.06	0.70	1.11
B: Mo/Sn/Cu/Zn	20.09	15.99	11.57	50.35	1.01	0.73	1.38
C: Mo/Cu/Zn/Sn	20.08	15.66	11.78	52.39	1.10	0.73	1.33
D: Mo/Cu/Sn/Zn	19.68	17.10	10.71	52.52	1.11	0.71	1.68
E: Mo/Zn/Cu/Sn	20.26	15.46	11.57	52.71	1.11	0.75	1.34
F: Mo/Zn/Sn/Cu	20.28	15.46	12.29	51.97	1.08	0.73	1.26

4.5.3.2 Study of the crystallographic structure

XRD spectra of the CZTS films originated from metal precursors having different stacking sequences are shown in Figure 4.28. The diffraction peaks of all films correspond with kesterite CZTS crystal structure according to the powder diffraction file (PDF) # 26-0575. The diffraction patterns show some preferential orientation in the (112) plane and no clear trend was observed relating the different precursor stack orders to the films' crystallinity or texture. XRD also did not show any signs of secondary phases in addition to CZTS, which is different from what was reported in [120] that secondary phases evolve in CZTS depending on the precursor stack order used to prepare the film. Here, note that the chemical composition of the CZTS films reported in [120] shows a high concentration of Cu, and the Cu/Sn ratio of the studied films was greater than 2. These metal ratios will lead to the evolution of $Cu_{2-x}S$ phases independently of the precursor stack order [225].

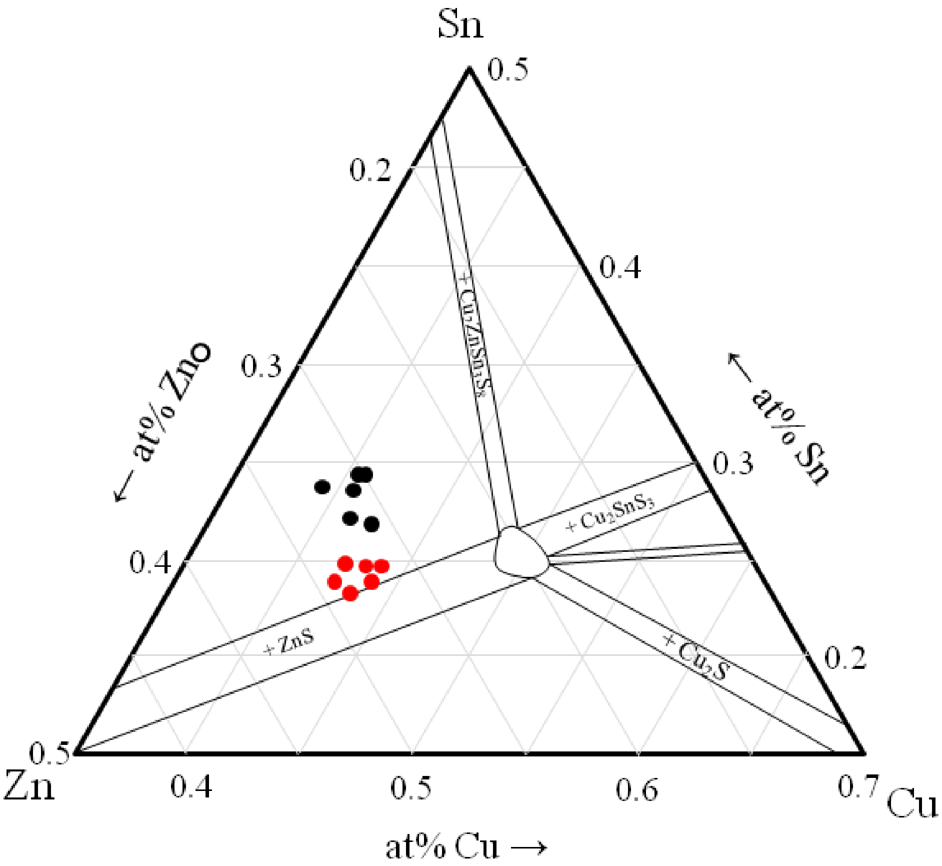

Figure 4.27: Composition of metal precursors having various stack orders (black dots) and of CZTS films prepared from these precursors (red dots).

Raman scattering measurements were conducted to reveal the existence of secondary phases that could not be detected by XRD such as ZnS and Cu_2SnS_3. Figure 4.29 displays the Raman patterns of the annealed films with plotted dashed lines showing the positions of CZTS peaks. All annealed films show almost similar patterns, with the most intense CZTS peaks located at 288 and 339 cm^{-1}, no matter what stack sequence was used to prepare the films. The spectra also showed the CZTS broad peak between 368 and 373 cm^{-1}.

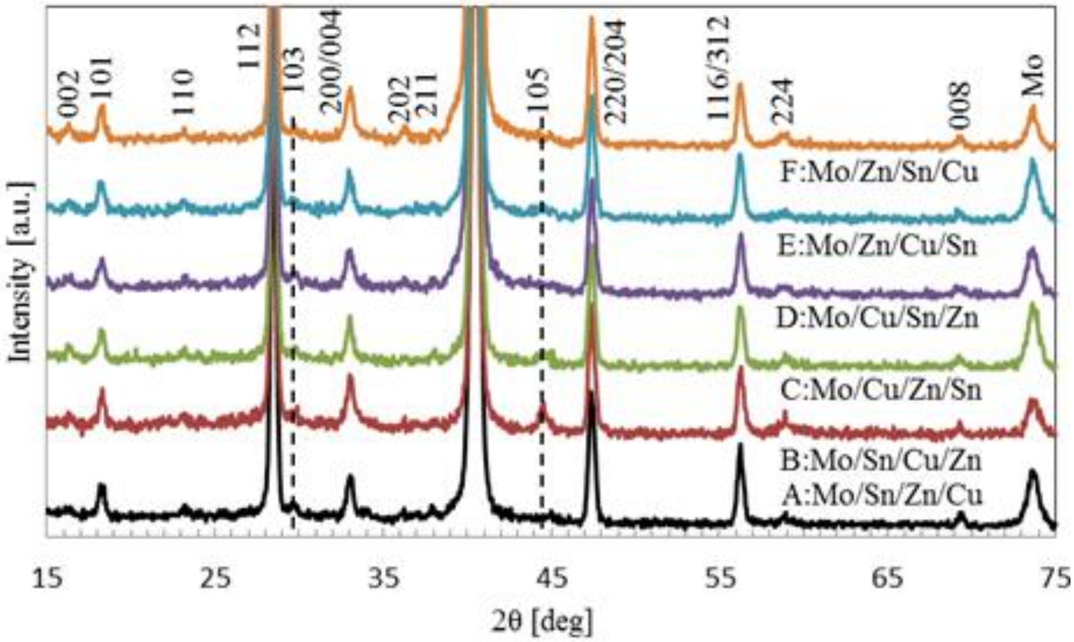

Figure 4.28: XRD spectra of CZTS films originated from precursors with different stacking sequences.

As mentioned earlier, the final CZTS films showing Zn-rich composition and ZnS phase is expected. Nevertheless, Raman spectra of all sulfurized films did not show a clear sign of the ZnS main peak at 352 cm^{-1} due to the difficulty of distinguishing ZnS from CZTS when using laser excitation in the visible region [127]. However, Raman measurements revealed a weak peak at 672 cm^{-1} that could belong to the second order of the ZnS phase peak.

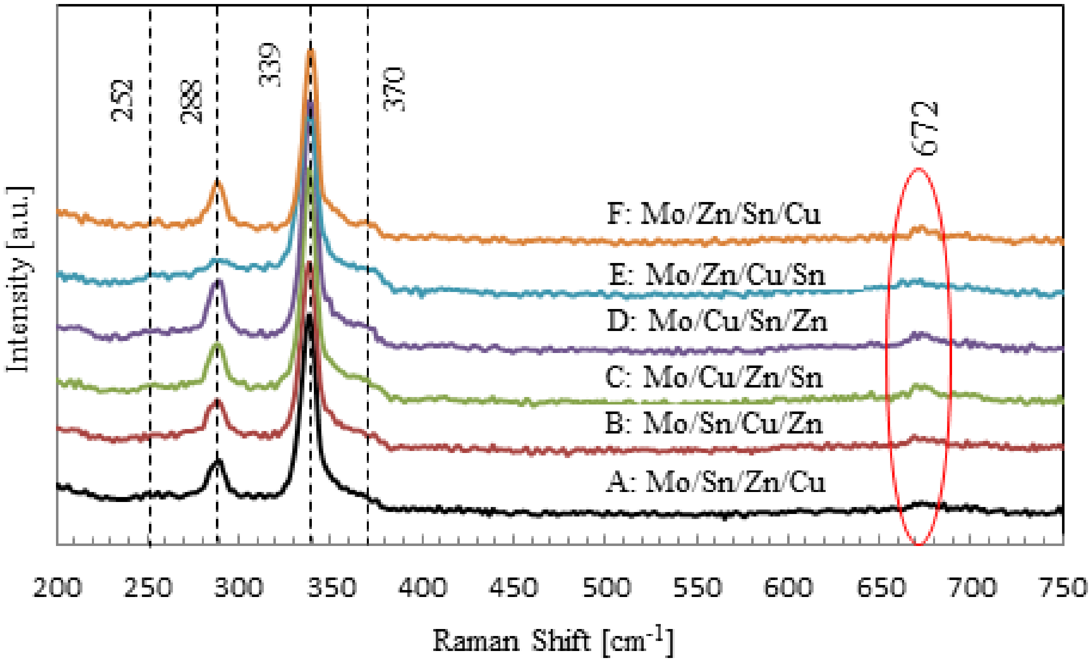

Figure 4.29: Raman spectra of CZTS films originated from precursors with different stacking sequences.

4.5.3.3 Study of film morphology and surface roughness

Plan-view and cross-sectional SEM scans of the metal precursors and sulfurized CZTS films were conducted to study the influence of the precursor stack orders on the morphology. Figure 4.30 shows plan-view SEM micrographs of the metal precursor with different stack sequences. As can be seen, the metal films exhibit different surface morphology in terms of grain size and compactness. By only observing the surface morphology, no clear trend could be made to relate it to the stacking orders.

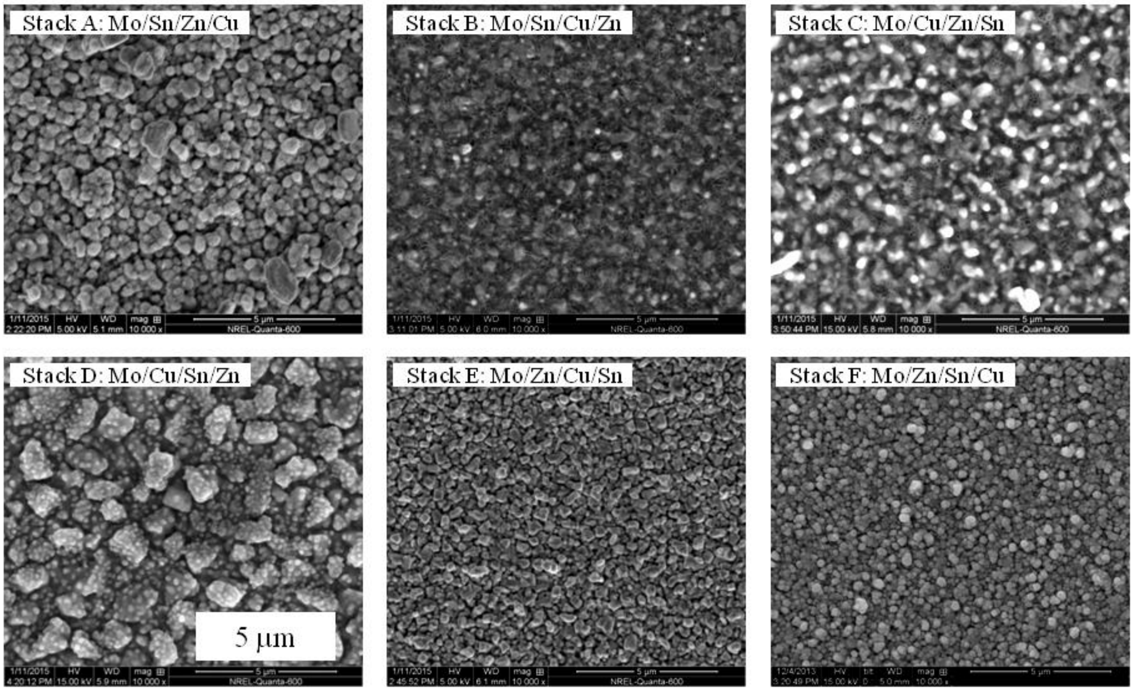

Figure 4.30: Plan-view SEM micrographs of the metal precursors with different stacking orders.

Cross-sectional SEM micrographs of all CZTS films are illustrated in Figure 4.31. In general, all films showed some surface roughness and dense bulk structures with some variation in grain size. The films prepared from precursors having Cu sputtered directly onto the Mo layer exhibited volcano-shaped voids on the surface and features of voids at the Mo/CZTS interface. The volcano-shaped voids are marked with red squares on the top-view SEM micrographs illustrated in Figure 4.32. The development of these voids could be explained by the relatively higher Cu diffusion rate, causing the migration of Cu to the film top and consequently leaving voids at the bottom. Both films that originated from precursors having Zn deposited on top exhibited the most voids at the Mo/absorber interface—especially film B, which showed clear separation from the Mo layer at some regions. On the contrary, the precursors with Zn deposited directly on Mo or as the second layer resulted in CZTS films with fewer voids at the Mo/film interface. All films exhibit, to a varying degree, features of voids at the Mo/absorber interface. So one can speculate that the precursor stacking order plays a role for their development, but also, that the sulfurization condition and/or the precursor chemical composition might have an additional impact.

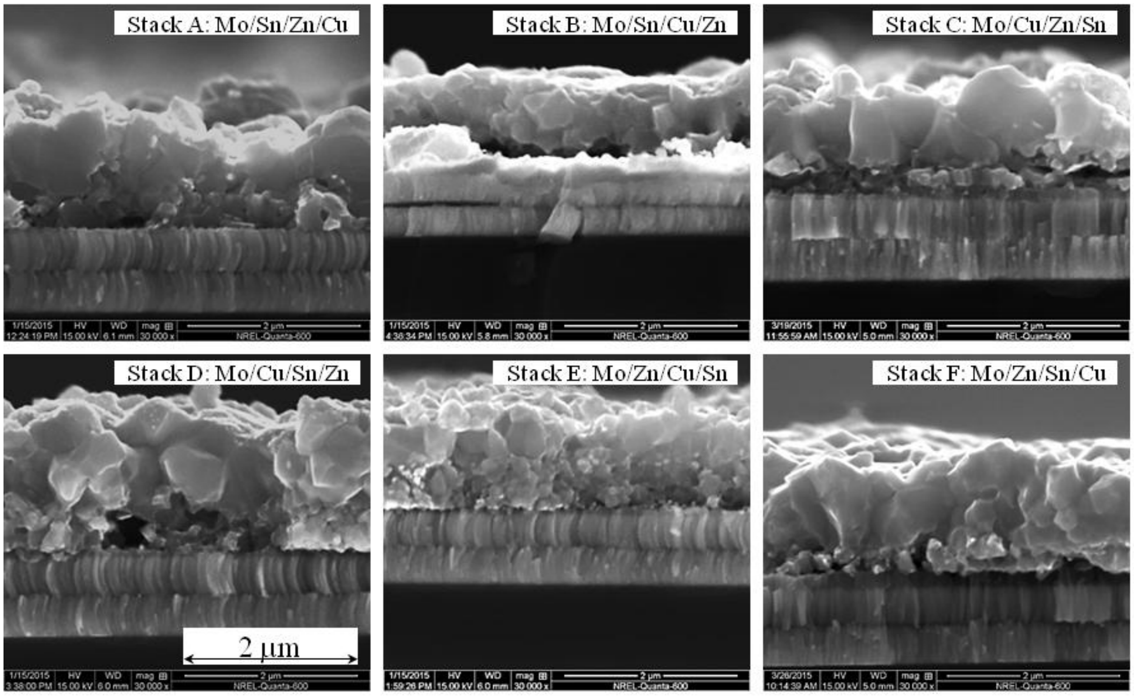

Figure 4.31: Cross-sectional SEM micrographs of the CZTS films originated from precursors with different stacking order.

The cross-sectional images also showed bi-layered CZTS films where a thin layer with small grains is formed at the bottom and a thicker layer with larger grains at the top. Bi-layering in CZTS was reported to be due to the formation of molybdenum sulfide (MoS_2) at the Mo/CZTS interface [231]. It has been reported that the interfacial $MoSe_2$ layer in CZTSe thin-film solar cells can be controlled by the annealing temperature [232]. Hence, optimizing the sulfurization parameters such as annealing temperature, duration, and sulfur partial pressure could reduce or eliminate the voids at the Mo/CZTS interface.

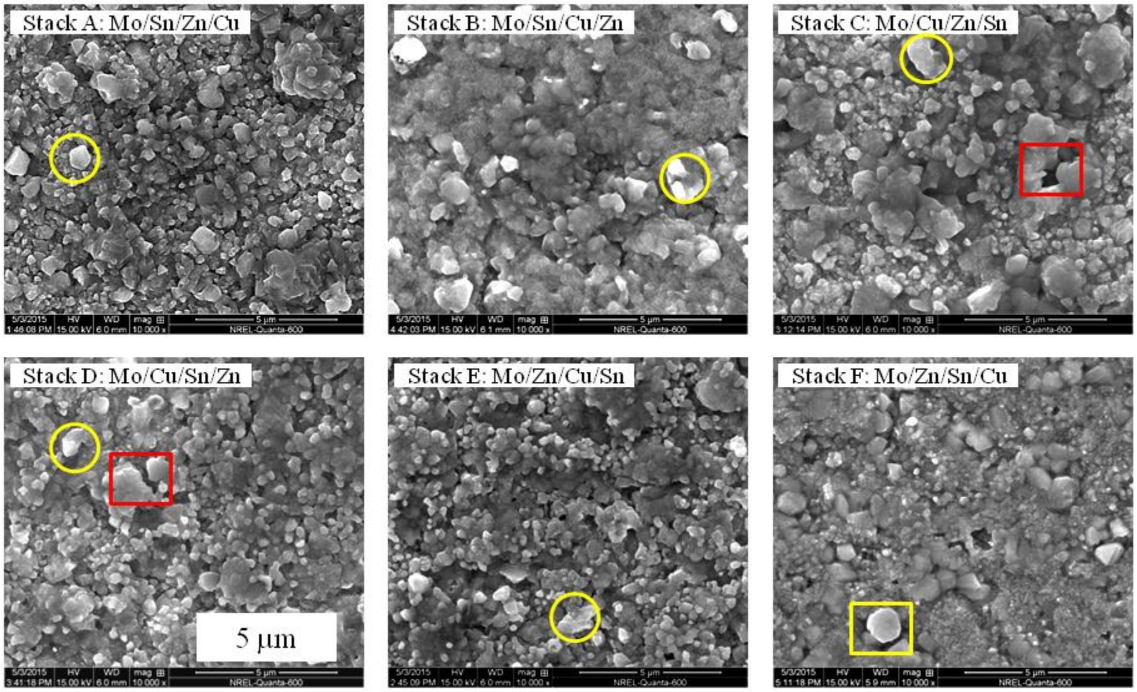

Figure 4. 32: Plan-view SEM micrographs of CZTS films prepared by the sulfurization of precursors with different stacking orders.

SEM/EDS scans at the Mo/absorber interface of our films did indeed reveal the formation of Mo-S layers. Figure 4.33 shows a cross-sectional micrograph of film D at which EDS point scans were conducted near and at the Mo/absorber interface and at a region close to the surface. The chemical composition data measured at different points of the cross-section are listed in Table 4.15. The high S and Mo concentration determined at points 2 and 3 is a good indication of the presence of MoS_2. In addition, EDS scans over some grains revealed high Zn concentration at the back of the film, indicating the presence of ZnS phase.

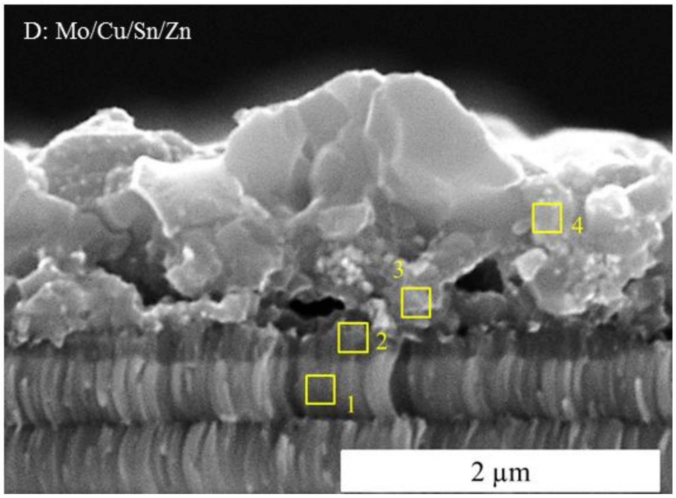

Figure 4.33: Cross-sectional micrograph of film D at which EDS point scans were conducted near and at the Mo/absorber interface.

ZnS grains were also detected by EDS on the surface of all films, except the one where Zn was deposited on Mo and Cu on top. The ZnS grains segregated on the surface are marked with yellow circles on the micrographs shown in Figure 4.32. The separated grains on the surface of film F with Zn on the bottom and Cu on top showed a composition related to CZTS. The composition of the marked grains on the micrograph is shown in Table 4.16.

Table 4.15: Chemical composition from EDS scans conducted at several points of film D cross-sectional SEM illustrated in Fig. 4.33.

	Point 1	**Point 2**	**Point 3**	**Point 4**
Cu (%)	1.77	6.53	13.77	20.13
Zn (%)	0.77	8.62	15.74	17.40
Sn (%)	2.57	6.39	7.69	10.75
S (%)	25.83	53.92	60.73	51.45
Mo (%)	69.06	24.54	2.07	0.27

Table 4.16: Chemical composition from EDS scans of the grains marked with yellow squares and circles illustrated in Fig. 4.32.

	S (%)	**Cu (%)**	**Zn (%)**	**Sn (%)**
Film A	48.51	13.71	27.90	9.88
Film B	51.54	23.08	11.64	13.75
Film C	52.16	10.98	29.42	7.44
Film D	52.06	11.17	29.79	6.98
Film E	50.45	12.34	27.79	9.42
Film F	51.70	20.70	13.87	13.73

Atomic force microscopy measurements were conducted on an area of 400 μm^2 of the CZTS films to better judge the surface roughness of the final CZTS films and to investigate the relationship between the different precursor stack orders and the surface roughness. AFM 3-D micrographs of the examined surfaces are illustrated in Figure 4.34. Micrograph C shows the volcano-shaped voids that were observed in the plan-view SEM images, exhibiting relatively large grains surrounding the volcano-shaped opening. The calculated roughness arithmetic mean (roughness average: R_a) and root mean square (RMS: R_q) are listed in Table 4.17. Generally, to a varying degree, all films exhibit rough surfaces.

Table 4.17: Calculated roughness average (R_a) and root mean square (R_q) of the CZTS films prepared by the sulfurization of metal precursors with different stacking orders.

Sample	**A**	**B**	**C**	**D**	**E**	**F**
R_a (nm)	127	95	164	134	157	63
R_q (nm)	161	126	209	167	195	82

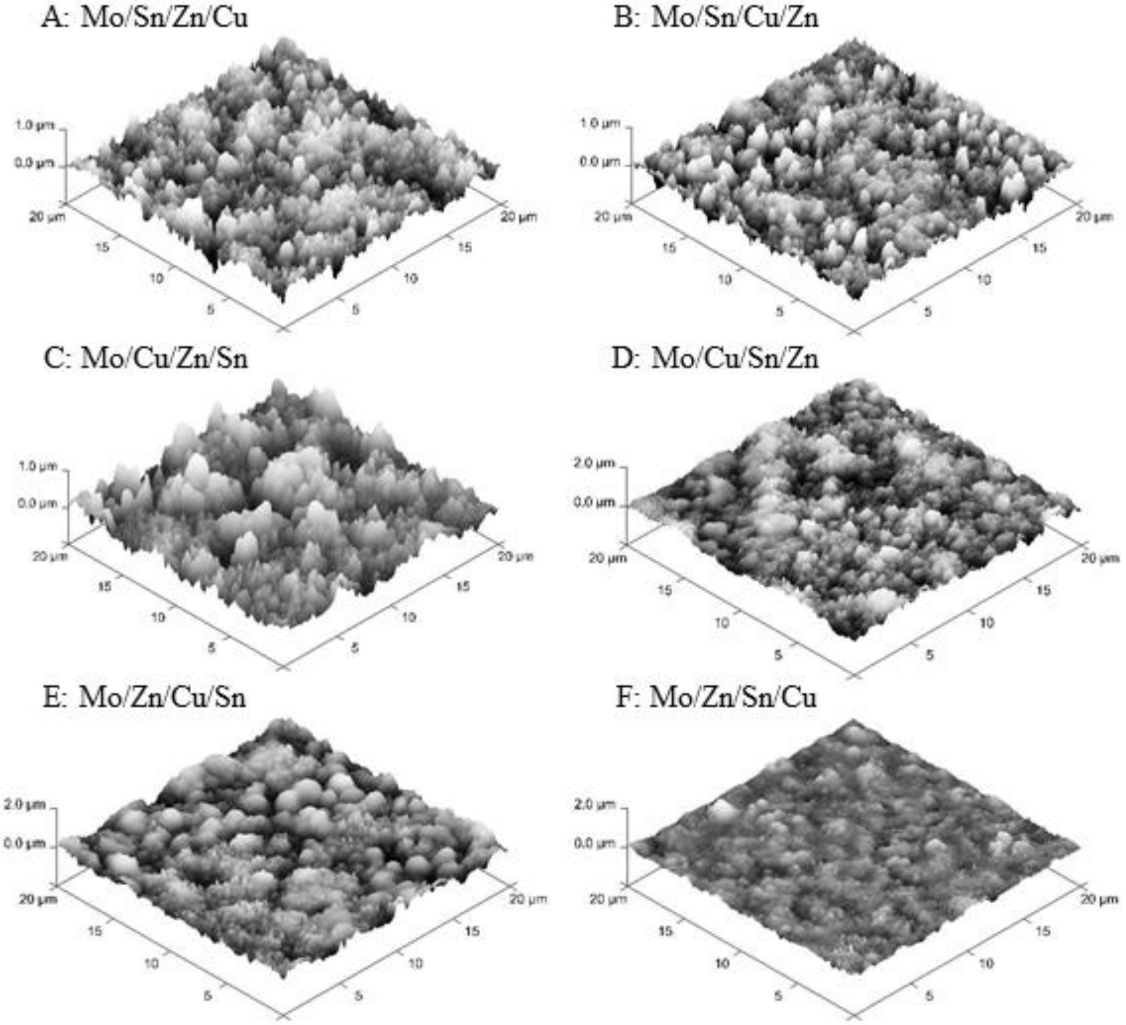

Figure 4.34: 3-D AFM micrographs showing the surface roughness of the prepared CZTS films.

4.5.3.4 Microstructure study

To further investigate the microstructure of our CZTS films, EBSD was used mainly to determine grain size. But also, as stated earlier, film texture and local orientation distribution can be determined. Because all CZTS films showed rough surfaces, the samples were ion-milled to reduce surface roughness to avoid shading. Figure 4.35 illustrates an SEM micrograph (a), Kikuchi patterns (EBSPs) (b), and indexed patterns to the CZTS phase (c) of an ion-milled surface of film F. The high-quality EBSP indicates good film crystallinity.

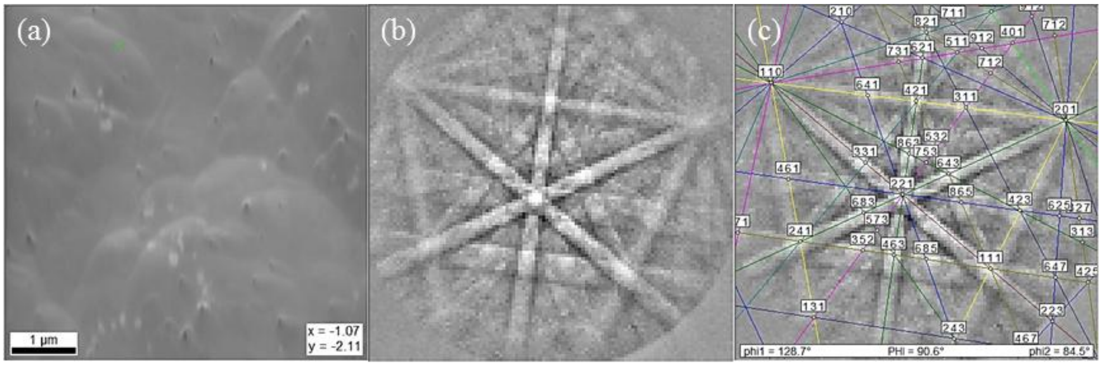

Figure 4.35: SEM plan-view (a), EBSPs (b), and indexed EBSPs (c) of film F with stacking order Mo/Zn/Sn/Cu.

The average lateral grain size calculated by the software for the CZTS films A–F were 0.65, 0.46, 0.54, 0.69, 0.57, and 0.37 μm, respectively. Grain-color maps, after removing the twin boundaries, of films A–F showing the grain size at areas where the data were collected are shown in Figure 4.36.

4.5.3.5 Solar cells

New CZTS absorber layers were prepared on Mo-coated SLG substrates with the same conditions used for the analyzed CZTS films to produce photovoltaic devices. For the complete devices, J-V characteristics and EQEs were measured. Figure 4.37 shows the illuminated J-V curve of cell A, which exhibited the highest efficiency of 4.43%.

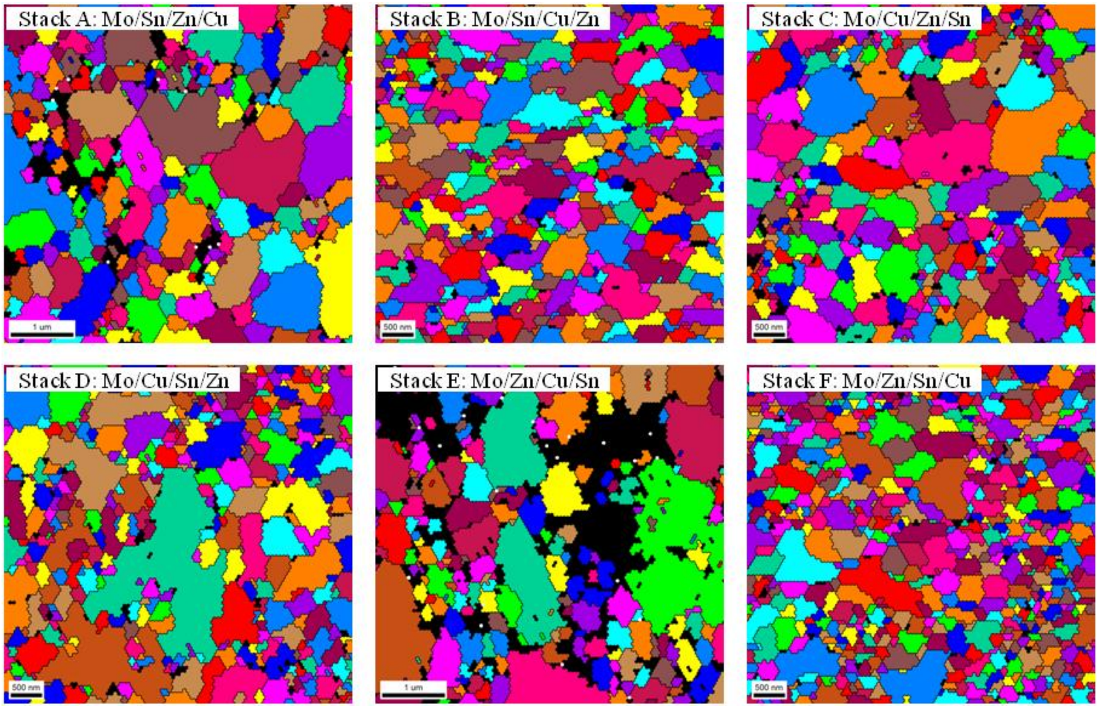

Figure 4.36: Grain-color maps of films A–F, showing grain size at the areas where the data were acquired.

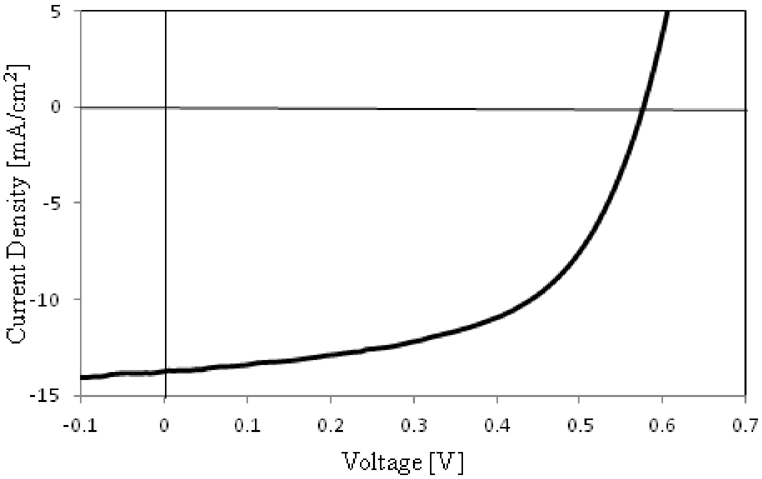

Figure 4.37: J-V illuminated curve of cell A with PCE of 4.43%.

The main electrical parameters of all cells are listed in Table 4.18. In contrast to Araki's work, the best cell PCEs were achieved in our study when Cu and Sn are not adjacent (cells A and C). Their best cell with a PCE of 1.79% resulted from precursors with stacking order Mo/Zn/Cu/Sn, whereas our cell with the same stacking order exhibited a PCE of 4.25%, which indicates the quality of our films.

Table 4.18: Electrical parameters of solar cells prepared from precursors with different stack orders.

Cell	V_{oc} (V)	J_{sc} (mA/cm^2)	FF (%)	η (%)
A	0.577	13.76	55.8	4.43
B	0.481	10.22	52.9	2.60
C	0.613	13.33	54.1	4.42
D	0.548	11.10	53.7	3.26
E	0.597	11.97	59.5	4.25
F	0.580	13.84	54.5	4.37

To obtain a better comparison, open-circuit voltage and short-circuit current are displayed as a function of the precursor stack order in Figure 4.38. Comparing the performance, cells A, C, and F exhibit related PCEs. Unlike the other cells, they show a short-circuit current density higher than 13 mA/cm^2 and fill factor of about 55%. Generally, all devices exhibit low J_{sc} due to high series resistance, causing a reduction of FF and consequently the efficiency. The cells showed efficiencies higher than 4% from devices with an absorber layer with a stack order where Zn was deposited as the first or second layer in the stack.

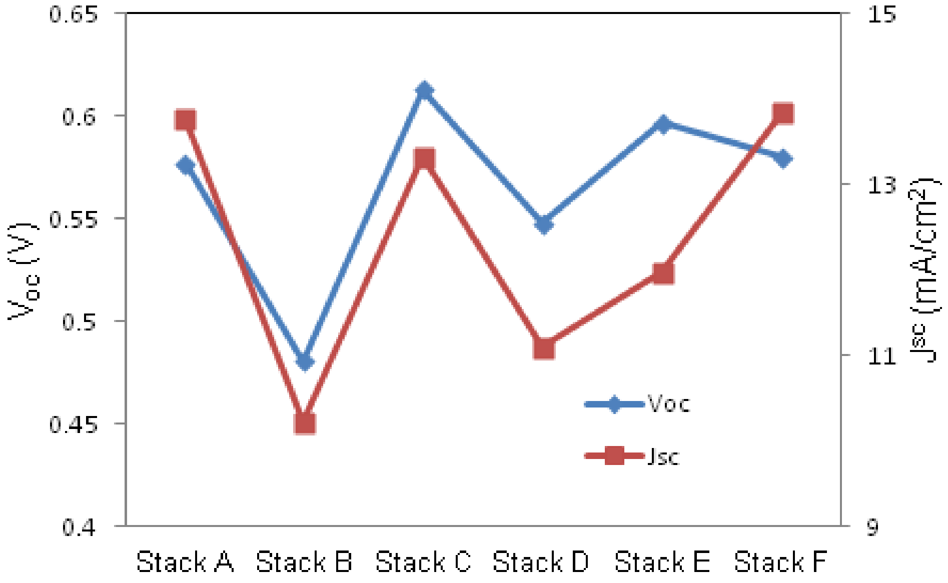

Figure 4.38: Open-circuit voltage and short-circuit current density as a function of the precursor stack order.

Figure 4.39 illustrates the EQE spectra of the fabricated cells as a function of wavelength. All curves exhibit their maximum at 530 nm. All devices show poor efficiency in the long-wavelength region, resulting in a poor carrier collection in this regime, which explains the lower J_{sc} of the devices.

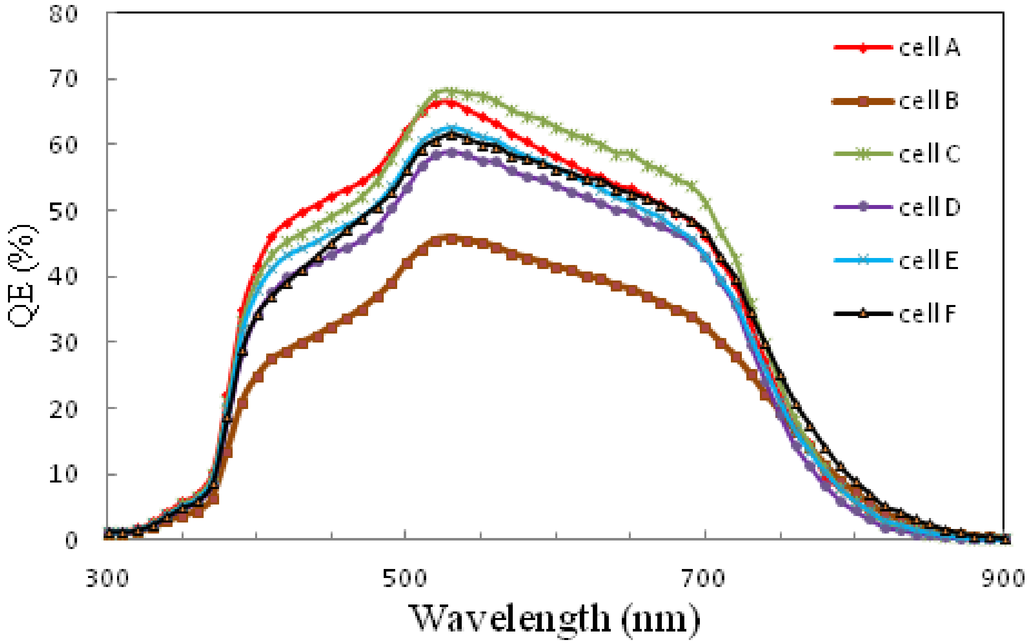

Figure 4.39: External quantum efficiency of the produced cells.

From the EQE spectra, the bandgap was estimated by graphing hv.ln(1–EQE)^2 vs photon energy (Figure 4.40). The estimated bandgap of the absorber layers ranges between 1.62 and 1.65 eV. The obtained bandgap values are indeed higher than the optimal CZTS bandgap of 1.5 eV. Similar values were obtained by Fernandes *et al.* [233] using EQE to estimate the bandgap. They reported achieving a bandgap of 1.5 eV using transmittance and reflectance measurements.

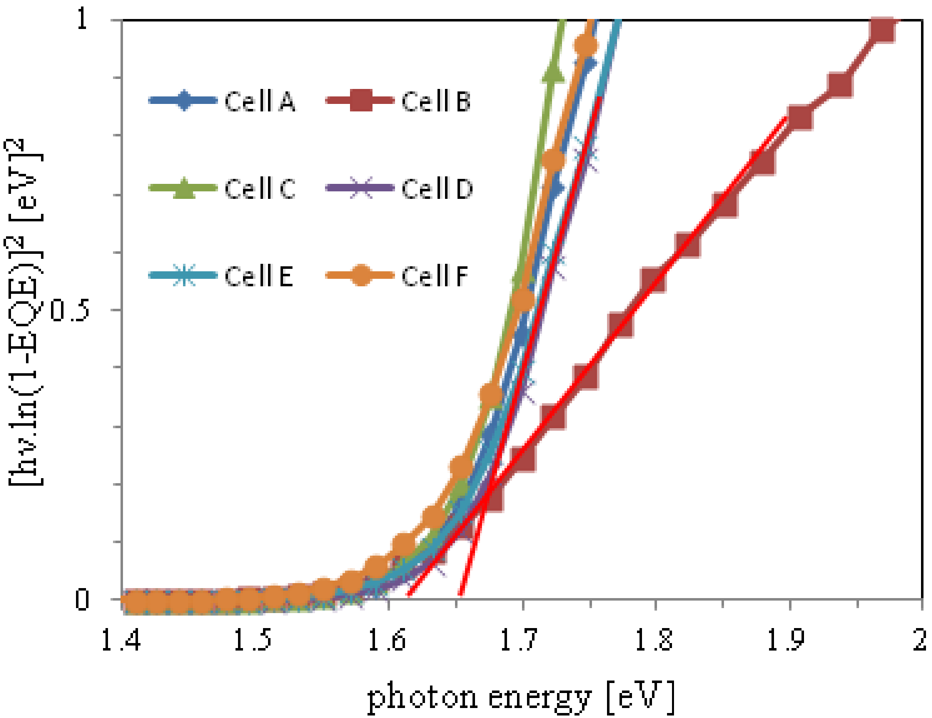

Figure 4.40: Bandgap estimation of the absorber layers by plotting hv.ln(1–EQE)^2 as a function of hv.

4.5.4 Conclusion

In this study, polycrystalline Cu_2ZnSnS_4 thin films were prepared by annealing metal precursors with different stack orders in sulfur atmosphere. Depending on the stack used, the chemical composition of the metal precursors showed some variation, and the annealed films revealed Sn loss that was minimized slightly when Cu was deposited on Sn or Zn/Sn layers. ZnS crystallites were formed in the sulfurized films as a result of the high Zn concentration in the starting metal precursor. However, this phase could be minimized or avoided by optimizing the composition of the starting precursors. Different stacking orders of the metal precursor did not show noticeable impact on the crystallographic structure of the final CZTS films. On the other hand, the stack sequence of the precursor showed some influence on the morphology of the final films. Precursors with a Zn layer deposited directly on Mo or as the second layer showed better adhesion to the substrate and fewer voids at the Mo/absorber interface. Similarly, the cells with the highest efficiency were made from CZTS active layers that originated from precursors where Zn was deposited directly on Mo or as the second layer. Generally, all devices suffered mainly from low current due to the voids in the absorber layer. Further work is ongoing to optimize the composition of the final CZTS films and to optimize the annealing process.

4.6 CZTS films from co-sputtered precursors

Portions of the results included in this section were presented in the SPIE Optics + Photonics for Sustainable Energy conference as: M. Abusnina, M. Matin, H. Moutinho, and M. Al-Jassim, "Characterization of Cu_2ZnSnS_4 Thin Films Prepared by the Sulfurization of Co-sputtered Metal Precursors," Proc. of SPIE Vol. 9561, 95610L-1.

4.6.1 Introduction

Our second approach for preparing the metal precursor is based on simultaneously sputtering the metal targets onto the substrate (co-sputtering). Compared to sequential sputtering, simultaneous sputtering produces more homogeneous precursors [81]. Co-sputtering is widely used to deposit the Cu-Zn-Sn precursor; however, binary metal sulfides are commonly used instead of elemental targets to incorporate sulfur in the precursor and to enhance the interdiffusion of the elemental composition in the precursor. Using Cu, ZnS, and SnS targets, Jimbo *et al.* [212] prepared CZTS films by sulfurizing co-sputtered precursors and achieved a device efficiency of 5.77%. Comparing metallic precursors with precursors containing sulfur, Björkman *et al.* [234] reported on uniform CZTS films with fewer voids when using sulfur-containing precursors. The main reason for not using metal sulfide targets in our project was to avoid contaminating the deposition chamber with sulfur, thus allowing the system to remain available for depositing other materials.

The largest portion of the CZTS films investigated in this study was based on stacked precursors, with the goal of transferring results obtained to fabricate films from co-sputtered precursors. In this section, we present the results and analysis of CZTS from co-sputtered precursors.

4.6.2 Controlling the chemical composition

As demonstrated at the beginning of this chapter, it is quite challenging to obtain a certain composition for a co-sputtered precursor, and it requires depositing several samples by adjusting the sputtering powers to achieve the desired composition. The process becomes more difficult if a predefined film thickness is required.

A second factor that significantly affects the composition of the final CZTS films is the loss of Sn during the annealing treatment. Unlike stacked precursors, co-sputtered films show a considerable loss of Sn after sulfurization, leading to a clear degradation of composition between the precursor and sulfurized film. Results from previous work showed that insufficient Sn content in the film leads to the evolution of $Cu_{2-x}S$ phases. To compensate for the loss of Sn during annealing, we could start with precursors having excess Sn or supply extra Sn during the sulfurization process in the form of Sn vapor.

4.6.3 Effect of sulfurization conditions

Recalling the composition data for film 95 presented earlier in this chapter, we can see the impact on film composition after sulfurization. The precursor resulted from co-sputtering Cu, Zn, and Sn with 70, 30, and 40 W, respectively, for 60 min, and then annealing in sulfur vapor at 550 °C for 60 min. The composition of the film before and after sulfurization is illustrated in Figure 4.41, where the black dot refers to the composition before and the red circle after sulfurization. Initially, the precursor had a Cu/(Zn+Sn) ratio of 0.82 and Zn/Sn ratio of 1.07, and then moved toward the Zn-rich and

Sn-poor region after annealing. The deficiency of Sn led to the formation of Cu$_{2\text{-}x}$S and ZnS phases in the film.

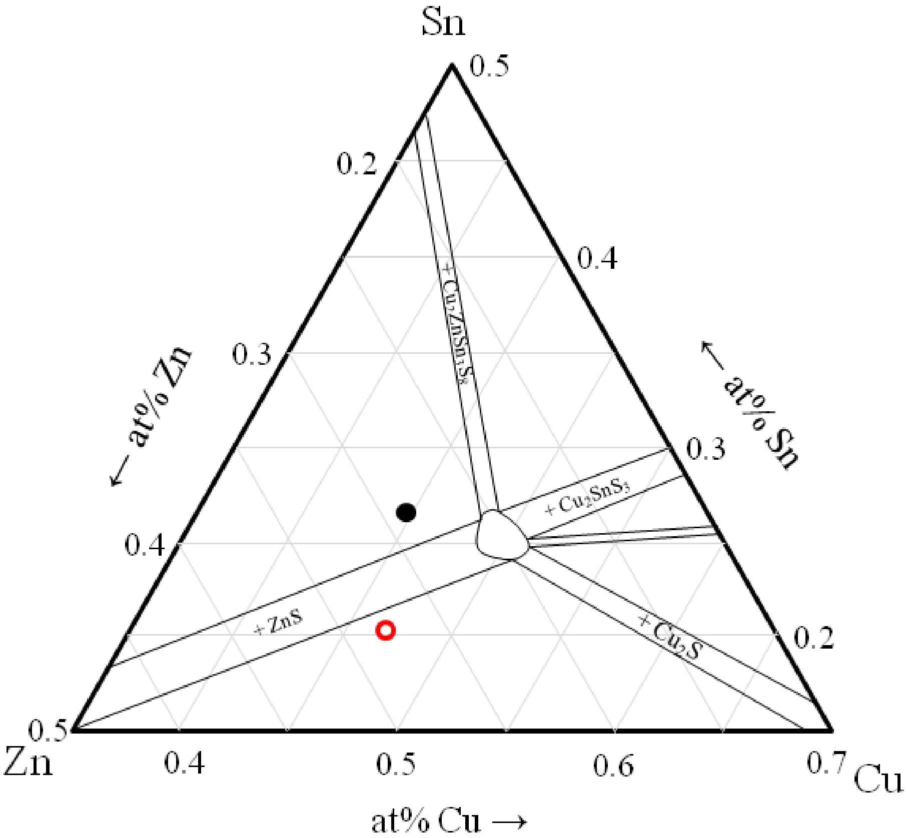

Figure 4.41: Chemical composition of film 95 prepared from a co-sputtered precursor. Black dot refers to the composition before sulfurization and red circle after sulfurization.

Considering Sn loss, the sputtering powers were modified to prepare a new series of precursors with high Sn concentration. Moreover, the sputtering time was reduced from 60 min to 45 min to minimize the final film thickness to about 1 µm. Using sputtering powers of 50–52, 21–22, and 32–35 W for Cu, Zn, and Sn, respectively, we achieved precursors with Cu/(Zn+Sn) ratios ranging from 0.78 to 0.84 and Zn/Sn ratios ranging from 0.66 to 0.81. The primary sulfurization treatment of these precursors revealed slightly Cu-poor, Zn-rich, and Sn-poor concentration, enabling CZTS films with compositions close to stoichiometric.

As a representative of the new precursors, film 183 is co-sputtered on a Mo-coated SLG substrate with 52, 21, and 35 W applied to Cu, Zn, and Sn targets, respectively. The precursor was then cut into two pieces that were sulfurized under different conditions. CZTS film 183-1 resulted from annealing the precursor in sulfur vapor at 600 °C for 60 min, whereas film 183-2 experienced 30 min of annealing in N_2 atmosphere before being sulfurized at 570 °C for 60 min. The chemical composition of the metal precursor and the two sulfurized films is shown in Table 4.19. Despite the high temperature and the long duration of treatment, the CZTS film is still Sn-rich after the treatment, indicating that the loss of Sn was successfully controlled. Comparing the composition of both films to the preferential values for the solar cell, further tuning is needed of the final composition to achieve a Cu/(Zn+Sn) ratio of about 0.85 and Zn/Sn ratio of about 1.1.

Table 4.19: Chemical composition and compositional ratios of film183 prepared by the sulfurization of co-sputtered precursor at 600 °C for 60 min.

	Cu (%)	**Zn (%)**	**Sn (%)**	**Cu/(Zn+Sn)**	**Zn/Sn**
Precursor	44.3	22.7	33.0	0.79	0.69
Film 183-1	48.2	25.1	26.7	0.93	0.94
Film 183-2	48.2	24.7	27.1	0.93	0.91

Plan-view SEM micrographs of both CZTS films are shown in Figure 4.42. Both films exhibit dense morphology; however, film 183-1, which was annealed at 600 °C, clearly shows some large grains. An EDS scan over numerous grains of both films showed composition close to stoichiometric, with no signs of composition degradation or presence of secondary phases. Figure 4.43 shows a cross-sectional SEM image and EDS line scan over the surface of film 183-1. The EDS line scan reveals a relatively homogeneous composition, and the SEM image indicates a thickness of about 850 nm for the film, close to the desired thickness of 1 μm.

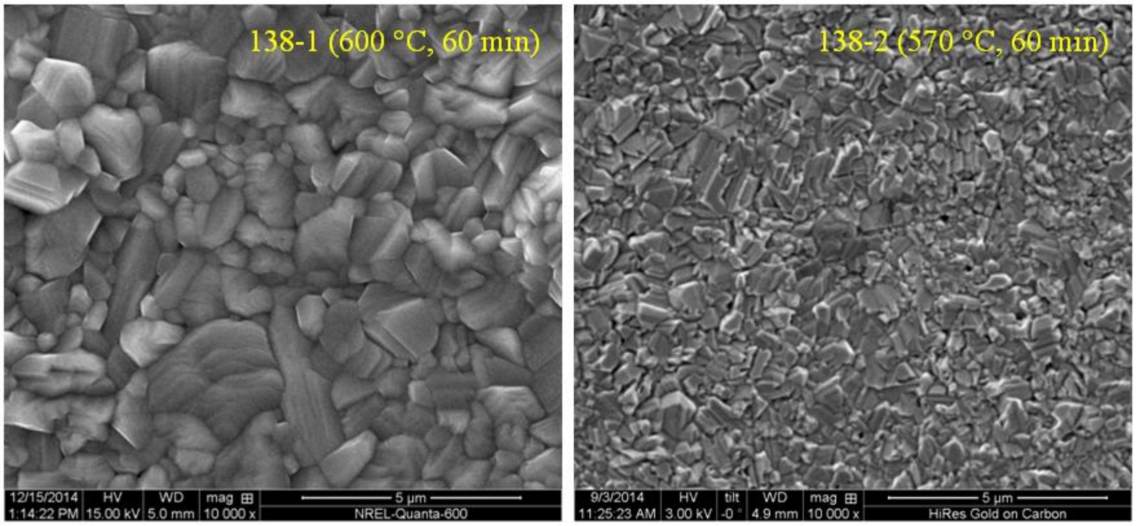

Figure 4.42: Plan-view SEM images of films 183-1 and 183-2.

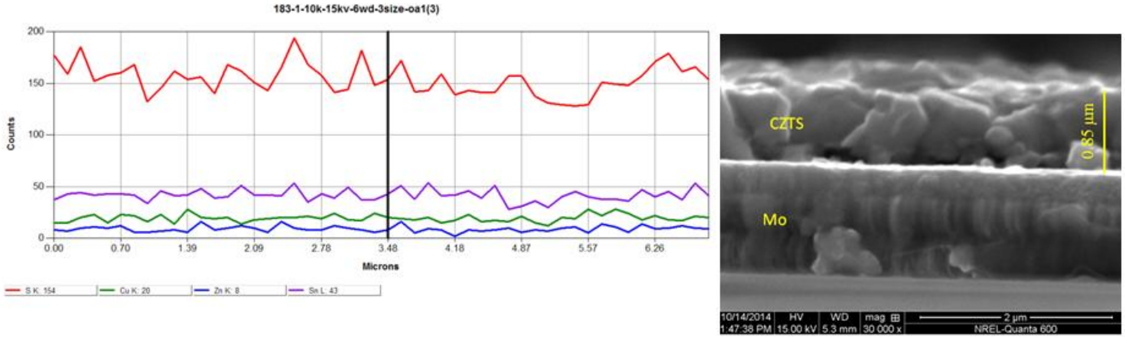

Figure 4.43: EDS line scan over the surface area of film 183-1 shown in Figure 4.41 (left), and cross-sectional SEM micrograph of the same film (right).

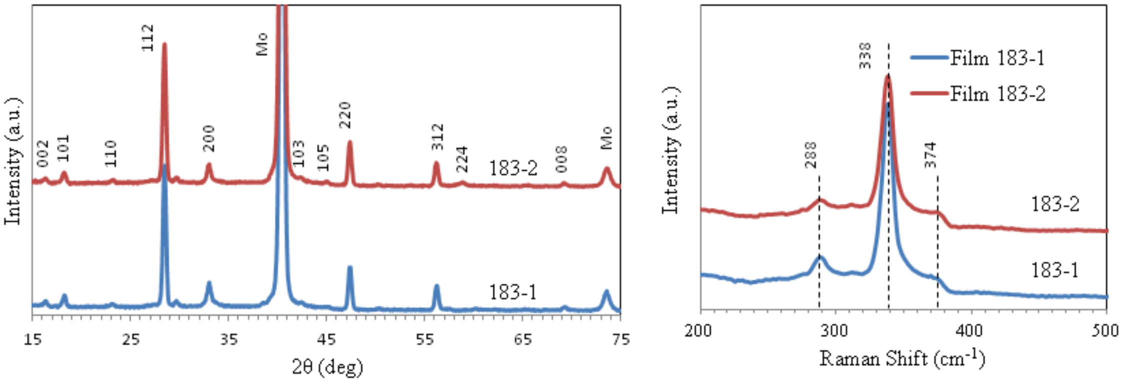

Figure 4.44: XRD and Raman spectra of films 183-1 and 183-2 prepared by sulfurizing co-sputtered precursor.

We conducted XRD and Raman spectroscopy measurements to investigate the crystallographic structure of the films and identify the phases. As Figure 4.44 shows, the spectra correspond to kesterite CZTS with no evidence of secondary phases.

Both films exhibited very good quality in terms of homogenous composition, single-phase crystal structure, dense morphology with large grains, and smooth surface. However, SEM revealed some areas of clear separation of the CZTS film from the Mo layer. Figure 4.45 shows plan-view and cross-sectional SEM micrographs of a region where the films have blistered. This effect is widely known in thin films and is attributed to compressive intrinsic stresses in the film [235]. It is beyond the scope of this project to inspect the origin of intrinsic stresses and study buckling delamination of thin films.

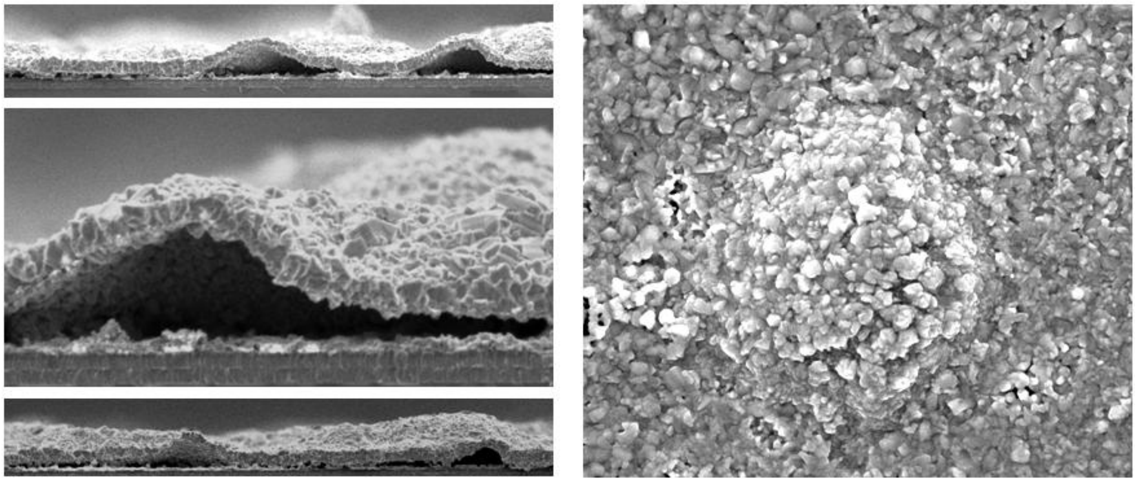

Figure 4.45: Plan-view and cross-sectional SEM micrographs showing blisters in CZTS films prepared by the sulfurization of co-sputtered films.

Further experiments were conducted to optimize the film adhesion to the substrate by reducing the temperature and annealing time. Although the blister effect was minimized—and in some cases eliminated—the resulting films exhibited porous morphology.

The beset device based on an absorber layer prepared by the sulfurization of a co-sputtered precursor showed an efficiency of 1.72%. The metal precursor was annealed in sulfur ambient at 550 °C for 60 min. The electrical parameters for this device are listed in Table 4.20.

Table 4.20: Characteristics of the best cell based on CZTS absorber layer prepared by sulfurizing a co-sputtered metal precursor.

V_{oc} (V)	J_{sc} (mA/cm^2)	FF (%)	η (%)
0.471	9.92	36.9	1.72

4.6.4 Conclusion

CZTS films were prepared by the sulfurization of co-sputtered metal precursors. The chemical composition of the precursor was challenging and requires considerable effort to control the final film composition. We achieved single-phase CZTS films with good crystallinity and dense morphology. Further investigation is required to address the origin of the intrinsic stresses in the films and how to avoid their existence. The highest efficiency of 1.72% was obtained from a device based on CZTS film fabricated by the sulfurization of co-sputtered metal precursor.

Chapter Five: Summary

At the beginning of this study, we set several goals to be achieved within the scope of the project. The ultimate target was to develop high-quality Cu_2ZnSnS_4 (CZTS) thin films as active absorber layers in thin-film solar cells. To reach the objective of our project, CZTS thin films were grown and characterized to understand the growth mechanism of the material, identify the impact of the growth conditions on film properties, optimize the growth process, and apply the developed films in photovoltaic devices.

Our CZTS thin-film fabrication process relies on two steps:

In the first step, a metal film is deposited from elemental copper, zinc, and tin targets on glass substrates using magnetron RF sputtering. Initially, the films were deposited on soda-lime glass (SLG) substrates; at a later point in time, we decided to prepare the films only on molybdenum-coated (Mo-coated) SLG substrates unless the optical properties of the films needed to be investigated. It is already known that sulfur reacts with Mo back-contact film, and a layer of MoS_2 is formed at the Mo/CZTS interface. The metal precursors were realized as a stack of layers, where one metal at a time is deposited, or where the three metals are deposited simultaneously as a co-sputtered film.

In the second synthesis step, the metal films are annealed in sulfur ambient to convert the precursors into a kesterite CZTS compound. In both stages, several parameters can be adjusted to control the film properties such as chemical composition, crystallographic structure, or morphology. The results of our study are presented in Chapter 4.

To control the chemical composition and thickness of the metal precursor, the sputtering system was calibrated and sputtering rates were determined. Primary results showed that controlling the composition of the stacked films can be achieved by varying the thickness of the different metal layers, and the required composition and thickness can be predicted based on the determined deposition rates. Controlling the composition of co-sputtered films, on the other hand, turned out to be more challenging due to the interplay of the particles within the deposition chamber. Therefore, several depositions are necessary to obtain the required composition. Our approach to convert the metal films into kesterite CZTS relies on the use of a three-heating-zone quartz-tube furnace, where the sample is placed in one of the zones and elemental sulfur powder in the other one. N_2 or Ar flux was used to carry the sulfur vapor inside the tube. By installing aluminum silicate rings between the heating zones, we were able to reduce heat transfer between the zones and achieve better control of the temperature.

Studying the influence of the sulfurization condition on the properties of the prepared CZTS films showed that temperatures from 500 °C and up to 600 °C are necessary to complete the compound crystallization. XRD and EDS measurements revealed the presence of secondary phases such as Cu_2SnS_3, $Cu_{2-x}S$, and ZnS, in addition to CZTS when annealing the films at 450 °C. The study also gave us more insight into the reaction pathway of the material and addressed the importance of the precursor chemical composition in developing secondary phases during the sulfurization process. We noted a variation in the measured compositional values and a discrepancy in data acquired by different characterization techniques to determine the chemical composition of the CZTS films. We explain these observations by considering the nonuniform distribution of the Cu-S grains on the film surface, which lead to different values depending on the region where data are collected. In this set of experiments, we obtained CZTS films with energy bandgaps close the optical value of 1.5 eV.

The impact of the chemical composition on the film properties and the evolution of secondary phases were investigated by characterizing CZTS films fabricated by annealing metal precursors with a stack order of SLG/Mo/Zn/Sn/Cu in sulfur atmosphere at 540 °C for 60 min. From EPMA data, the CZTS films had Cu/(Zn + Sn) ratios ranging between 0.81 and 1.05, realizing Cu-poor and Cu-rich composition. The investigation showed that the amount of Cu, but of Sn in the precursor is the factor controlling the development of $Cu_{2-x}S$ phases. We proved, trough providing the right amount of Sn, $Cu_{2-x}S$ can be avoided in Cu-rich concentration. On the other hand, they develop in Cu-poor composition when amount of Sn is insufficient. The study also confirmed the grain size growth enhancement when high Cu amount incorporated in the film.

The impact of stacking order of the precursor on the properties of the polycrystalline Cu_2ZnSnS_4 thin films was inspected by annealing of metal precursors with different stack orders in sulfur atmosphere. Depending on the used stack, the chemical composition of the metal precursors showed some variation, and the annealed films revealed Sn loss that was slightly minimized when Cu was deposited on Sn- or Zn/Sn layers. ZnS crystallites were formed in the sulfurized films as a result of the high Zn concentration in the starting metal precursor. The stack order of the metal precursor did not show noticeable impact on the crystallographic structure of the final CZTS films. On the other hand, the stack sequence of the precursor showed some influence on the morphology of the final films. Precursors with Zn layer deposited directly on Mo or as the second layer showed better adhesion to the substrate and less voids at the Mo/absorber interface. Consequentially, the cells with the highest efficiency were made from CZTS active layers that originated from precursors where Zn was deposited directly on Mo or as the second layer. The highest power conversion efficiency of 4.43% was achieved for a device made of an absorber layer originated from a precursor with a stack of Mo/Zn/Sn/Cu. Generally, all devices suffered mainly from low current due to high series resistance.

CZTS films based on a co-sputtered precursor showed very promising results regarding dense morphology, large grain size, and smooth film surface. Controlling the chemical composition of both the metal precursor and the final CZTS film is more challenging compared to stacked films, and it would require greater effort and empirical correction of the composition. Although we achieved single-phase CZTS films with good crystallinity, the films exhibited an adhesion issue with the Mo back-contact layer due to compressive stresses. Further investigation is required to address the origin of the intrinsic stresses in the films and to avoid such stresses. A device based on CZTS film fabricated by the sulfurization of a co-sputtered metal precursor yielded a highest efficiency of 1.72%.

Some suggested future work based on my investigations and the results achieved within this study include the following:

1. The use of binary sulfide targets to prepare the precursors, especially the stacked ones, can result in films that are denser and more homogeneous. The sulfur can be incorporated earlier in the films, helping to reduce the elemental interdiffusion during the annealing process.

2. The compressive stress observed in films prepared from co-sputtered precursors needs to be studied in detail to determine the growth parameters that lead to its existence. One possible factor could be the sputter working pressure; hence, a study to optimize the working pressure is recommended to minimize or eliminate this intrinsic stress.

3. Further optimizing of the sulfurization time is required to reduce the duration of the process.

4. Coupling a mechanical pump to evacuate the quartz tube before the sulfurization treatment can minimize the contamination in the tube, and hence, lessen the impurities in the synthesized film, thus boosting device efficiency.

5. Optimizing the annealing temperature could control the MoS_2 layers observed at the interface between the film and Mo layer.

6. The high Zn concentration detected in the films prepared from the stacked precursor needs to be optimized to minimize or suppress the presence of ZnS phases.

7. Optimizing the thickness of the absorber layer is also recommended to minimize the fabrication time and to investigate its influence on the performance of the solar cell.

References

[1] EIA, U. (2013). International Energy Outlook 2013. US Energy Information Administration (EIA).

[2] OECD/IEA. (2015). Key World Energy Statistic 2015. Retrieved from https://www.iea.org/publications/freepublications/publication/KeyWorld_Statistics_2015.pdf.

[3] World Energy Council. (2013). World Energy Resources 2013 Survey. Retrieved from https://www.worldenergy.org/wp-content/uploads/2013/09/Complete_WER_2013_Survey.pdf

[4] OECD/IEA. (2015). CO_2 Emissions From Fuel Combustion. Retrieved from https://www.iea.org/publications/freepublications/publication/CO2EmissionsFromFuelCombustionHighlights2015.pdf.

[5] Zhu, X. G., Long, S. P., & Ort, D. R. (2008). What is the maximum efficiency with which photosynthesis can convert solar energy into biomass?. *Current opinion in biotechnology*, 19(2), 153-159.

[6] OECD/IEA. (2014). Snapshot of Global PV Markets. Retrieved from http://www.iea-pvps.org/fileadmin/dam/public/report/technical/PVPS_report_-_A_Snapshot_of_Global_PV_-_1992-2014.pdf.

[7] Green, M. A., Emery, K., Hishikawa, Y., Warta, W., & Dunlop, E. D. (2015). Solar cell efficiency tables (Version 45). *Progress in photovoltaics: research and applications, 23*(1), 1-9.

[8] First Solar press release. (2016, February 23). Retrieved from http://investor.firstsolar.com/releasedetail.cfm?ReleaseID=956479.

[9] Jackson, P., Hariskos, D., Wuerz, R., Kiowski, O., Bauer, A., Friedlmeier, T. M., & Powalla, M. (2015). Properties of Cu (In, Ga) Se_2 solar cells with new record efficiencies up to 21.7%. *physica status solidi (RRL)-Rapid Research Letters*, *9*(1), 28-31.

[10] Ito, K., & Nakazawa, T. (1988). Electrical and optical properties of stannite-type quaternary semiconductor thin films. *Japanese Journal of Applied Physics*, *27*(11R), 2094.

[11] Nakayama, N. & Ito, K. (1996). Sprayed films of stannite Cu_2ZnSnS_4. *Applied Surface Science*, 92, 171-175.

[12] Tanaka, K., Moritake, N., & Uchiki, H. (2007). Preparation of Cu_2ZnSnS_4 thin films by sulfurizing sol–gel deposited precursors. *Solar Energy Materials and Solar Cells, 91*(13), 1199-1201.

[13] Grossberg, M., Krustok, J., Timmo, K., & Altosaar, M. (2009). Radiative recombination in $Cu_2ZnSnSe_4$ monograins studied by photoluminescence spectroscopy. *Thin Solid Films, 517*(7), 2489-2492.

[14] Wang, W., Winkler, M. T., Gunawan, O., Gokmen, T., Todorov, T. K., Zhu, Y., & Mitzi, D. B. (2014). Device characteristics of CZTSSe thin-film solar cells with 12.6% efficiency. *Advanced Energy Materials*, *4*(7).

[15] Shin, B., Gunawan, O., Zhu, Y., Bojarczuk, N. A., Chey, S. J., & Guha, S. (2013). Thin film solar cell with 8.4% power conversion efficiency using an earth-abundant Cu_2ZnSnS_4 absorber. *Progress in Photovoltaics: Research and Applications, 21*(1), 72-76.

[16] Shockley, W., & Queisser, H. J. (1961). Detailed balance limit of efficiency of p-n junction solar cells. *Journal of applied physics, 32*(3), 510-519.

[17] Goetzberger, A., Voss, B., & Knobloch, J. (1994). Sonnenenergie: Photovoltaik: Physik und Technologie der Solarzelle. Stuttgart: B.G. Teubner.

[18] Green, M. A. (1992). Solar cells: Operating principles, technology and system applications. Kensington, N.S.W.: University of New South Wales. [19] Green, M. A. (2009). The path to 25% silicon solar cell efficiency: History of silicon cell evolution. *Progress in Photovoltaics: Research and Applications,17*(3), 183-189.

[20] Masuko, K., Shigematsu, M., Hashiguchi, T., Fujishima, D., Kai, M., Yoshimura, N., ... & Yamanishi, T. (2014). Achievement of more than 25% conversion efficiency with crystalline silicon heterojunction solar cell.Photovoltaics, *IEEE Journal of Photovoltaics, 4*(6), 1433-1435.

[21] Trina Solar Announces New Efficiency Record of 21.25% Efficiency for Multi-crystalline Silicon Solar Cell. (2015, November 9) Retrieved from http://www.trinasolar.com/us/about-us/newinfo_978.html

[22] Green, M. A., Emery, K., Hishikawa, Y., Warta, W., & Dunlop, E. D. (2015). Solar cell efficiency tables (Version 47). *Progress in photovoltaics: research and applications, 24*(1), 3-11.

[23] International Technology Roadmap for Photovoltaic (ITRPV): Results 2015. (2016, March) Retrieved from http://www.itrpv.net/Reports/Downloads/

[24] Miles, R. W., Hynes, K. M., & Forbes, I. (2005). Photovoltaic solar cells: An overview of state-of-the-art cell development and environmental issues.*Progress in Crystal Growth and Characterization of Materials, 51*(1), 1-42.

[25] Meillaud, F., Boccard, M., Bugnon, G., Despeisse, M., Hänni, S., Haug, F. J., ... & Ballif, C. (2015). Recent advances and remaining challenges in thin-film silicon photovoltaic technology. *Materials Today, 18*(7), 378-384.

[26] Carlson, D. E., & Wronski, C. R. (1976). Amorphous silicon solar cell. *Applied Physics Letters, 28*(11), 671-673.

[27] Staebler, D. L., & Wronski, C. R. (1977). Reversible conductivity changes in discharge-produced amorphous Si. *Applied Physics Letters, 31*(4), 292-294.

[28] Matsui, T., Sai, H., Suezaki, T., Matsumoto, M., Saito, K., Yoshida, I., & Kondo, M. (2013). Development of highly stable and efficient amorphous silicon based solar cells. In *Proc. 28th European Photovoltaic Solar Energy Conference* (pp. 2213-2217).

[29] Sai, H., Matsui, T., Koida, T., Matsubara, K., Kondo, M., Sugiyama, S., ... & Yoshida, I. (2015). Triple-junction thin-film silicon solar cell fabricated on periodically textured substrate with a stabilized efficiency of 13.6%. *Applied Physics Letters, 106*(21), 213902.

[30] El Chaar, L., & El Zein, N. (2011). Review of photovoltaic technologies.*Renewable and Sustainable Energy Reviews, 15*(5), 2165-2175.

[31] Bai, Z., Yang, J., & Wang, D. (2011). Thin film CdTe solar cells with an absorber layer thickness in micro-and sub-micrometer scale. *Applied Physics Letters, 99*(14), 143502.

[32] Romeo, N., Bosio, A., & Romeo, A. (2010). An innovative process suitable to produce high-efficiency CdTe/CdS thin-film modules. *Solar Energy Materials and Solar Cells, 94*(1), 2-7.

[33] Romeo, N., Bosio, A., Menossi, D., Romeo, A., & Aramini, M. (2014). Last Progress in CdTe/CdS Thin Film Solar Cell Fabrication Process. *Energy Procedia, 57*, 65-72.

[34] Britt, J., & Ferekides, C. (1993). Thin-film CdS/CdTe solar cell with 15.8% efficiency. *Applied Physics Letters, 62*(22), 2851-2852.

[35] Meyers, P. V. (1988). Design of a thin film CdTe solar cell. *Solar Cells, 23*(1), 59-67.

[36] Gupta, A., Parikh, V., & Compaan, A. D. (2006). High efficiency ultra-thin sputtered CdTe solar cells. *Solar Energy Materials and Solar Cells, 90*(15), 2263-2271.

[37] Matsumoto, H., Kuribayashi, K., Uda, H., Komatsu, Y., Nakano, A., & Ikegami, S. (1984). Screen-printed CdS/CdTe solar cell of 12.8% efficiency for an active area of 0.78 cm 2. *Solar Cells, 11*(4), 367-373.

[38] Wagner, S., Shay, J. L., Migliorato, P., & Kasper, H. M. (1974). $CuInSe_2$/CdS heterojunction photovoltaic detectors. *Applied Physics Letters, 25*(8), 434-435.

[39] Kazmerski, L. L., White, F. R., & Morgan, G. K. (1976). Thin-film $CuInSe_2$/CdS heterojunction solar cells. *Applied Physics Letters, 29*(4), 268-270.

[40] Ramanathan, K., Contreras, M.A., Perkins, C.L., Asher, S., Hasoon, F.S., Keane, J., Young, D., Romero, M., Metzger, W., Noufi, R. and Ward, J., 2003. Properties of 19.2% efficiency ZnO/CdS/$CuInGaSe_2$ thin-film solar cells. Progress in Photovoltaics: Research and Applications, 11(4), pp.225-230.

[41] Shi, J. H., Li, Z. Q., Zhang, D. W., Liu, Q. Q., Sun, Z., & Huang, S. M. (2011). Fabrication of Cu (In, Ga) Se_2 thin films by sputtering from a single quaternary chalcogenide target. *Progress in Photovoltaics: Research and Applications, 19*(2), 160-164.

[42] Sebastian, P. J., Calixto, M. E., Bhattacharya, R. N., & Noufi, R. (1999). CIS and CIGS based photovoltaic structures developed from electrodeposited precursors. *Solar energy materials and solar cells, 59*(1), 125-135.

[43] Ahn, S., Kim, K. H., Yun, J. H., & Yoon, K. H. (2009). Effects of selenization conditions on densification of Cu(In,Ga) Se_2 (CIGS) thin films prepared by spray deposition of CIGS nanoparticles. *Journal of Applied Physics, 105*(11), 113533.

[44] Repins, I., Contreras, M. A., Egaas, B., DeHart, C., Scharf, J., Perkins, C. L., ... & Noufi, R. (2008). 19· 9%-efficient ZnO/CdS/$CuInGaSe_2$ solar cell with 81· 2% fill factor. *Progress in Photovoltaics: Research and applications,16*(3), 235-239.

[45] Seol, J. S., Lee, S. Y., Lee, J. C., Nam, H. D., & Kim, K. H. (2003). Electrical and optical properties of Cu_2ZnSnS_4 thin films prepared by rf magnetron sputtering process. *Solar Energy Materials and Solar Cells, 75*(1), 155-162.

[46] Tanaka, T., Nagatomo, T., Kawasaki, D., Nishio, M., Guo, Q., Wakahara, A., ... & Ogawa, H. (2005). Preparation of Cu_2ZnSnS_4 thin films by hybrid sputtering. *Journal of Physics and Chemistry of Solids, 66*(11), 1978-1981.

[47] Hall, S. R., Szymanski, J. T., & Stewart, J. M. (1978). Kesterite, Cu< 2)(Zn, Fe) SnS< 4), and stannite, Cu< 2)(Fe, Zn) SnS< 4), structurally similar but distinct minerals. *The Canadian Mineralogist, 16*(2), 131-137.

[48] Schorr, S. (2007). Structural aspects of adamantine like multinary chalcogenides. *Thin Solid Films, 515*(15), 5985-5991.

[49] Chen, S., Gong, X. G., Walsh, A., & Wei, S. H. (2009). Crystal and electronic band structure of Cu_2ZnSnX_4 (X= S and Se) photovoltaic absorbers: first-principles insights. *Applied Physics Letters, 94*(4), 41903.

[50] Kumar, M., & Persson, C. (2013). Cu2ZnSnS4 and $Cu_2ZnSnSe_4$ as potential earth-abundant thin-film absorber materials: A density functional theory study. *Int. J. Theor. Appl. Sci, 5*(1).

[51] Paier, J., Asahi, R., Nagoya, A., & Kresse, G. (2009). Cu_2ZnSnS_4 as a potential photovoltaic material: a hybrid Hartree-Fock density functional theory study. *Physical Review B, 79*(11), 115126.

[52] Schorr, S., Hoebler, H. J., & Tovar, M. (2007). A neutron diffraction study of the stannite-kesterite solid solution series. *European Journal of Mineralogy,19*(1), 65-73.

[53] Persson, C. (2010). Electronic and optical properties of Cu_2ZnSnS_4 and Cu2ZnSnSe4. *Journal of Applied Physics, 107*(5), 3710.

[54] Schorr, S. (2011). The crystal structure of kesterite type compounds: A neutron and X-ray diffraction study. *Solar Energy Materials and Solar Cells,95*(6), 1482-1488.

[55] Ichimura, M., & Nakashima, Y. (2009). Analysis of atomic and electronic structures of Cu_2ZnSnS_4 based on first-principle calculation. *Japanese Journal of Applied Physics, 48*(9R), 090202.

[56] Zongyan, Z., & Xiang, Z. (2015). Electronic, optical, and mechanical properties of Cu_2ZnSnS_4 with four crystal structures Project supported by the National Natural Science Foundation of China (No. 21263006), the Science Research Foundation of Educational Commission of Yunnan Province of China (No. 2012Y542), and the Introduced Talents Foundation of Kunming University of Science and Technology. *Journal of Semiconductors, 36*(8), 083004.

[57] Nakamura, S., Maeda, T., & Wada, T. (2010). Phase stability and electronic structure of In-free photovoltaic materials: $Cu_2ZnSiSe_4$, Cu2ZnGeSe4, and Cu2ZnSnSe4. *Japanese Journal of Applied Physics, 49*(12R), 121203.

[58] Kumar, Y. K., Babu, G. S., Bhaskar, P. U., & Raja, V. S. (2009). Preparation and characterization of spray-deposited Cu_2ZnSnS_4 thin films. *Solar Energy Materials and Solar Cells, 93*(8), 1230-1237.

[59] Kumar, Y. B., Bhaskar, P. U., Babu, G. S., & Raja, V. S. (2010). Effect of copper salt and thiourea concentrations on the formation of Cu_2ZnSnS_4 thin films by spray pyrolysis. *physica status solidi (a)*, 207(1), 149-156.

[60] Jin, X., Li, J., Chen, G., Xue, C., Liu, W., & Zhu, C. (2016). Preparation of Cu2 ZnSnS4-based thin film solar cells by a combustion method. *Solar Energy Materials and Solar Cells, 146*, 16-24.

[61] Babu, G. S., Kumar, Y. K., Bhaskar, P. U., & Raja, V. S. (2008). Effect of post-deposition annealing on the growth of $Cu_2ZnSnSe_4$ thin films for a solar cell absorber layer. *Semiconductor Science and Technology*, *23*(8), 085023.

[62] Botti, S., Kammerlander, D., & Marque, M. A. (2011). Band structures of Cu_2ZnSnS_4 and $Cu_2ZnSnSe_4$ from many-body methods. *arXiv preprint arXiv:1105.4968*.

[63] Hönes, K., Zscherpel, E., Scragg, J., & Siebentritt, S. (2009). Shallow defects in Cu_2ZnSnS_4. *Physica B: Condensed Matter, 404*(23), 4949-4952.

[64] Katagiri, H., Saitoh, K., Washio, T., Shinohara, H., Kurumadani, T., & Miyajima, S. (2001). Development of thin film solar cell based on Cu_2ZnSnS_4 thin films. *Solar Energy Materials and Solar Cells, 65*(1), 141-148.

[65] Bär, M., Schubert, B. A., Marsen, B., Schorr, S., Wilks, R. G., Weinhardt, L., ... & Yang, W. (2011). Electronic structure of Cu_2ZnSnS_4 probed by soft x-ray emission and absorption spectroscopy. *Physical Review B, 84*(3), 035308.

[66] Pawar, S. M., Moholkar, A. V., Kim, I. K., Shin, S. W., Moon, J. H., Rhee, J. I., & Kim, J. H. (2010). Effect of laser incident energy on the structural, morphological and optical properties of Cu_2ZnSnS_4 (CZTS) thin films.*Current Applied Physics, 10*(2), 565-569.

[67] Katagiri, H. (2005). Cu_2ZnSnS_4 thin film solar cells. *Thin Solid Films, 480*, 426-432.

[68] Babu, G. S., Kumar, Y. K., Bhaskar, P. U., & Vanjari, S. R. (2010). Effect of Cu/(Zn+ Sn) ratio on the properties of co-evaporated $Cu_2ZnSnSe_4$ thin films. *Solar Energy Materials and Solar Cells, 94*(2), 221-226.

[69] Katagiri, H., Sasaguchi, N., Hando, S., Hoshino, S., Ohashi, J., & Yokota, T. (1997). Preparation and evaluation of Cu_2ZnSnS_4 thin films by sulfurization of E- B evaporated precursors. *Solar Energy Materials and Solar Cells, 49*(1), 407-414.

[70] Moriya, K., Tanaka, K., & Uchiki, H. (2007). Fabrication of Cu_2ZnSnS_4 thin-film solar cell prepared by pulsed laser deposition. *Japanese Journal of Applied Physics, 46*(9R), 5780.

[71] Matsushita, H., Maeda, T., Katsui, A., & Takizawa, T. (2000). Thermal analysis and synthesis from the melts of Cu-based quaternary compounds $Cu–III–IV–VI_4$ and $Cu_2–II–IV–VI_4$ (II= Zn, Cd; III= Ga, In; IV= Ge, Sn; VI= Se). *Journal of Crystal Growth, 208*(1), 416-422.

[72] Wibowo, R. A., Kim, W. S., Lee, E. S., Munir, B., & Kim, K. H. (2007). Single step preparation of quaternary $Cu_2ZnSnSe_4$ thin films by RF magnetron sputtering from binary chalcogenide targets. *Journal of Physics and Chemistry of Solids, 68*(10), 1908-1913.

[73] Babu, G. S., Kumar, Y. K., Bhaskar, P. U., & Raja, V. S. (2008). Growth and characterization of co-evaporated $Cu_2ZnSnSe_4$ thin films for photovoltaic applications. *Journal of Physics D: Applied Physics, 41*(20), 205305.

[74] Liu, M. L., Chen, I. W., Huang, F. Q., & Chen, L. D. (2009). Improved Thermoelectric Properties of Cu-Doped Quaternary Chalcogenides of $Cu_2CdSnSe_4$. *Advanced Materials, 21*(37), 3808-3812.

[75] Liu, M., Huang, F., Chen, L., & Chen, I. (2009). A wide-band-gap p-type thermoelectric material based on quaternary chalcogenidesof Cu2ZnSnQ4 (Q=S,Se). Retrieved from http://repository.upenn.edu/mse_papers/170

[76] Altosaar, M., Raudoja, J., Timmo, K., Danilson, M., Grossberg, M., Krustok, J., & Mellikov, E. (2008). $Cu_2Zn_{1−x}Cd_x$ Sn $(Se_{1−y}Sy)_4$ solid solutions as absorber materials for solar cells. *physica status solidi (a), 205*(1), 167-170.

[77] Zoppi, G., Forbes, I., Miles, R. W., Dale, P. J., Scragg, J. J., & Peter, L. M. (2009). $Cu_2ZnSnSe_4$ thin film solar cells produced by selenisation of magnetron sputtered precursors. *Progress in Photovoltaics: Research and Applications, 17*(5), 315-319.

[78] Ahn, S., Jung, S., Gwak, J., Cho, A., Shin, K., Yoon, K., ... & Yun, J. H. (2010). Determination of band gap energy (Eg) of Cu2ZnSnSe4 thin films: On the discrepancies of reported band gap values. *Appl. Phys. Lett, 97*(2), 021905.

[79] Riha, S. C., Parkinson, B. A., & Prieto, A. L. (2011). Compositionally Tunable $Cu_2ZnSn\ (S_{1−x}Se_x)_4$ Nanocrystals: Probing the Effect of Se-Inclusion in Mixed Chalcogenide Thin Films. *Journal of the American Chemical Society, 133*(39), 15272-15275.

[80] Wei, H., Ye, Z., Li, M., Su, Y., Yang, Z., & Zhang, Y. (2011). Tunable band gap Cu_2ZnSnS_{4x} $Se_{4(1-x)}$ nanocrystals: experimental and first-principles calculations. *CrystEngComm, 13*(7), 2222-2226.

[81] Katagiri, H., Jimbo, K., Maw, W. S., Oishi, K., Yamazaki, M., Araki, H., & Takeuchi, A. (2009). Development of CZTS-based thin film solar cells. *Thin Solid Films, 517*(7), 2455-2460.

[82] Walukiewicz, W. (1989). Amphoteric native defects in semiconductors. *Applied physics letters, 54*(21), 2094-2096.

[83] Zhang, J., & Shao, L. (2009). Cu_2ZnSnS_4 thin films prepared by sulfurizing different multilayer metal precursors. *Science in China Series E: Technological Sciences, 52*(1), 269-272.

[84] Zhou, Z., Wang, Y., Xu, D., & Zhang, Y. (2010). Fabrication of Cu_2ZnSnS_4 screen printed layers for solar cells. *Solar Energy Materials and Solar Cells,94*(12), 2042-2045.

[85] Su, Z., Yan, C., Sun, K., Han, Z., Liu, F., Liu, J., ... & Liu, Y. (2012). Preparation of Cu_2ZnSnS_4 thin films by sulfurizing stacked precursor thin films via successive ionic layer adsorption and reaction method. *Applied Surface Science, 258*(19), 7678-7682.

[86] Chen, S., Yang, J. H., Gong, X. G., Walsh, A., & Wei, S. H. (2010). Intrinsic point defects and complexes in the quaternary kesterite semiconductor Cu_2ZnSnS_4. *Physical Review B, 81*(24), 245204.

[87] Nagoya, A., Asahi, R., Wahl, R., & Kresse, G. (2010). Defect formation and phase stability of Cu_2ZnSnS_4 photovoltaic material. *Physical Review B,81*(11), 113202.

[88] Chen, S., Gong, X. G., Walsh, A., & Wei, S. H. (2010). Defect physics of the kesterite thin-film solar cell absorber Cu2ZnSnS4. *Applied Physics Letters, 96*(2), 021902.

[89] Zhang, S. B., Wei, S. H., Zunger, A., & Katayama-Yoshida, H. (1998). Defect physics of the $CuInSe_2$ chalcopyrite semiconductor. *Physical Review B, 57*(16), 9642.

[90] Walsh, A., Chen, S., Gong, X. G., Wei, S. H., Ihm, J., & Cheong, H. (2011, December). Crystal structure and defect reactions in the kesterite solar cell absorber Cu_2ZnSnS_4 (CZTS): Theoretical insights. In *AIP Conference Proceedings-American Institute of Physics* (Vol. 1399, No. 1, p. 63).

[91] Chen, S., Walsh, A., Gong, X. G., & Wei, S. H. (2013). Classification of Lattice Defects in the Kesterite Cu_2ZnSnS_4 and $Cu_2ZnSnSe_4$ Earth-Abundant Solar Cell Absorbers. *Advanced Materials, 25*(11), 1522-1539.

[92] Han, D., Sun, Y. Y., Bang, J., Zhang, Y. Y., Sun, H. B., Li, X. B., & Zhang, S. B. (2013). Deep electron traps and origin of p-type conductivity in the earth-abundant solar-cell material Cu_2ZnSnS_4. *Physical Review B, 87*(15), 155206.

[93] Chen, S., Wang, L. W., Walsh, A., Gong, X. G., & Wei, S. H. (2012). Abundance of CuZn+ SnZn and 2CuZn+ SnZn defect clusters in kesterite solar cells. *Applied Physics Letters, 101*(22), 223901.

[94] Olekseyuk, I. D., Dudchak, I. V., & Piskach, L. V. (2004). Phase equilibria in the Cu_2S–ZnS–SnS_2 system. *Journal of alloys and compounds, 368*(1), 135-143.

[95] Scragg, J. J. (2010). Studies of Cu_2ZnSnS_4 films prepared by sulphurisation of electrodeposited precursors (Doctoral dissertation). University of Bath.

[96] Muska, K., Kauk, M., Altosaar, M., Pilvet, M., Grossberg, M., & Volobujeva, O. (2011). Synthesis of Cu_2ZnSnS_4 monograin powders with different compositions. *Energy Procedia*, *10*, 203-207.

[97] Katagiri, H., Jimbo, K., Tahara, M., Araki, H., & Oishi, K. (2009). The influence of the composition ratio on CZTS-based thin film solar cells. In *MRS proceedings* (Vol. 1165, pp. 1165-M04). Cambridge University Press.

[98] Mitzi, D. B., Gunawan, O., Todorov, T. K., Wang, K., & Guha, S. (2011). The path towards a high-performance solution-processed kesterite solar cell. *Solar Energy Materials and Solar Cells*, *95*(6), 1421-1436.

[99] Walsh, A., Chen, S., Wei, S. H., & Gong, X. G. (2012). Kesterite Thin-Film Solar Cells: Advances in Materials Modelling of Cu_2ZnSnS_4. *Advanced Energy Materials, 2*(4), 400-409.

[100] Vigil-Galán, O., Espíndola-Rodríguez, M., Courel, M., Fontané, X., Sylla, D., Izquierdo-Roca, V., ... & Pérez-Rodríguez, A. (2013). Secondary phases dependence on composition ratio in sprayed Cu2ZnSnS4 thin films and its impact on the high power conversion efficiency. *Solar Energy Materials and Solar Cells, 117*, 246-250.

[101] Redinger, A., Hönes, K., Fontané, X., Izquierdo-Roca, V., Saucedo, E., Valle, N., ... & Siebentritt, S. (2011). Detection of a ZnSe secondary phase in coevaporated Cu2ZnSnSe4 thin films. *Applied Physics Letters*, *98*(10), 101907.

[102] Wang, K., Shin, B., Reuter, K. B., Todorov, T., Mitzi, D. B., & Guha, S. (2011). Structural and elemental characterization of high efficiency Cu2ZnSnS4 solar cells. *Applied Physics Letters, 98*(5), 1912.

[103] Li, Z., Liu, B., Yu, S., Wang, J., Li, Q., Zou, B., ... & Liu, J. (2010). The study of structural transition of ZnS nanorods under high pressure. *The Journal of Physical Chemistry C, 115*(2), 357-361.

[104] Siebentritt, S., & Schorr, S. (2012). Kesterites—a challenging material for solar cells. *Progress in Photovoltaics: Research and Applications, 20*(5), 512-519.

[105] Nozaki, H., Shibata, K., & Ohhashi, N. (1991). Metallic hole conduction in CuS. *Journal of solid state chemistry, 91*(2), 306-311.

[106] Liang, W., & Whangbo, M. H. (1993). Conductivity anisotropy and structural phase transition in covellite CuS. *Solid state communications, 85*(5), 405-408.

[107] Wagner, R., & Wiemhöfer, H. D. (1983). Hall effect and conductivity in thin films of low temperature chalcocite Cu_2S at 20° C as a function of stoichiometry. *Journal of Physics and Chemistry of Solids, 44*(8), 801-805.

[108] Thangaraju, B., & Kaliannan, P. (2000). Spray pyrolytic deposition and characterization of SnS and SnS_2 thin films. *Journal of Physics D: Applied Physics, 33*(9), 1054.

[109] Ogah, O. E., Zoppi, G., Forbes, I., & Miles, R. W. (2009). Thin films of tin sulphide for use in thin film solar cell devices. *Thin Solid Films, 517*(7), 2485-2488.

[110] Miles, R. W., Ogah, O. E., Zoppi, G., & Forbes, I. (2009). Thermally evaporated thin films of SnS for application in solar cell devices. *Thin Solid Films, 517*(17), 4702-4705.

[111] Calixto-Rodriguez, M., Martinez, H., Sanchez-Juarez, A., Campos-Alvarez, J., Tiburcio-Silver, A., & Calixto, M. E. (2009). Structural, optical, and electrical properties of tin sulfide thin films grown by spray pyrolysis. *Thin Solid Films, 517*(7), 2497-2499.

[112] Avellaneda, D., Nair, M. T. S., & Nair, P. K. (2009). Photovoltaic structures using chemically deposited tin sulfide thin films. *Thin Solid Films, 517*(7), 2500-2502.

[113] Deshpande, N. G., Sagade, A. A., Gudage, Y. G., Lokhande, C. D., & Sharma, R. (2007). Growth and characterization of tin disulfide (SnS_2) thin film deposited by successive ionic layer adsorption and reaction (SILAR) technique. *Journal of alloys and compounds, 436*(1), 421-426.

[114] Hu, X., Song, G., Li, W., Peng, Y., Jiang, L., Xue, Y., ... & Hu, J. (2013). Phase-controlled synthesis and photocatalytic properties of SnS, SnS 2 and SnS/SnS_2 heterostructure nanocrystals. *Materials Research Bulletin, 48*(6), 2325-2332.

[115] Tiwari, D., Chaudhuri, T. K., Shripathi, T., Deshpande, U., & Rawat, R. (2013). Non-toxic, earth-abundant 2% efficient Cu_2SnS_3 solar cell based on tetragonal films direct-coated from single metal-organic precursor solution. *Solar Energy Materials and Solar Cells, 113,* 165-170.

[116] Wu, C., Hu, Z., Wang, C., Sheng, H., Yang, J., & Xie, Y. (2007). Hexagonal Cu2SnS3 with metallic character: Another category of conducting sulfides. *Applied physics letters, 91*(14), 143104-143104.

[117] Berg, D. M., Djemour, R., Gütay, L., Siebentritt, S., Dale, P. J., Fontane, X., ... & Pérez-Rodriguez, A. (2012). Raman analysis of monoclinic Cu2SnS3 thin films. *Applied Physics Letters, 100*(19), 192103.

[118] Chino, K., Koike, J., Eguchi, S., Araki, H., Nakamura, R., Jimbo, K., & Katagiri, H. (2012). Preparation of Cu_2SnS_3 thin films by sulfurization of Cu/Sn stacked precursors. *Japanese Journal of Applied Physics, 51*(10S), 10NC35.

[119] Baranowski, L. L., Zawadzki, P., Christensen, S., Nordlund, D., Lany, S., Tamboli, A. C., ... & Zakutayev, A. (2014). Control of doping in Cu_2SnS_3 through defects and alloying. *Chemistry of Materials, 26*(17), 4951-4959.

[120] Shin, S. W., Pawar, S. M., Park, C. Y., Yun, J. H., Moon, J. H., Kim, J. H., & Lee, J. Y. (2011). Studies on Cu_2ZnSnS_4 (CZTS) absorber layer using different stacking orders in precursor thin films. *Solar Energy Materials and Solar Cells, 95*(12), 3202-3206.

[121] Fernandes, P. A., Salomé, P. M. P., & Da Cunha, A. F. (2011). Study of polycrystalline Cu_2ZnSnS_4 films by Raman scattering. *Journal of alloys and compounds, 509*(28), 7600-7606.

[122] Fernandes, P. A., Salomé, P. M. P., & Da Cunha, A. F. (2009). Growth and Raman scattering characterization of Cu_2ZnSnS_4 thin films. *Thin solid films, 517*(7), 2519-2523.

[123] Nilsen, W. G. (1969). Raman spectrum of cubic ZnS. *Physical Review,182*(3), 838.

[124] Fernandes, P. A., & da Cunha, A. F. (2010). A study of ternary Cu_2SnS_3 and Cu_3SnS_4 thin films prepared by sulfurizing stacked metal precursors. *Journal of Physics D: Applied Physics, 43*(21), 215403.

[125] Fernandes, P. A., Salomé, P. M. P., & Da Cunha, A. F. (2010). CuxSnS_{x+1} (x= 2, 3) thin films grown by sulfurization of metallic precursors deposited by dc magnetron sputtering. *physica status solidi (c), 7*(3-4), 901-904.

[126] Dimitrievska, M., Fairbrother, A., Fontané, X., Jawhari, T., Izquierdo-Roca, V., Saucedo, E., & Pérez-Rodríguez, A. (2014). Multiwavelength excitation Raman scattering study of polycrystalline kesterite Cu2ZnSnS4 thin films. *Applied Physics Letters, 104*(2), 021901.

[127] Berg, D. M., Arasimowicz, M., Djemour, R., Gütay, L., Siebentritt, S., Schorr, S., ... & Dale, P. J. (2014). Discrimination and detection limits of secondary phases in Cu_2ZnSnS_4 using X-ray diffraction and Raman spectroscopy. *Thin Solid Films, 569*, 113-123.

[128] Fontané, X., Calvo-Barrio, L., Izquierdo-Roca, V., Saucedo, E., Pérez-Rodriguez, A., Morante, J. R., ... & Siebentritt, S. (2011). In-depth resolved Raman scattering analysis for the identification of secondary phases: characterization of Cu2ZnSnS4 layers for solar cell applications. *Applied Physics Letters, 98*(18), 181905.

[129] Price, L. S., Parkin, I. P., Hardy, A. M., Clark, R. J., Hibbert, T. G., & Molloy, K. C. (1999). Atmospheric pressure chemical vapor deposition of tin sulfides (SnS, Sn_2S_3, and SnS_2) on glass. *Chemistry of materials, 11*(7), 1792-1799.

[130] Sandoval, S. J., Yang, D., Frindt, R. F., & Irwin, J. C. (1991). Raman study and lattice dynamics of single molecular layers of MoS_2. *Physical Review B, 44*(8), 3955.

[131] Márquez, J., Neuschitzer, M., Dimitrievska, M., Gunder, R., Haass, S., Werner, M., ... & Forbes, I. (2016). Systematic compositional changes and their influence on lattice and optoelectronic properties of Cu2ZnSnSe4 kesterite solar cells. *Solar Energy Materials and Solar Cells, 144*, 579-585.

[132] Pawar, S. M., Inamdar, A. I., Gurav, K. V., Shin, S. W., Jo, Y., Kim, J., ... & Kim, J. H. (2014). Growth of void free Cu2ZnSnS4 (CZTS) thin films by sulfurization of stacked metallic precursor films. *Vacuum, 104*, 57-60.

[133] Suryawanshi, M. P., Shin, S. W., Ghorpade, U. V., Gurav, K. V., Agawane, G. L., Hong, C. W., ... & Moholkar, A. V. (2014). A chemical approach for synthesis of photoelectrochemically active Cu2ZnSnS4 (CZTS) thin films.*Solar Energy, 110*, 221-230.

[134] Salomé, P. M. P., Malaquias, J., Fernandes, P. A., Ferreira, M. S., Leitão, J. P., Da Cunha, A. F., ... & Viana, E. R. (2011). The influence of hydrogen in the incorporation of Zn during the growth of Cu_2ZnSnS_4 thin films. *Solar Energy Materials and Solar Cells, 95*(12), 3482-3489.

[135] Maeda, K., Tanaka, K., Fukui, Y., & Uchiki, H. (2011). Dependence on Annealing Temperature of Properties of Cu_2ZnSnS_4 Thin Films Prepared by Sol–Gel Sulfurization Method. *Japanese Journal of Applied Physics,50*(1S2), 01BE10.

[136] Gurav, K. V., Pawar, S. M., Shin, S. W., Agawane, G. L., Patil, P. S., Moon, J. H., ... & Kim, J. H. (2013). Electrosynthesis of CZTS films by sulfurization of CZT precursor: Effect of soft annealing treatment. *Applied Surface Science, 283,* 74-80.

[137] Mkawi, E. M., Ibrahim, K., Ali, M. K. M., & Mohamed, A. S. (2013). Dependence of copper concentration on the properties of Cu2ZnSnS4 thin films prepared by electrochemical method. *Int. J. Electrochem. Sci, 8,* 359-368.

[138] Thiruvenkadam, S., Jovina, D., & Rajesh, A. L. (2014). The influence of deposition temperature in the photovoltaic properties of spray deposited CZTS thin films. *Solar Energy, 106,* 166-170.

[139] Rajeshmon, V. G., Kartha, C. S., Vijayakumar, K. P., Sanjeeviraja, C., Abe, T., & Kashiwaba, Y. (2011). Role of precursor solution in controlling the opto-electronic properties of spray pyrolysed Cu_2ZnSnS_4 thin films. *Solar Energy, 85*(2), 249-255.

[140] Wang, H. (2011). Progress in thin film solar cells based on. *International journal of Photoenergy*, 2011.

[141] Abusnina, M., Moutinho, H., Al-Jassim, M., DeHart, C., & Matin, M. (2014). Fabrication and Characterization of CZTS Thin Films Prepared by the Sulfurization of RF-Sputtered Stacked Metal Precursors. *Journal of Electronic Materials, 43*(9), 3145-3154.

[142] Yoo, H., & Kim, J. (2010). Growth of Cu_2ZnSnS_4 thin films using sulfurization of stacked metallic films. *Thin Solid Films, 518*(22), 6567-6572.

[143] Han, J., Shin, S. W., Gang, M. G., Kim, J. H., & Lee, J. Y. (2013). Crystallization behaviour of co-sputtered Cu2ZnSnS4 precursor prepared by sequential sulfurization processes. *Nanotechnology, 24*(9), 095706.

[144] Ge, J., Yu, W., Cao, H., Jiang, J., Ma, J., Yang, L., ... & Chu, J. (2012). Fabrication of Cu_2ZnSnS_4 absorbers by sulfurization of Sn-rich precursors. *physica status solidi (a), 209*(8), 1493-1497.

[145] He, J., Sun, L., Chen, Y., Jiang, J., Yang, P., & Chu, J. (2014). Cu_2ZnSnS_4 thin film solar cell utilizing rapid thermal process of precursors sputtered from a quaternary target: a promising application in industrial processes. *RSC Advances, 4*(81), 43080-43086.

[146] He, J., Sun, L., Zhang, K., Wang, W., Jiang, J., Chen, Y., ... & Chu, J. (2013). Effect of post-sulfurization on the composition, structure and optical properties of Cu_2ZnSnS_4 thin films deposited by sputtering from a single quaternary target. *Applied Surface Science, 264*, 133-138.

[147] Fan, P., Zhao, J., Liang, G. X., Gu, D., Zheng, Z. H., Zhang, D. P., ... & Ye, F. (2015). Effects of annealing treatment on the properties of CZTSe thin films deposited by RF-magnetron sputtering. *Journal of Alloys and Compounds, 625,* 171-174.

[148] Sun, R., Zhao, M., Zhuang, D., Gong, Q., Xie, M., Ouyang, L., ... & Zhang, L. (2016). Effects of selenization on phase transition and S/(S+ Se) ratios of as-deposited Cu_2ZnSnS_4 absorbers sputtered by a quaternary target. *Materials Letters, 164*, 140-143.

[149] Sun, L., He, J., Chen, Y., Yue, F., Yang, P., & Chu, J. (2012). Comparative study on Cu_2ZnSnS_4 thin films deposited by sputtering and pulsed laser deposition from a single quaternary sulfide target. *Journal of Crystal Growth,361*, 147-151.

[150] Dhakal, T. P., Peng, C. Y., Tobias, R. R., Dasharathy, R., & Westgate, C. R. (2014). Characterization of a CZTS thin film solar cell grown by sputtering method. *Solar Energy, 100*, 23-30.

[151] Son, D. H., Kim, D. H., Park, S. N., Yang, K. J., Nam, D., Cheong, H., & Kang, J. K. (2015). Growth and Device Characteristics of CZTSSe Thin-Film Solar Cells with 8.03% Efficiency. *Chemistry of Materials, 27*(15), 5180-5188.

[152] Ward, J. S., Ramanathan, K., Hasoon, F. S., Coutts, T. J., Keane, J., Contreras, M. A., ... & Noufi, R. (2002). A 21.5% efficient Cu (In, Ga) Se2 thin-film concentrator solar cell. *Progress in Photovoltaics: Research and Applications, 10*(1), 41-46.

[153] Schubert, B. A., Marsen, B., Cinque, S., Unold, T., Klenk, R., Schorr, S., & Schock, H. W. (2011). Cu_2ZnSnS_4 thin film solar cells by fast coevaporation. Progress in Photovoltaics: *Research and Applications, 19*(1), 93-96.

[154] Oishi, K., Saito, G., Ebina, K., Nagahashi, M., Jimbo, K., Maw, W. S., ... & Takeuchi, A. (2008). Growth of Cu_2ZnSnS_4 thin films on Si (100) substrates by multisource evaporation. *Thin Solid Films, 517*(4), 1449-1452.

[155] Tanaka, T., Kawasaki, D., Nishio, M., Guo, Q., & Ogawa, H. (2006). Fabrication of Cu_2ZnSnS_4 thin films by co-evaporation. *physica status solidi (c), 3*(8), 2844-2847.

[156] Katagiri, H., Ishigaki, N., Ishida, T., & Saito, K. (2001). Characterization of Cu_2ZnSnS_4 thin films prepared by vapor phase sulfurization. *Japanese Journal of Applied Physics, 40*(2R), 500.

[157] Xinkun, W., Wei, L., Shuying, C., Yunfeng, L., & Hongjie, J. (2012). Photoelectric properties of Cu_2ZnSnS_4 thin films deposited by thermal evaporation. *Journal of Semiconductors, 33*(2), 022002.

[158] Biccari, F., Chierchia, R., Valentini, M., Mangiapane, P., Salza, E., Malerba, C., ... & Mittiga, A. (2011). Fabrication of Cu_2ZnSnS_4 solar cells by sulfurization of evaporated precursors. *Energy Procedia, 10*, 187-191.

[159] Hsu, W. C., Repins, I., Beall, C., DeHart, C., To, B., Yang, W., ... & Noufi, R. (2014). Growth mechanisms of co-evaporated kesterite: a comparison of Cu-rich and Zn-rich composition paths. *Progress in Photovoltaics: Research and Applications, 22*(1), 35-43.

[160] Lee, Y. S., Gershon, T., Gunawan, O., Todorov, T. K., Gokmen, T., Virgus, Y., & Guha, S. (2015). $Cu_2ZnSnSe_4$ Thin-Film Solar Cells by Thermal Co-evaporation with 11.6% Efficiency and Improved Minority Carrier Diffusion Length. *Advanced Energy Materials*, *5*(7).

[161] Moholkar, A. V., Shinde, S. S., Babar, A. R., Sim, K. U., Lee, H. K., Rajpure, K. Y., ... & Kim, J. H. (2011). Synthesis and characterization of Cu_2ZnSnS_4 thin films grown by PLD: solar cells. *Journal of Alloys and Compounds*, *509*(27), 7439-7446.

[162] He, J., Sun, L., Chen, S., Chen, Y., Yang, P., & Chu, J. (2012). Composition dependence of structure and optical properties of $Cu_2ZnSn(S, Se)_4$ solid solutions: an experimental study. *Journal of Alloys and Compounds*, *511*(1), 129-132.

[163] Larramona, G., Bourdais, S., Jacob, A., Choné, C., Muto, T., Cuccaro, Y., ... & Dennler, G. (2014). 8.6% efficient CZTSSe solar cells sprayed from water–ethanol CZTS colloidal solutions. *The journal of physical chemistry letters*,*5*(21), 3763-3767.

[164] Daranfed, W., Aida, M. S., Attaf, N., Bougdira, J., & Rinnert, H. (2012). Cu_2ZnSnS_4 thin films deposition by ultrasonic spray pyrolysis. *Journal of Alloys and Compounds*, *542*, 22-27.

[165] Zeng, X., Tai, K. F., Zhang, T., Ho, C. W. J., Chen, X., Huan, A., ... & Wong, L. H. (2014). $Cu_2ZnSn(S, Se)_4$ kesterite solar cell with 5.1% efficiency using spray pyrolysis of aqueous precursor solution followed by selenization.Solar. *Energy Materials and Solar Cells, 124*, 55-60.

[166] Scragg, J. J., Berg, D. M., & Dale, P. J. (2010). A 3.2% efficient Kesterite device from electrodeposited stacked elemental layers. *Journal of Electroanalytical Chemistry, 646*(1), 52-59.

[167] Jeon, M., Shimizu, T., & Shingubara, S. (2011). Cu_2ZnSnS_4 thin films and nanowires prepared by different single-step electrodeposition method in quaternary electrolyte. *Materials Letters, 65*(15), 2364-2367.

[168] Guo, L., Zhu, Y., Gunawan, O., Gokmen, T., Deline, V. R., Ahmed, S., ... & Deligianni, H. (2014). Electrodeposited $Cu_2ZnSnSe_4$ thin film solar cell with 7% power conversion efficiency. *Progress in Photovoltaics: Research and Applications, 22*(1), 58-68.

[169] Swami, S. K., Kumar, A., & Dutta, V. (2013). Deposition of kesterite Cu_2ZnSnS_4 (CZTS) thin films by spin coating technique for solar cell application. *Energy Procedia, 33,* 198-202.

[170] Yeh, M. Y., Lee, C. C., & Wuu, D. S. (2009). Influences of synthesizing temperatures on the properties of Cu_2ZnSnS_4 prepared by sol–gel spin-coated deposition. *Journal of sol-gel science and technology, 52*(1), 65-68.

[171] Barkhouse, D. A. R., Gunawan, O., Gokmen, T., Todorov, T. K., & Mitzi, D. B. (2012). Device characteristics of a 10.1% hydrazine-processed $Cu_2ZnSn(Se, S)_4$ solar cell. *Progress in Photovoltaics: Research and Applications,20*(1), 6-11.

[172] Haass, S. G., Diethelm, M., Werner, M., Bissig, B., Romanyuk, Y. E., & Tiwari, A. N. (2015). 11.2% Efficient Solution Processed Kesterite Solar Cell with a Low Voltage Deficit. *Advanced Energy Materials, 5*(18).

[173] Ohring, M. (1992). *The Materials Science of Thin Films*. Boston: Academic Press.

[174] Seshan, K.(2012). Handbook of thin film deposition: Techniques, processes, and technologies. Amesterdam: Elsevier.

[175] Wasa, K., Kanno, I., and Kotera, H. (2012). Handbook of sputter deposition technology: Fundamentals and applications for functional thin films, nano-materials and MEMS. Waltham, MA: William Andrew.

[176] Oladeji, I. O., & Chow, L. (1997). Optimization of chemical bath deposited cadmium sulfide thin films. *Journal of the Electrochemical Society, 144*(7), 2342-2346.

[177] Ortega-Borges, R., & Lincot, D. (1993). Mechanism of Chemical Bath Deposition of Cadmium Sulfide Thin Films in the Ammonia-Thiourea System In Situ Kinetic Study and Modelization. *Journal of the Electrochemical Society, 140*(12), 3464-3473.

[178] Niki, S., Contreras, M., Repins, I., Powalla, M., Kushiya, K., Ishizuka, S., & Matsubara, K. (2010). CIGS absorbers and processes. *Progress in Photovoltaics: Research and Applications, 18*(6), 453-466.

[179] Chopra, K. L., Paulson, P. D., & Dutta, V. (2004). Thin-film solar cells: an overview. *Progress in Photovoltaics: Research and Applications, 12*(2-3), 69-92.

[180] Tsepulin, V. G., Perchik, A. V., Tolstoguzov, V. L., & Karasik, V. E. (2015). Thin film thickness measurement error reduction by wavelength selection in spectrophotometry. In *Journal of Physics: Conference Series* (Vol. 584, No. 1, p. 012011). IOP Publishing.

[181] Siderov, V., Mladenova, D., Yordanov, R., Milenkov, V., Ohlidal, M., Salyk, O., ... & Weiter, M. (2013). Film thickness measurement by optical profilometer MicroProf® FRT. *Bulg. Chem. Commun, 45*, 194-197.

[182] Bennett, J. M., & Dancy, J. H. (1981). Stylus profiling instrument for measuring statistical properties of smooth optical surfaces. *Applied Optics,20*(10), 1785-1802.

[183] Piegari, A., & Masetti, E. (1985). Thin film thickness measurement: a comparison of various techniques. *Thin solid films, 124*(3), 249-257.

[184] Kim, S. W., & Kim, G. H. (1999). Thickness-profile measurement of transparent thin-film layers by white-light scanning interferometry. *Applied Optics, 38*(28), 5968-5973.

[185] Maniscalco, B., Kaminski, P. M., & Walls, J. M. (2014). Thin film thickness measurements using scanning white light interferometry. *Thin Solid Films,550*, 10-16.

[186] Kao, S. C., & Doremus, R. H. (1994). Silica Films on Silicon Thickness Measurement by Electron Microscopy and Ellipsometry. Journal of The Electrochemical Society, 141(7), 1832-1838.

[187] McCrackin, F. L., Passaglia, E., Stromberg, R. R., & Steinberg, H. L. (1963). Measurement of the thickness and refractive index of very thin films and the optical properties of surfaces by ellipsometry. J. Res. Nat. Bur. Sec. A, 67.

[188] Emiliani, G., Flori, D., Masetti, E., & Piegari, A. (1985). The use of a spectrophotometer for the optical monitoring of thin films. Thin Solid Films,124(3), 259-264.

[189] Katagiri, H., & Jimbo, K. (2011, June). Development of rare metal-free CZTS-based thin film solar cells. In *Photovoltaic Specialists Conference (PVSC), 2011 37th IEEE* (pp. 003516-003521). IEEE.

[190] Ericson, T., Kubart, T., Scragg, J. J., & Platzer-Björkman, C. (2012). Reactive sputtering of precursors for Cu_2ZnSnS_4 thin film solar cells. *Thin Solid Films, 520*(24), 7093-7099.

[191] Scherrer, P. (1969). Bestimmung der Grosse und der inneren Struktur von Kolloidteilchen mittels Rontgenstrahlen (1918) in: X-ray Diffraction Methods in Polymer Science, Ed. LE Alexander.

[192] Cullity, B. D., & Stock, S. R. (2001). Elements of x-ray diffraction. Upper Saddle River, NJ: Prentice Hall.

[193] Monshi, A., Foroughi, M. R., & Monshi, M. R. (2012). Modified Scherrer equation to estimate more accurately nano-crystallite size using XRD. *World Journal of Nano Science and Engineering, 2*(03), 154.

[194] Mansour, H. M., & Hickey, A. J. (2007). Raman characterization and chemical imaging of biocolloidal self-assemblies, drug delivery systems, and pulmonary inhalation aerosols: a review. *AAPS PharmSciTech, 8*(4), 140-155.

[195] Smith, E., & Dent, G. (2005). Modern Raman spectroscopy: A practical approach. Hoboken, NJ: J. Wiley.

[196] Gremlich, H., & Yan, B. (2001). Infrared and raman spectroscopy of biological materials. New York: M. Dekker.

[197] Goldstein, J. (2003). Scanning electron microscopy and x-ray microanalysis. New York: Kluwer Academic/Plenum.

[198] Potts, P. J., & Webb, P. C. (1992). X-ray fluorescence spectrometry. *Journal of Geochemical Exploration, 44*(1), 251-296.

[199] Lakowicz, J. R. (2006). Principles of fluorescence spectroscopy. New York: Springer.

[200] Pankove, J. I. (1971). Optical processes in semiconductors. Englewood Cliffs, NJ: Prentice-Hall.

[201] Kumar, Y. B., Babu, G. S., Bhaskar, P. U., & Raja, V. S. (2009). Effect of starting-solution pH on the growth of $Cu_2ZnSnS4$ thin films deposited by spray pyrolysis. *physica status solidi (a), 206*(7), 1525-1530.

[202] Fernandes, P. A., Salomé, P. M. P., & Da Cunha, A. F. (2009). Precursors' order effect on the properties of sulfurized Cu_2ZnSnS_4 thin films. *Semiconductor Science and Technology, 24*(10), 105013.

[203] Hergert, F., & Hock, R. (2007). Predicted formation reactions for the solid-state syntheses of the semiconductor materials Cu_2SnX_3 and Cu_2ZnSnX_4 (X= S, Se) starting from binary chalcogenides. *Thin solid films,515*(15), 5953-5956.

[204] Schorr, S., Weber, A., Honkimäki, V., & Schock, H. W. (2009). In-situ investigation of the kesterite formation from binary and ternary sulphides.*Thin Solid Films, 517*(7), 2461-2464.

[205] Araki, H., Kubo, Y., Mikaduki, A., Jimbo, K., Maw, W. S., Katagiri, H., ... & Takeuchi, A. (2009). Preparation of Cu_2ZnSnS_4 thin films by sulfurizing electroplated precursors. *Solar Energy Materials and Solar Cells, 93*(6), 996-999.

[206] Pawar, S. M., Inamdar, A. I., Pawar, B. S., Gurav, K. V., Shin, S. W., Yanjun, X., ... & Im, H. (2014). Synthesis of Cu_2ZnSnS_4 (CZTS) absorber by rapid thermal processing (RTP) sulfurization of stacked metallic precursor films for solar cell applications. *Materials Letters, 118*, 76-79.

[207] Gao, C., Shen, H., Jiang, F., & Guan, H. (2012). Preparation of Cu_2ZnSnS_4 film by sulfurizing solution deposited precursors. *Applied Surface Science,261*, 189-192.

[208] Katagiri, H., Nishimura, M., Onozawa, T., Maruyama, S., Fujita, M., Sega, T., & Watanabe, T. (1997, August). Rare-metal free thin film solar cell. In *Power Conversion Conference-Nagaoka 1997., Proceedings of the* (Vol. 2, pp. 1003-1006). IEEE.

[209] Wang, K., Gunawan, O., Todorov, T., Shin, B., Chey, S. J., Bojarczuk, N. A., ... & Guha, S. (2010). Thermally evaporated Cu2ZnSnS4 solar cells. *Applied Physics Letters, 97*(14).

[210] Katagiri, H., Jimbo, K., Moriya, K., & Tsuchida, K. (2003, May). Solar cell without environmental pollution by using CZTS thin film. In *Photovoltaic Energy Conversion, 2003. Proceedings of 3rd World Conference on* (Vol. 3, pp. 2874-2879). IEEE.

[211] Grenet, L., Bernardi, S., Kohen, D., Lepoittevin, C., Noël, S., Karst, N., ... & Mariette, H. (2012). $Cu_2ZnSn(S_{1-x}Se_x)_4$ based solar cell produced by selenization of vacuum deposited precursors. *Solar Energy Materials and Solar Cells, 101*, 11-14.

[212] Jimbo, K., Kimura, R., Kamimura, T., Yamada, S., Maw, W. S., Araki, H., ... & Katagiri, H. (2007). Cu_2ZnSnS_4-type thin film solar cells using abundant materials. *Thin Solid Films, 515*(15), 5997-5999.

[213] Maeda, K., Tanaka, K., Nakano, Y., & Uchiki, H. (2011). Annealing temperature dependence of properties of Cu_2ZnSnS_4 thin films prepared by sol–gel sulfurization method. *Japanese Journal of Applied Physics, 50*(5S2), 05FB08.

[214] Guan, H., Shen, H., Gao, C., & He, X. (2013). Sulfurization time effects on the growth of Cu_2ZnSnS_4 thin films by solution method. *Journal of Materials Science: Materials in Electronics, 24*(8), 2667-2671.

[215] Emrani, A., Vasekar, P., & Westgate, C. R. (2013). Effects of sulfurization temperature on CZTS thin film solar cell performances. *Solar Energy, 98*, 335-340.

[216] González, J. C., Fernandes, P. A., Ribeiro, G. M., Abelenda, A., Viana, E. R., Salomé, P. M. P., & da Cunha, A. F. (2014). Influence of the sulphurization time on the morphological, chemical, structural and electrical properties of Cu_2ZnSnS_4 polycrystalline thin films. *Solar Energy Materials and Solar Cells, 123*, 58-64.

[217] Ge, J., Wu, Y., Zhang, C., Zuo, S., Jiang, J., Ma, J., ... & Chu, J. (2012). Comparative study of the influence of two distinct sulfurization ramping rates on the properties of Cu_2ZnSnS_4 thin films. *Applied Surface Science,258*(19), 7250-7254.

[218] Khalkar, A., Lim, K. S., Yu, S. M., Shin, D. W., Oh, T. S., & Yoo, J. B. (2015). Effects of Sulfurization Pressure on the Conversion Efficiency of Cosputtered Cu_2ZnSnS_4 Thin Film Solar Cells. *International Journal of Photoenergy*, 2015.

[219] Chalapathy, R. B. V., Jung, G. S., & Ahn, B. T. (2011). Fabrication of Cu_2ZnSnS_4 films by sulfurization of Cu/ZnSn/Cu precursor layers in sulfur atmosphere for solar cells. *Solar Energy Materials and Solar Cells, 95*(12), 3216-3221.

[220] Amal, M. I., & Kim, K. H. (2013). Structural and optical properties of sulfurized Cu_2ZnSnS_4 thin films from Cu–Zn–Sn alloy precursors. *Journal of Materials Science: Materials in Electronics, 24*(2), 559-566.

[221] Weber, A., Mainz, R., & Schock, H. W. (2010). On the Sn loss from thin films of the material system Cu–Zn–Sn–S in high vacuum. *Journal of Applied Physics, 107*(1), 013516.

[222] Redinger, A., & Siebentritt, S. (2010). Coevaporation of Cu2ZnSnSe4 thin films. *Applied Physics Letters, 97*(9), 092111.

[223] Marshall, R., & Mitra, S. S. (1965). Optical properties of cuprous sulfide. *Journal of Applied Physics, 36*(12), 3882-3883.

[224] Weber, A., Krauth, H., Perlt, S., Schubert, B., Kötschau, I., Schorr, S., & Schock, H. W. (2009). Multi-stage evaporation of Cu_2ZnSnS_4 thin films.*Thin Solid Films, 517*(7), 2524-2526.

[225] Abusnina, M., Matin, M., Moutinho, H. R., Blackburn, J. L., Alleman, J., DeHart, C., ... & Al-Jassim, M. (2015). Suppression of the Secondary Phases in CZTS

Films Through Controlling the Film Elemental Composition. *IEEE Journal of Photovoltaics, 5*(5), 1470-1475.

[226] Tanaka, K., Fukui, Y., Moritake, N., & Uchiki, H. (2011). Chemical composition dependence of morphological and optical properties of Cu_2ZnSnS_4 thin films deposited by sol–gel sulfurization and Cu_2ZnSnS_4 thin film solar cell efficiency. *Solar Energy Materials and Solar Cells, 95*(3), 838-842.

[227] Tanaka, T., Yoshida, A., Saiki, D., Saito, K., Guo, Q., Nishio, M., & Yamaguchi, T. (2010). Influence of composition ratio on properties of Cu_2ZnSnS_4 thin films fabricated by co-evaporation. *Thin Solid Films, 518*(21), S29-S33.

[228] Abou-Ras, D., Schorr, S., & Schock, H. W. (2007). Grain-size distributions and grain boundaries of chalcopyrite-type thin films. *Journal of Applied Crystallography, 40*(5), 841-848.

[229] Moholkar, A. V., Shinde, S. S., Agawane, G. L., Jo, S. H., Rajpure, K. Y., Patil, P. S., ... & Kim, J. H. (2012). Studies of compositional dependent CZTS thin film solar cells by pulsed laser deposition technique: An attempt to improve the efficiency. *Journal of Alloys and Compounds, 544*, 145-151.

[230] Araki, H., Mikaduki, A., Kubo, Y., Sato, T., Jimbo, K., Maw, W. S., ... & Takeuchi, A. (2008). Preparation of Cu_2ZnSnS_4 thin films by sulfurization of stacked metallic layers. *Thin Solid Films, 517*(4), 1457-1460.

[231] Ghorpade, U. V., Suryawanshi, M. P., Shin, S. W., Hong, C. W., Kim, I., Moon, J. H., ... & Kolekar, S. S. (2015). Wurtzite CZTS nanocrystals and phase evolution to kesterite thin film for solar energy harvesting. *Physical Chemistry Chemical Physics, 17*(30), 19777-19788.

[232] Shin, B., Zhu, Y., Bojarczuk, N. A., Chey, S. J., & Guha, S. (2012). Control of an interfacial MoSe2 layer in Cu2ZnSnSe4 thin film solar cells: 8.9% power conversion efficiency with a TiN diffusion barrier. *Applied Physics Letters, 101*(5), 053903.

[233] Fernandes, P. A., Salomé, P. M. P., Da Cunha, A. F., & Schubert, B. A. (2011). Cu_2ZnSnS_4 solar cells prepared with sulphurized dc-sputtered stacked metallic precursors. *Thin Solid Films, 519*(21), 7382-7385.

[234] Platzer-Björkman, C., Scragg, J., Flammersberger, H., Kubart, T., & Edoff, M. (2012). Influence of precursor sulfur content on film formation and compositional changes in Cu_2ZnSnS_4 films and solar cells. *Solar Energy Materials and Solar Cells, 98*, 110-117.

[235] Mattox, D. M. (1989). Particle bombardment effects on thin-film deposition: A review. *Journal of Vacuum Science & Technology A, 7*(3), 1105-1114.